JAGIELLONIAN UNIVERSITY
FACULTY OF PHYSICS, ASTRONOMY AND APPLIED COMPUTER SCIENCE

Monika Pawlik - Niedźwiecka

index number: 1069039

Studies of changes of signals shapes in plastic scintillator strips

Master Thesis

Major: Physics
Specialisation: Nuclear Physics

supervised by:

Prof. dr hab. Paweł Moskal
Institute of Physics
Division of Nuclear Physics

Cracow, 2014

Oświadczenie autora pracy

Świadoma odpowiedzialności prawnej oświadczam, że niniejsza praca dyplomowa została napisana przeze mnie samodzielnie i nie zawiera treści uzyskanych w sposób niezgodny z obowiązującymi przepisami.
Oświadczam również, że przedstawiona praca nie była wcześniej przedmiotem procedur związanych z uzyskaniem tytułu zawodowego w wyższej uczelni.

Kraków, dnia

Podpis autora pracy

Oświadczenie kierującego pracą

Potwierdzam, że niniejsza praca została przygotowana pod moim kierunkiem i kwalifikuje się do przedstawienia jej w postępowaniu o nadanie tytułu zawodowego.

Kraków, dnia

Podpis kierującego pracą

Acknowledgements

I would like to express gratitude to all people without whom I would not have completed this thesis.

First and foremost, I would like to express my sincere appreciation and gratitude to my advisor, prof. dr hab. Paweł Moskal, for his guidance, support and encouragement. He was extremely patient and never got upset over mistakes. Instead, he constantly gave me valuable suggestions.

I am also indebted to my guide, dr Michał Silarski, for personal attention which have provided good basis for my master thesis.

I thank my colleagues: Michał, Agata, Monika, Jagoda, Basia, Tomek and my brother Michał because they were always with me and have supported me over the last year.

Words are short to express my deep sense of gratitude towards my loving husband, Szymon, for his enormous help and taking care of our son. He used to review my thesis progress, give me valuable suggestions and made corrections.

I thank my son, Filip, for his smile and making me happy. I love you so much.

Dziękuję Rodzicom i Teściom za ogromną pomoc i cierpliwość. Ta praca nie powstałaby bez Was.

Abstract

The main aim of this master thesis was to study properties of signals in plastic scintillator detectors with different shapes. The scintillators with the length of 500 mm and cross sections of square (14 mm side), hexagonal (9 mm side), triangular (17 mm side) and circular (16 mm and 10mm dia.) were studied. A series of measurements were done with ^{68}Ge radioactive source placed in lead collimator. 500 mm long scintillator connected to two photomultipliers by optical gel and reference detector were used to make an experimental setup. Measurements were performed at 5 positions across each strip. It was observed that the rise time increases and the fall time decreases with the distance between the irradiation place and photomultiplier.

Streszczenie

Głównym celem pracy magisterskiej były studia własności sygnałów w plastikowych detektorach scyntylacyjnych o różnych kształtach. Przetestowane zostały scyntylatory o długości 500 mm i przekrojach: kwadratowym (14 mm bok), sześciokątnym (9 mm bok), trójkątnym (17 mm bok) i okrągłym (16 mm i 10 mm średnicy). Wykonano szereg pomiarów przy użyciu radioaktywnego źródła ^{68}Ge umieszczonego w ołowianym kolimatorze. Układ pomiarowy składał się z 500 mm paska połączonego z dwoma fotopowielaczami przy użyciu żelu optycznego oraz detektora referencyjnego. Pomiary zostały wykonane dla 5 pozycji wzdłuż każdego z pasków. Zaobserwowano, że czas narastania rośnie, natomiast czas opadania maleje, wraz z odległością pomiędzy miejscem naświetlania a fotopowielaczem.

Contents

1 Introduction

Positron Emission Tomography, called PET, belongs to medicine imaging group and uses radiology tests to obtain information about body tissues, their condition and functioning and also physiological processes ongoing inside the human body. To define various types of disorders, like cancers, heart diseases and neurological abnormalities, PET use a small amount of radionuclid emitting positrons which annihilate with electrons creating two 511-keV γ quanta. This γ quanta are detected by scanning device composed of ring of crystal detectors connected with photomultipliers which convert light signals from scintillators to its electrical equivalent. Reconstruction methods are used to find place of annihilation.
Novel PET system, called J-PET, is currently under development at Jagiellonian University [1, 2, 3]. The innovative solutions is the use of polymer scintillator strips instead of crystals. The possibility of using 1 m length scintillators allows to build large cylindrical diagnostic chamber enabling scan of larger area of patient body.
The main aim of this master thesis is to study changes of signal properties generated by different shapes of scintillators. In the second section a basic informations about PET tomography are described. This chapter contains description about $\beta+$ decay and interaction of γ radiation with matter, radiopharmaceuticals, differences between inorganic and organic scintillators and also details about light collection in ogranic scintillators. In next part of this chapter PET and J-PET systems are described in details.
In experimental part (chapter 3) setup used to meausure properties of signals: rise and fall time, area under signals and their amplitude, is described. This chapter includes also details about analysis and comparison of above mentioned parameters between different scintillators shapes. Histograms and plots for hexagon shape of scintillator are presented. The spectra for the rest of shapes are shown in Appendices. Results for all shapes are discussed.
Appendix A contains experimental details about different measurements. Rise and fall time spectra for the rest of scintillators shapes are included in Appendix B and Appendix C respectively. Appendix D and E contain the spectra of area under signals and amplitudes.

2 Basics of PET tomography

Positron Emission Tomography (PET) is now one of the most technologically advanced diagnostic methods. PET provides non-invasive imaging of ongoing physiological processes in the body. Additionally, it makes possible to monitore theraphy effects which is really important in cardiology, oncology and neurlogy.
Positron Emission Tomography relies on observation how concetration and localization of chemical agent changes in patients body. This special chemical agent contains radioactive isotope emitting positrons. Positrons from $\beta+$ decays annihilate with electrons in the body and then as a results pairs of gamma quanta are emitted. PET systems register this gamma quanta in coincidence by ring of several thousand detectors. The complete reconstruction of the image is done by computer using appropriate algorithms [14].

2.1 $\beta+$ decay and interaction of γ radiation with matter

During $\beta+$ decay unstable atom (radionuclide) decays by convertion a proton into a neutron while emitting a positron and an electron neutrino. This process can be described as:

$$ {}^{Z}_{A}X \rightarrow {}^{Z}_{A-1}X' + e^{+} + \nu_e \tag{2.1} $$

where X - initial element, X′ - final element, A - mass number, Z - atomic number, ν_e - electron neutrino. Atomic number is reduced by one while mass number is not changed in newly created nucleus. Positron travels through different tissue inside patients body. Addittionally, this charged particle loses kinematic energy mainly by interactions with electrons and may create hydrogen-like system known as positronium when energy dicreases under 10 keV. Unstable positrionium decays by annihilation creating pair of 511-keV gamma quanta which move anti-parallel [8]. Only less than 2% of positrons annihilate without creating positronium.
The most important mechanisms of γ rays interactions with matter are photoelectric effect and Compton scattering.
In photoelectric effect γ rays interact with atom, transfer energy to inner shell and excite bound electron making atom unstable. Kinetic energy of ejected electon will be equal to difference between gamma ray energy and electron binding energy:

$$ E_e = E_\gamma - E_B \tag{2.2} $$

If electron is ejected from K-shell, electron from shell with higher energy can fill the gap to stabilize atom what results in an X-ray emission with energy equal to the energy difference between this two shells. This X-rays are then quickly absorbed.

The probability of photoelectric effect increases with atomic number of the medium and descreases with γ ray energy and it is approximately equal to

$$P \sim Z^5/{E_\gamma}^3 \tag{2.3}$$

Ejected electron is then fast absorbed in solid or liquid medium.

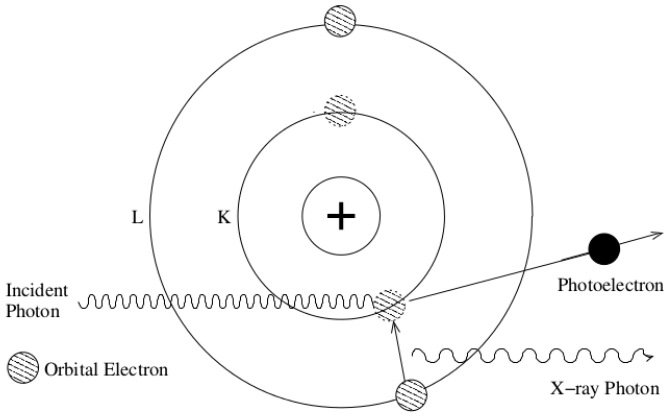

Figure 2.1: Photoelectric effect. Incident photon is absorbed by an electron bounded within an atom. As a result photoelectron is ejected from an atom and an X-ray phonon is created due to drop of electron from higher energy state [19].

The Compton effect, considered as an inelastic scattering, is based on γ rays scattering on free or loosely bound in an outer shell single atomic electrons named quasi-free electrons. In this effect incindent photon interacts with quasi-free electron, transfers some part of energy to the electron and ejects it with energy equals to difference between energy of scattered photon and electrons binding energy in the shell.

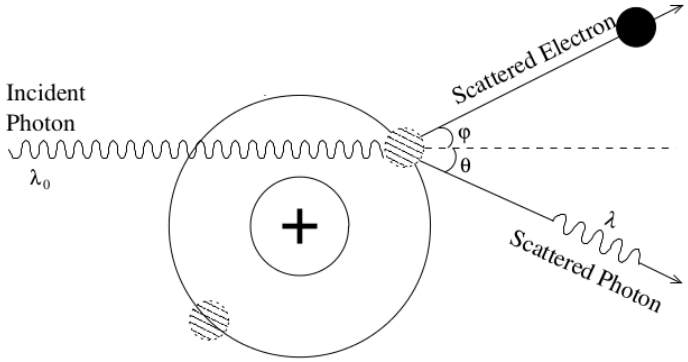

Figure 2.2: The Compton effect. Incident photon scatters on free or loosely bound electron under θ angle [19].

Momentum and energy conservation laws lead to equation for energy of scattered electrons:

$$E_{sc} = \frac{m_e c^2}{\frac{m_e c^2}{E} + 1 - cos\theta} \tag{2.4}$$

where E - energy of incoming photon, m_e - mass of the electron, c - speed of light and θ - scattering angle. Since $m_e c^2$ is equal to 511 keV and energy of incident photon in the PET tomography is equal to the same value the equation above reduces to the following form:

$$E_{sc} = \frac{511}{2 - cos\theta}[keV] \tag{2.5}$$

Maximum energy is transefered from photon to electron when θ is equal to 180^o. The probability of Compton effect increases with photon energy smaller than 1MeV, while after 1MeV it decreases with γ rays energy.

2.2 Inorganic and organic scintillators

One of the methods of detection ionizing radiation is light production in special type of transparent materials. Two main types of this materials are inorganic and organic scintillators. The most important parameters characterizing scintillators are:

- light output - number of photons produced per 1keV deposited energy by γ quanta in the scintillator,
- decay time - time of luminescence should be as short as possible,
- energy resolution - it should be very good.

When γ quanta deposited energy in the scintillator it emits isotropically light in visible region of the electromagnetic spectrum. Used scintillator should be composed with elements with a large atomic number, probability of 511 keV gamma quanta reaction quanta with scintillation materials depends on density which is related with atomic number.

Present PET systems use inorganic scintillators because of their high atomic number and good properties described earlier, which gives them a big advantage over organic scintillators. In this kind of materials scintillation mechanism depends on the energy states.

Electron has available states with discrete allowed values of energy. Between lower state, named as valence band, and upper state, called as conduction band, there is a forbidden band where electrons can not exist in pure crystal without any activators. Electrons are bound in the crystal lattice in the valence band. Radiation exicite electrons which can migrate to conduction band creating holes in the valence

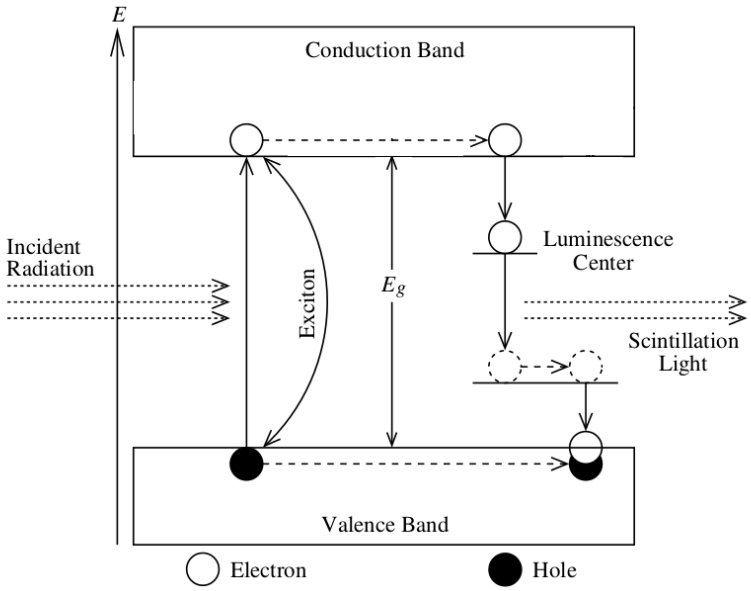

Figure 2.3: Scintillation mechanism in inorganic scintillators [19].

band. In conduction band electrons have enough energy to move across the crystal. Scintillators used in PET have modified energy states structure by impurities, called activators, which create additional states in the forbidden band. Activators ionization energy is smaller than normal crystal lattice, so positive holes migrate to activator location and ionize it. In meantime electrons in conduction band migrates until it meets enough ionized impurities and go to the an activator state. If upper activator state is formed as an excitated state, electron can very quickly de-excitate to the activator ground state by photon emission. For correctly chosen type of an activator the emitted photon is from the visible part of electromagnetic spectrum.
Organic scintillators are produced in solid and also liquid forms and in various geometric shape. Scintillation mechanism of organic scintillators depends on fluorescence following transitions between different energy levels in a single molecule with structure known as π-electron structure.

Energy space between singlet states S_0 (ground state) and S_1 is equal to about 3-4 eV, while the distance between vibrational levels is of the order of 0.15 eV. The incoming radiation transfers electrons to one of vibrational levels of S_1 band. Produced in this way system is unstable which forces electrons to radiationless transition from vibrational S_1 to ground S_1 band. Subsequently electrons de-excite from ground S_1 to ground or vibrational states of S_0 emitting photons from ultraviolet or visible region of electromagnetic spectrum. Energy emitted during fluorescence is smaller than energy absorbed from incoming radiation because electrons lose some

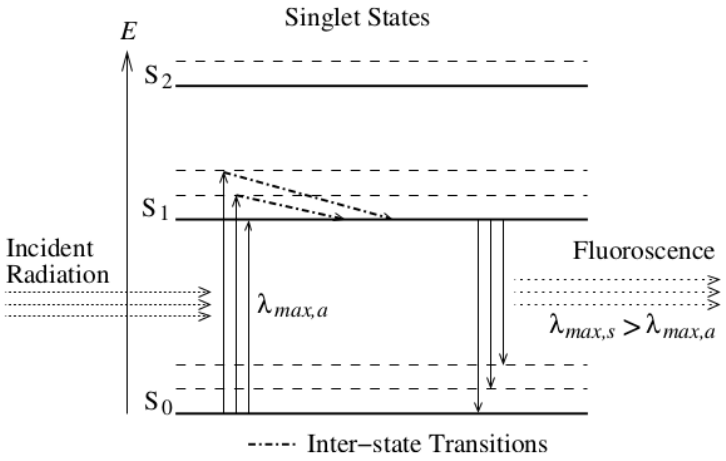

Figure 2.4: Scintillation mechanism in organic scintillators [19].

part of energy during transition between vibrational and ground level of S_1, so wavelength of fluorescence photon is bigger than wavelenght of absorbtion photon.
Other possible transition is through levels in a triplet T_1 state (as one can see in Fig. 2.5). Electrons from ground S_1 state de-excite to more stable T_1 vibrational levels instead of S_0 as was described earlier. Electrons are trapped for some period of time on T_1 levels and then de-excite first to the T_1 state and later to the ground S_0 state which results in emission of light known as phosphorescence after more than 100 ms from the excitation/gamma quantum interaction.

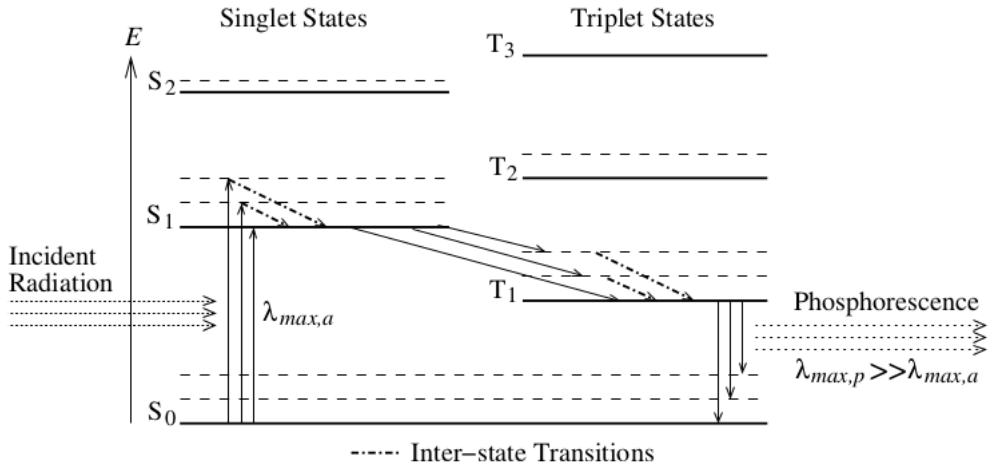

Figure 2.5: Singlet and triplet states of organic scintillators [19].

Comparison between properties of most popular inorganic and organic scintillators are shown in Tab. 2.1.

Name of scintillator	Type	Density (g/cm^3)	Light output (photons/MeV)	Decay time(ns)	Index of refraction
Sodium iodide |NaI(Tl)|	crystal	3.67	38000	230	1.85
Bismuth Germanate |BGO|	crystal	7.13	8000	300	2.15
Lutetium Oxyorthosilicate |LSO:Ce|	crystal	7.40	25000	~ 47	1.82
|BC404|	plastic	1.023	10400	1.8	1.58
|RP422|	plastic	1.02	8400	1.6	1.58

Table 2.1: Comparison between different type of scintillators [18, 25].

Solid plastic scintillators consists of a base, main organic scintillator and waveshifter. Organic scintillator like 2,5-Diphenyloxazole (PPO) or p-Terphenyl (PPP) can be dissolved in solvent and then polymerized. One can use solvent containing polyvinyltoulene or polystyrene. The idea of producing plastic scintillators is simple, but in practice it is not so easy, because to create this kind of scintillator one have to use very pure form and there should be some period of time between different steps of production. Waveshifter like as 5-Phenyl-2-[4-(5-phenyl-1,3-oxazol-2-yl)phenyl]-1,3-oxazole (POPOP) shifts light wavelength to visible region.
Properties of plastic scintillators studied in this thesis are shown in Tab. 2.2. Maximum wavelength λ_{max} means the most probable wavelength of emission, FWHM - width at half maximum of signals amplitude.

Light output (photons/MeV; % Anthracene)	Rise time (ns)	Fall time (ns)	FWHM (ns)	λ_{max} (nm)	(Bulk) light attenuation length(cm)
9700; 64	0.5	1.5	1.3	391	(110) 140

Table 2.2: Properties of EJ-230 scintillators [27].

Primary polymer of EJ-230 is polyvinyltoluene. Emission spectrum of EJ-230 provided by Eljen Technology is shown in Fig. 2.7.

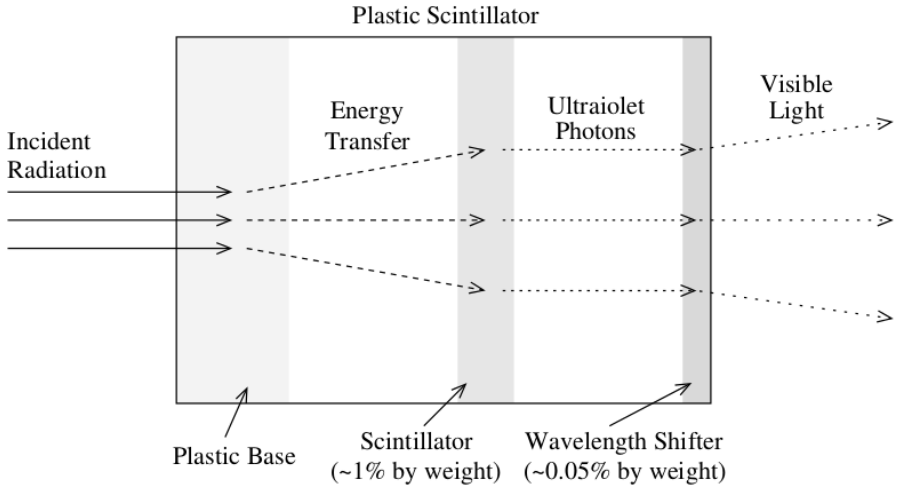

Figure 2.6: Working mechanism of plastic scintillator. Incident radiation interacts with plastic base. Deposited energy is then transfered to the scintillator. The scintillator produced an ultraviolet photons which are shifted to visible ligh region by the wavelength shifter [19].

Number of hydrogen and carbon atoms per cm^3 in EJ-230 is equal to 5.15×10^{22} and 4.69×10^{22}, respectively. Additionally, the number of electrons in $1cm^3$ amounts to 3.33×10^{23}. This kind of scintillator has very good timing properties which makes it the best choice for new prototype of PET scanner which is being built in Jagiellonian University in Cracow.

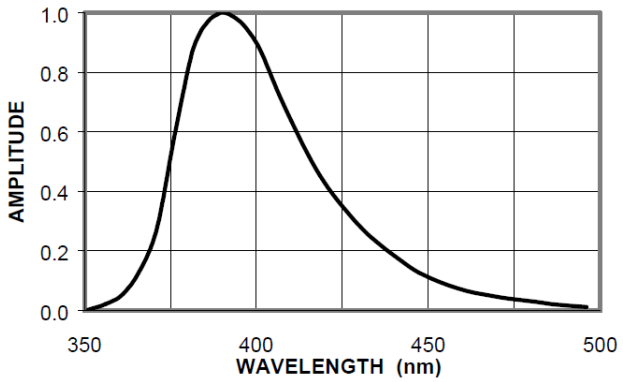

Figure 2.7: Emission spectrum of EJ-230. Figure adopted from [25].

2.3 Light collection in organic scintillators

In any kind of scintillators two things have influence light collection: scintillator can absorb emitted photons by itself (self-absorption) and losses them on material surfaces. In fact, self-absorption plays no significant role in light losses except scintillators with large diameter.
Fraction of light collecte from scintillator has an impact on energy resolution, the best resolution corresponds to collection of all photons released in the interaction. Moreover amplitudes of signals change with the position along the scintillator strip which influences additionally the overall energy resolution.
Light inside the scintillator is emitted isotropically, thus only a fraction of light is directly hitting the photomultiplier located on one surface of scintillator. Rest of the light reflects inside scintillator one or more times before reaching the photomultiplier. The total internal reflection occurs when photons incidence angle is bigger than so called critical angle. For smaller angles photons are transmitted through the scintillator surface or are reflected.

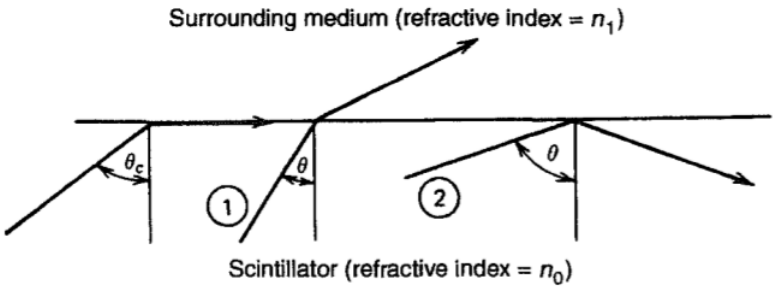

Figure 2.8: Possible light path inside scintillator when n_0 is greater than n_1. In first case ray sometimes can escape, but in second case one can see total internal reflection [21].

Desirable total internal reflection should be minimized on surfaces connected with photomultipliers by using transparent medium (e.g. silicon optical gel) with the same refraction index as scintillator. Plastic scintillators have refraction index similiar to the index of photmultipliers glass window. Light collecion can be increased by using more than one photomultiplier. It could be also enhanced by minimizing number of reflections.
In Positron Emission Tomography photomultipliers are used to convert incoming photons resulting from the interaction of γ rays with scintillator material to electrical signals. A photocatode is placed on one side of the photomultiplier tube, on the second end there is an anode and between them dynodes are located. Incident photons hit photocatode and they are converted by this photosensive element to

low-energy electrons in photoelectric effect. Electromagnetic lens focuses electrons to the first dynode. On each next dynodes voltage is higher than on previous one. Electrons from first dynode are accelerated, hit second dynode, knock out more electrons. This acceleration and multiplication of electrons is continued to the last dynode where pulse of electrons is formed and attracted to the anode.

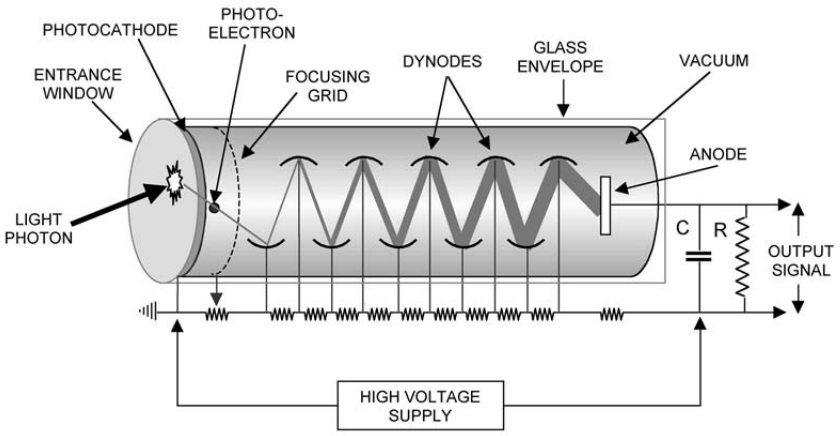

Figure 2.9: A photomultiplier tube [18].

Properties of photomultipliers used in experiments described later in this thesis are shown in Tab. 2.3. Photomultipliers produced by Hammmatsu, model R5320, serial number BA0202 (named as PM1) and BA0214 (named as F2), have bialkali photocathode with effective area equal to 20 mm dia., quartz window and also linear-focused structure of dynodes.

Name	Cathode Luminous Sens. [μA/lm]	Anode Luminous Sens. [A/lm]	Anode Dark Current [nA]	Cathode Blue Sens. Index
PM1	108.0	301.0	2.50	10.9
F2	98.9	356.0	1.20	10.7

Table 2.3: Properties of R5320 photomultipliers [26].

2.4 PET systems

Nowadays PET scanners are built out from block detectors arranged in ring. Typically, 3 cm thick single block detector constitutes from a crystal partially cut, with the deepest cuts at the edges, into smaller pieces (mostly, 8 x 8 elements) separated by reflective material and connected to photomultipliers. Cuts ensure linear division of scintillation light between all of the photomultipliers. For example, when γ quantum hits the edge of crystal scintillator, scintillation light is detected only by one

photomultiplier, but when it hits central position of crystal then produced light is detected by all photomultipliers. This results in a scintillation light distribution.

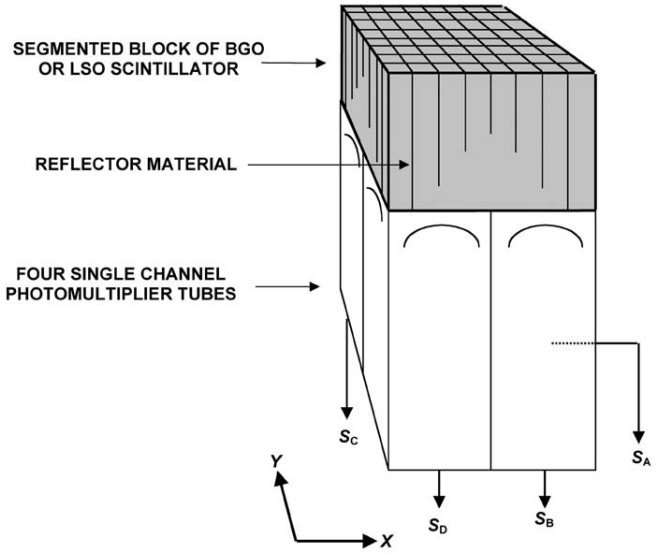

Figure 2.10: Typically block detector scheme [18].

One can calculate hit position of annihilation quanta in X and Y coordinates by using the following equations (where S_A, S_B, S_C and S_D means signals from four photomultiplier tubes) and receive a two-dimensional histogram (called flood histogram) as a result.

$$X = \frac{S_A + S_B - S_C - S_D}{S_A + S_B + S_C + S_D} \tag{2.6}$$

$$Y = \frac{S_A + S_C - S_B - S_D}{S_A + S_B + S_C + S_D} \tag{2.7}$$

Division of block detector for smaller pieces and its width determines spatial resolution which is equal to 3-5 mm in current PET scanners.

Photomultipliers used in the block detectors are one of the most expensive elements of modern PET scanners. On the other hand, thousands of detectors ensure good coverage of solid angle and this is the reason for continuous development of PET tomographs.

The most popular type of PET scanners is tomograph with large number of block detectors configured in ring. Typical dimension of crystal face of single unit is equal to 38 mm x 38 mm with depth equal to 30 mm, eight detector units create one module and 35 modules form a ring as one can see in Fig. 2.11.

One can measure pairs of gamma quanta originating from annihilation of the positron and electon with detectors using coincidence measurements. In the ideal case only true coincidences would be registered. True coincidence are events where one can

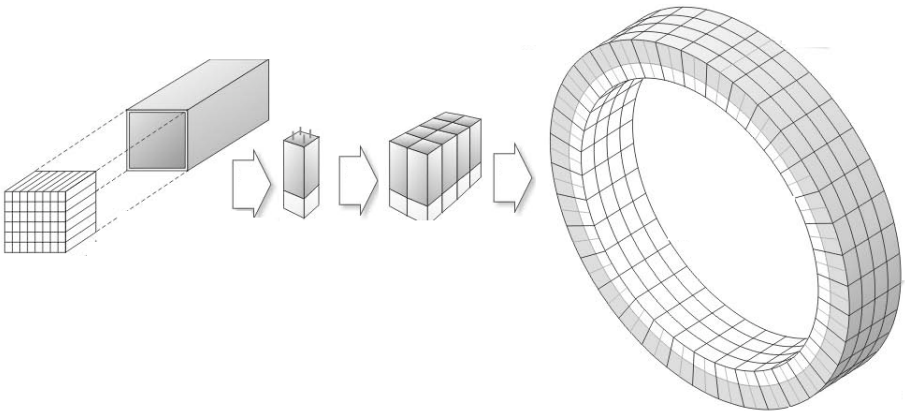

Figure 2.11: Standard PET system. Cutted scintillator is connected to the photomultiplier. 8 such modules form a photomultiplier matrix. Each block in the ring consists of one of such matrixes [12].

observe in small time window (e.g. 12 ns) pair of back-to-back photons exactly from the same radioactive decay and which have not changed direction or lost any energy before being detected [19]. One can also record multiple, random or scattered coincidences as it is shown in Fig.2.12.
Scattered coincidence occurs when two γ quanta from the same source have changed direction because of interaction inside the body which results in receiving a bad location of an event during measurement. γ quanta are registered in a small time window by detectors which define LOR line (line of response) for a given radiactive decay. In a random coincidence γ quanta originating from different sources are recorded by two opposite detectors in the ring while multiple coincidence happens when more than two gamma quanta are detected by two opposite detectors in small time window.
Different kinds of events cause deterioration of the resolution and contrast of image. By defining LOR which means path of photons originating from the same radioactive source one can reject multiple coincidences. Additionally, small time window allows partial rejection of random coincidences. Another way to improve resolution of tomographic image is the use of time of flight (TOF) method. PET TOF scanners use time difference between arrival time of two gamma quanta. Arrival time is counted as the time from the moment of their emission until their registration. One can determine the emission point Δd by the following relation:

$$\Delta d = \frac{\Delta t \times c}{2} \tag{2.8}$$

where: Δt - the difference of arrival times of two γ quanta, c - speed of light. However, this method is not currently used because of its difficulty and costly implement. Even

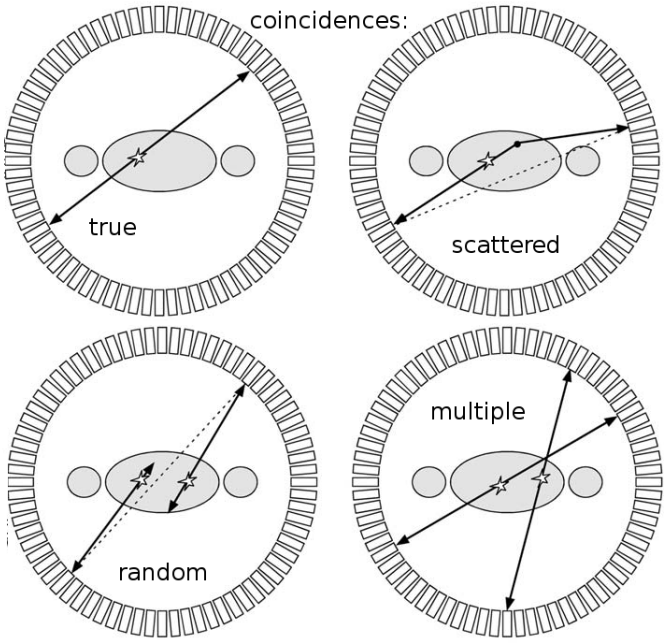

Figure 2.12: Different kinds of events in PET tomography [18].

a timing resolution as fine as 100 ps would only yield a positional resolution of ∼1.5 cm. With currently available detector technology, the best timing resolution that can be achieved is on the order of a few hundred picoseconds [18].

2.5 J-PET: novel PET systems

Organic scintillators have not been used in positron emission tomography because of their low density and low atomic number of the elements of the material. This properties imply small probability for gamma quanta detection and for transfer of the whole energy to electrons by the photoelectric effect. On the other hand they have long light attenuation length (about 2 meters) which allows for creation of scintillators up to a meter long and sufficient light output (about 10000 photons/MeV) with comparison to crystal scintillators. Instead of the photoelectric effect which probability is negligible one can use still the Compton effect. The maximum energy deposition of electrons from the Compton edge is equal to about 340 keV. Thus Strip PET with low energy threshold of 200 keV will reduce the scattering of gamma quanta in the body of a patient to the same extent as it is in the currently used tomographs which typically use the low energy threshold of 300 or 350 keV [23].
In the novel PET system strips of organic scintillators will form a large cylindrical diagnostic chamber as it is shown in Fig. 2.14. Many layers of scintillator strips with

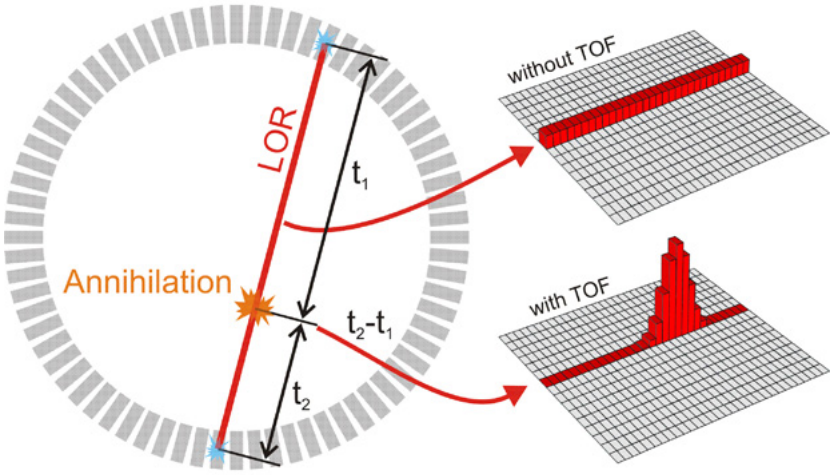

Figure 2.13: PET with and without time of flight method. In case of PET without TOF method the probability of annihilation along the LOR line is homogeneous while with using TOF method only part of LOR line is taken into account in reconstruction [29].

total thickness equal to 5 cm will provide an efficiency of 20% with deposited energy larger than the 200 keV threshold.

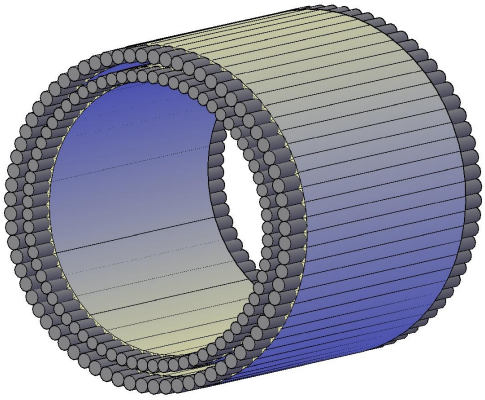

Figure 2.14: Strip J-PET [28].

To each strip of scintillator a photomultiplier will be connected. Photomultipliers will convert light signal to its electrical form. Scheme of two modules is presented in Fig.2.15.

In the novel solution of PET tomograph the knowledge of position of positron annihillation will be provided by time measurements. The distance between the middle point of scintillator and position of interaction of gamma quanta with scintillator

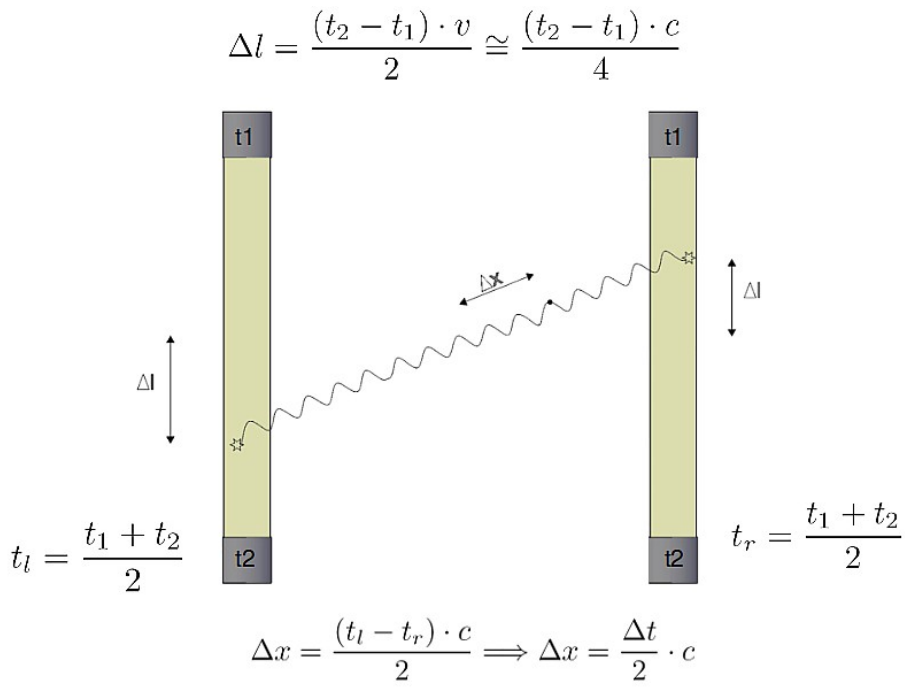

Figure 2.15: Two modules of J-PET diagnostic chamber. t_l (t_r) is a time of γ quantum interaction with left (right) scintillator [30].

material Δl will be calculated as difference between arrival time of signal on a respective photomultipliers multiplied by light velocity inside the scintillator and divided by factor 2. Factor 2 comes from the calculations of Δl. One can take the beginning of the scintillator as 0, the end as L, where L - length of a single scintillator strip, and the middle as $\frac{L}{2}$. One 511-keV photon will travel the distance to photomultiplier equal to $\frac{L}{2} - \Delta$l, and secon photon will travel the distance equal to $\frac{L}{2} + \Delta$l. Therefore:

$$t_2 - t_1 = \frac{\frac{L}{2} - \Delta l}{V} - \frac{\frac{L}{2} + \Delta l}{V} = \frac{-2\Delta l}{V} \tag{2.9}$$

$$\Delta l = \frac{(t_2 - t_1) \times V}{2} \tag{2.10}$$

where V - speed of light inside scintillator, equal to about half of the speed of light in vacuum. In next step point of annhiliation of positron and electon is calculated in a similar way. One can take whole the line of response as x, then Δx will be the distance from the annihilation point to the middle of the LOR. One of the 511-keV photons will travel $x + \Delta x$ and the other will travel $x - \Delta x$. Since the photons travel at speed of light (c), the difference in time (Δt) of arrival of the two photons at the detectors is $\frac{2 \times \Delta x}{c}$ [7].

Even though the probability for independent interaction of two gamma quanta with

2.5 cm thick polymer scintillator material is about 16 times smaller with comparison to the same probability for LSO crystal, in the 3D mode the geometric acceptance of e.g. one meter long chamber will increase on average by a factor of about five in the comparison to the present PET detectors [24]. Additionally, the longitudinal field of view will be five times larger. This properties together give about 25 times bigger probability for annihilation gamma quanta to be registered by the detector. As a result the rate of signals on each photomultiplier will be comparable to the rate in current PET solutions and signal to noise ratio will be about eight times better. The novel PET system will allow for imaging a much larger part of the patient body with unchanged radiopharmaceutical dose. It also increases the probability of detecting of the tumor metastases appearing in the body. The concept of the new scanners may appoint an entirely new path in the field of positron emission tomography and increases the availability of PET equipment for patients.

2.6 Radiopharmaceuticals

The PET radiopharmaceuticals are widely used, mostly in oncology to search for cancerous changes. Their distinguishing feature is beta plus decay of contained radionuclide and its short half-life which results in a significant reduction in the time of their synthesis and clinical use.

Radiopharmaceutical is created as combination of radionuclide and ligand. Ligand is a molecular structure which plays the role of 'vehicle' for radionuclide and it is selected with knowlegde about the target site. The ligand molecules can directly interact with tissue and cels or take part in metabolic processes. Positron emitting isotopes are produced by bombarding targets with charged projectiles. The most important radionuclides are shown in Fig. 2.16.

The most often used radionuclide is ^{18}F because of its long half-life with comparison to other PET isotopes, high part of $\beta+$ decay in decay modes and also relatively low energy of emitted positrons . Fluorine-18 ($t_{\frac{1}{2}} = 110$ min) is produced by irradiation of ^{18}O-water with 10-18 MeV protons in a cyclotron and recovered as ^{18}F-sodium fluoride by passing the irradiated water target mixture through a carbonate type anion exchange resin column. The water passes through, whereas ^{18}F- is retained on the column, which is recovered by elution with potassium carbonate solution [7]. ^{18}F-sodium fluoride is used for receiving ^{18}F-Fluorodeoxyglucose (FDG) which is widely applied in PET. To obtain good image of examined area of the patient body the activity of injected FDG is recommended on the 6 MBq/kg level.

Radionuclide	Half-life	Decay modes (%)	Max. β^+ energy (MeV)
^{11}C	20.4 min	$\beta^+(100)$	0.96
^{13}N	9.96 min	$\beta^+(100)$	1.19
^{15}O	2.03 min	$\beta^+(100)$	1.73
^{18}F	109.8 min	$\beta^+(97)$ EC (3)	0.635
^{124}I	4.2 days	$\beta^+(25)$ EC (75)	2.13
^{64}Cu	12.7 h	$\beta^+(19)$ EC (41)	0.656

Radionuclide	Production method
^{11}C	$^{14}N(p,\alpha)^{11}C$
^{13}N	$^{16}O(p,\alpha)^{13}N$
^{15}O	$^{14}N(d,n)^{15}O$
^{18}F	$^{18}O(p,n)^{18}F$
^{124}I	$^{124}Te(p,n)^{124}I$
^{64}Cu	$^{64}Ni(p,n)^{64}Cu$

Figure 2.16: The most important PET radioactive isotopes and methods of their production. Notation $^{18}O(p,n)^{18}F$ means situation where ^{18}O is a target, p is a projectile, n is emitted and ^{18}F is created. [5]

3 Experimental studies of scintillator shape influence on signals

The main aim of this master thesis is to check how the shape of light pulses is changing in polymer strip scintillators, in other words how the amount of light reaching photomultiplier is changing according to different shapes of scintillators and different point of interaction of gamma quanta. For this purpose analysis of rise and fall time of signals, their amplitude and also signals area according to shape of the scintillator was performed.

3.1 Experimental setup

A series of measurements with different shapes of scintillators were done with ^{68}Ge radioactive source placed in a lead collimator. 50 cm long scintillator connected to two Hamamatsu photomultipliers (model R5320, marked as PM1 and F2) by optical gel and reference detector consisting of BC-404 scintillator and Thorn EMI 9954B photomultiplier were used to make an experimental setup. To sample and store data from photomultipliers, Oscilloscope LeCroy 6000A SDA was used. All photomultipliers were connected to CAEN SY4527 high voltage system.

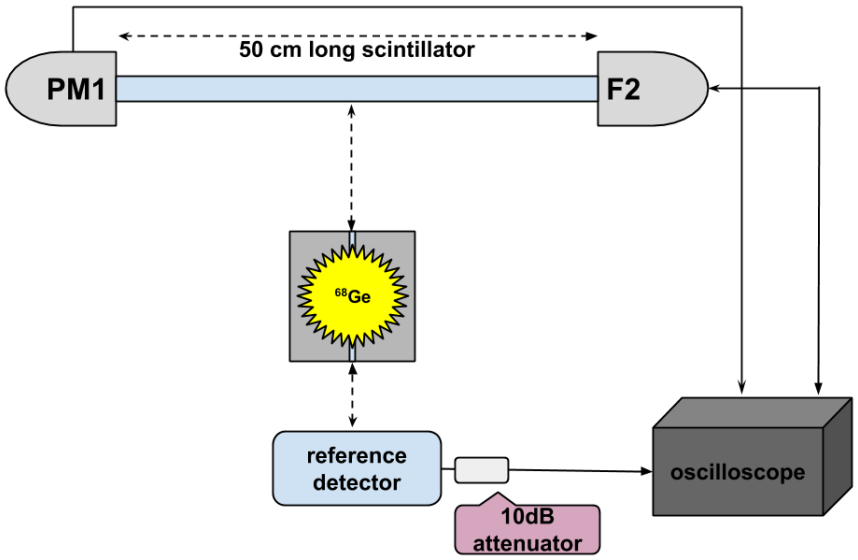

Figure 3.1: Experimental setup for measurements of different scintillator shapes.

Reference detector was connected to the oscilloscope by 10 dB attenuator. Gain of PM1 and F2 photomultipliers were matched to obtain the same amplification.
Each scintillator was wrapped in tyvek foil. Distance between the edge of scintillator

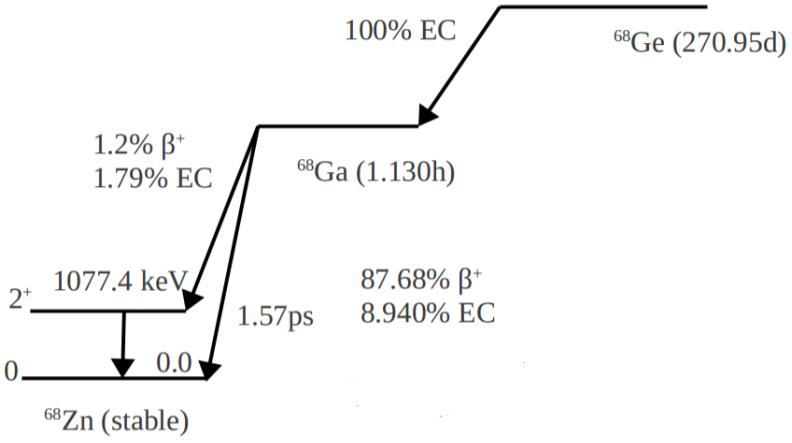

Figure 3.2: Decay scheme of ^{68}Ge [27].

and tyvek wrapping was equal to 0.4 cm on two opposite side of scintillator. ^{68}Ge source was produced in 2013 and its activity was equal to 19200 kBq on April 23, 2013. During the measurements on July activity of radioactive source was equal to about 15527 kBq. Source was placed inside two aluminium discs and then between two lead blocks (20 cm x 10 cm x 5 cm each, see Fig. 3.3).

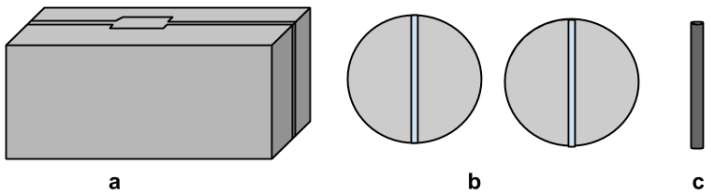

Figure 3.3: Lead collimator with slit between two blocks (20cm x 10cm x 5cm each) (a), two aluminum discs (b) and pencil-like ^{68}Ge source (c).

Measurements were done for square, hexagonal, circular and triangular shapes of scintillator. The dimensions of scintillators are presented in Fig. 3.4.

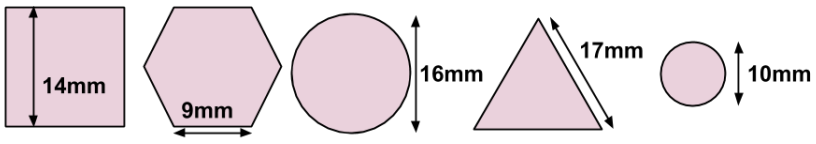

Figure 3.4: Scintillators with cross-section dimensions of measured shapes.

Five positions were measured for each scintillator - center (marked as 25 cm), the edges (marked as 3.2 cm and 46.8 cm) and between them and center position (14.1

cm and 35.9 cm). More details and all oscilloscope settings one can find in Appendix A.
Optical quality of each scintillator strip was checked with ultraviolet lamp. Usage UV lamp allows one to see all damages of scintillator like scratches and cracks. All tests proved that strips were in good condition.

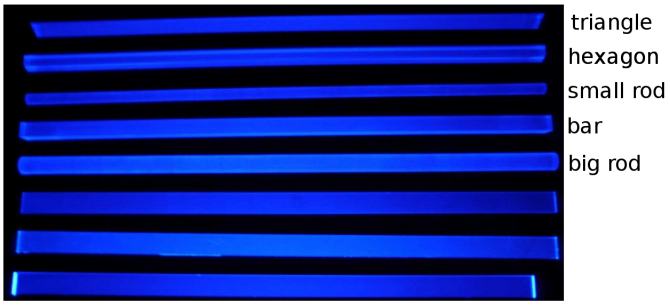

Figure 3.5: Scintillator strips in UV light [27].

3.2 Offset estimation

Offset was calculated for each signal. To calculate offset value the following procedure was done: in first step arithmetic mean of first 20 points of singal in amplitude

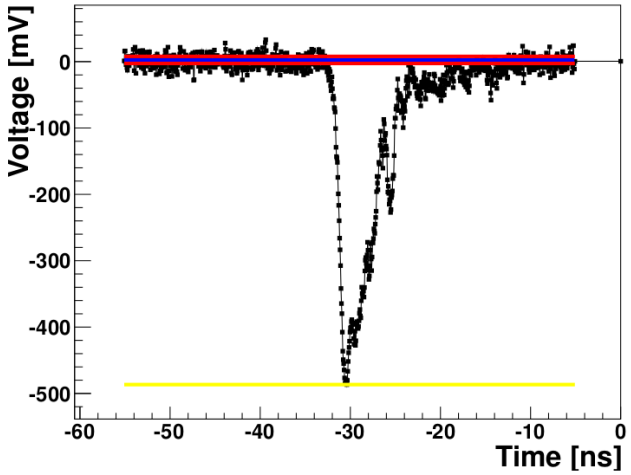

Figure 3.6: Sample signal with signed minimum (yellow line).

domain was computed. This result with plus and minus three standard deviation was treated as a noise. Later, the minimum value of signals was found and program checked point by point the edge of left side from the minumum.

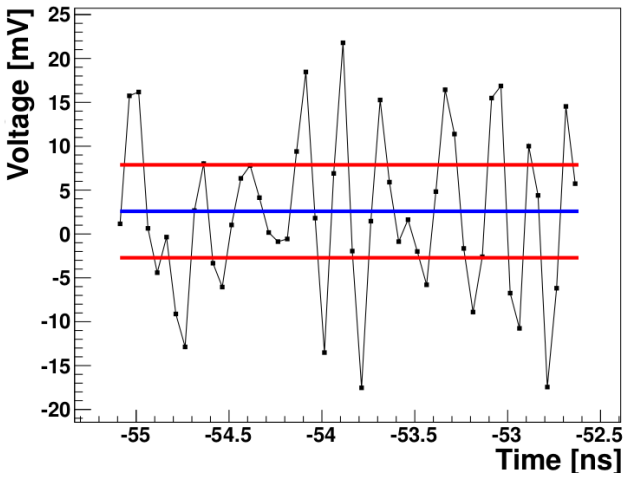

Figure 3.7: First 50 points of this signal with mean value of offset (blue line) with three standard deviation (red line).

When the first point included in noise was found the procedure was canceled and mean value of points from zero to this point was calculated and this value was treated as an offset. Program went deep into noise with checking point by point of signal just to be sure that this tested point is truly in noise range.

3.3 Rise times

For each shape of scintillator signals rise time analysis was performed. Single signal with 10% and 90% fraction marked is shown in Fig. 3.8.

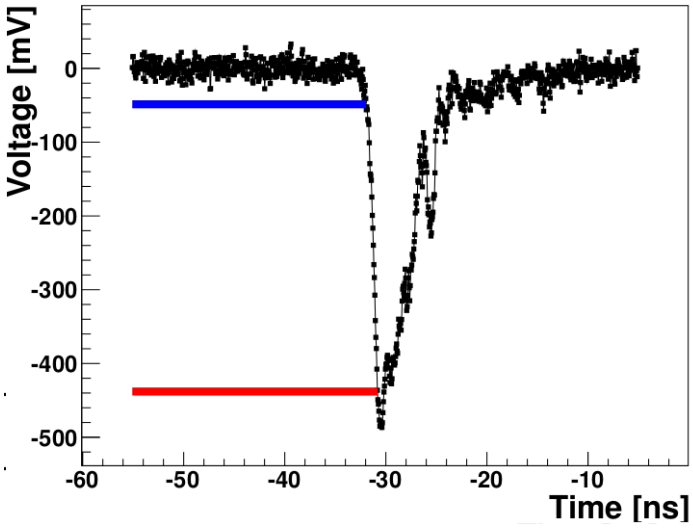

Figure 3.8: Signal with marked 10% (blue line) and 90% (red line) fraction.

Each signal is moved by the offset value. In next step the minimum point of amplitude is located. Minimum of signal has been found because scale is in the negative values. To find appropriate fraction, 10% and 90% of minimum value is calculated. For this results time at fraction is obtained from the following equations:

$$\begin{aligned} y_1 &= a * x_1 + b \\ y_2 &= a * x_1 + b \end{aligned} \tag{3.1}$$

Solving the equations system one can obtain:

$$\begin{aligned} a &= \frac{y_1 - y_2}{x_1 - x_2} \\ b &= y_2 - a * x_2 \end{aligned} \tag{3.2}$$

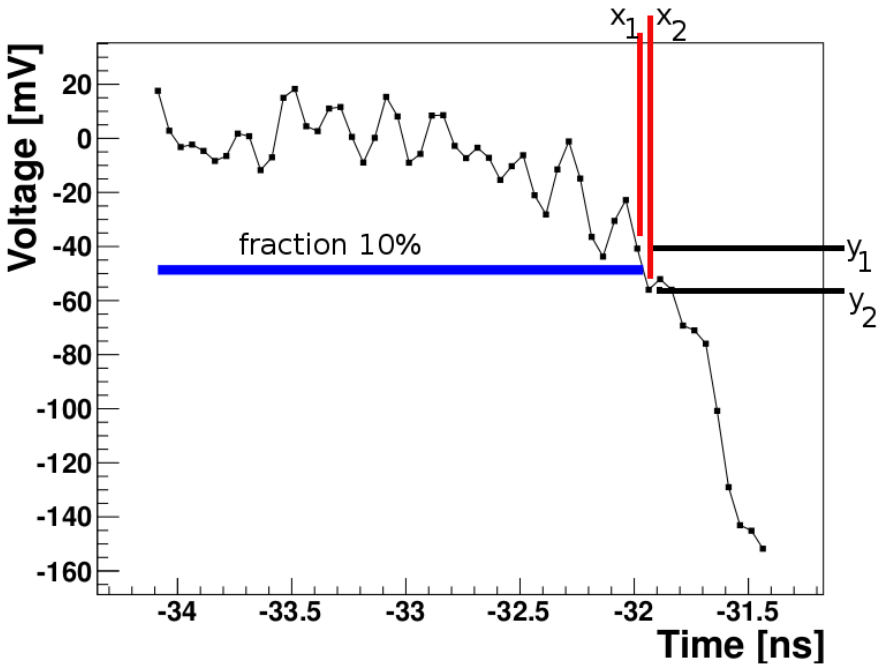

Figure 3.9: Part of signal with marked x_1,x_2, y_1 and y_2. y_1 is an amplitude value above fraction and y_2 is an amplitude value below fraction. x_1 is a time corresponding to amplitude above fraction while x_2 corresponds to amplitude below fraction.

To obtain time on the edge for fraction value (x) one can take value of fraction as y and parameter a and b from above solution of equations system:

$$t_{at\ fraction} = x = \frac{y - b}{a} \tag{3.3}$$

One can receive the time for 10% and 90% fractions and calculate the rise time from the equation:

$$rise\ time = t_{10\%} - t_{90\%} \tag{3.4}$$

where $t_{10\%}$ is time at fraction 10% and $t_{90\%}$ is time at fraction 90%.
Rise time histograms for all five positions of hexagonal shape of scintillator are presented in Fig. 3.10. Histograms of rise time for the rest of scintillators shapes are presented in Appendix B. For each position there is shown histogram of rise times for channel C1 (photomultiplier PM1) and C3 (photomultiplier F2).

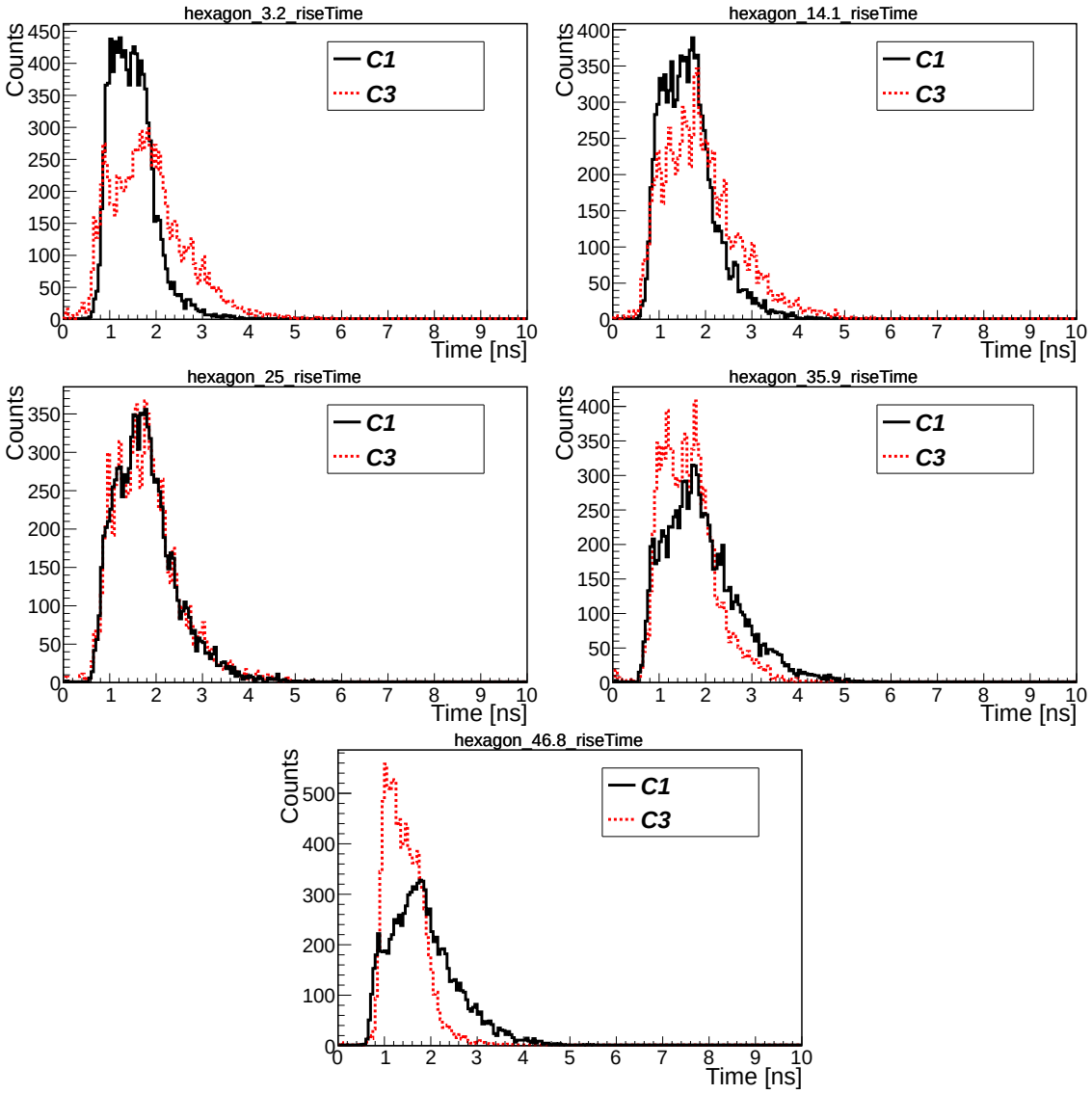

Figure 3.10: Histograms of rise time for hexagon shape of scintillator for position 3.2 cm, 14.1 cm, 25 cm, 35.9 cm and 46.8 cm.

As one can see the histogram of rise time for position 3.2 cm (closer to PM1) for photomultiplier PM1 is narrower than for the photomultiplier F2. Value of rise time is smaller for signals reaching the closer photomultiplier. This situation turns for position 46.8 cm. Histograms of rise time for both photmultipliers are similar for position 25 cm (middle of scintillator strip).
Mean rise time was calculated as the arithmetic mean for each histogram. Mean rise time versus distance from given photomultiplier with extrapolation to zero is shown in Fig. 3.11. Plots for the other photomultiplier are presented in Appendix B.

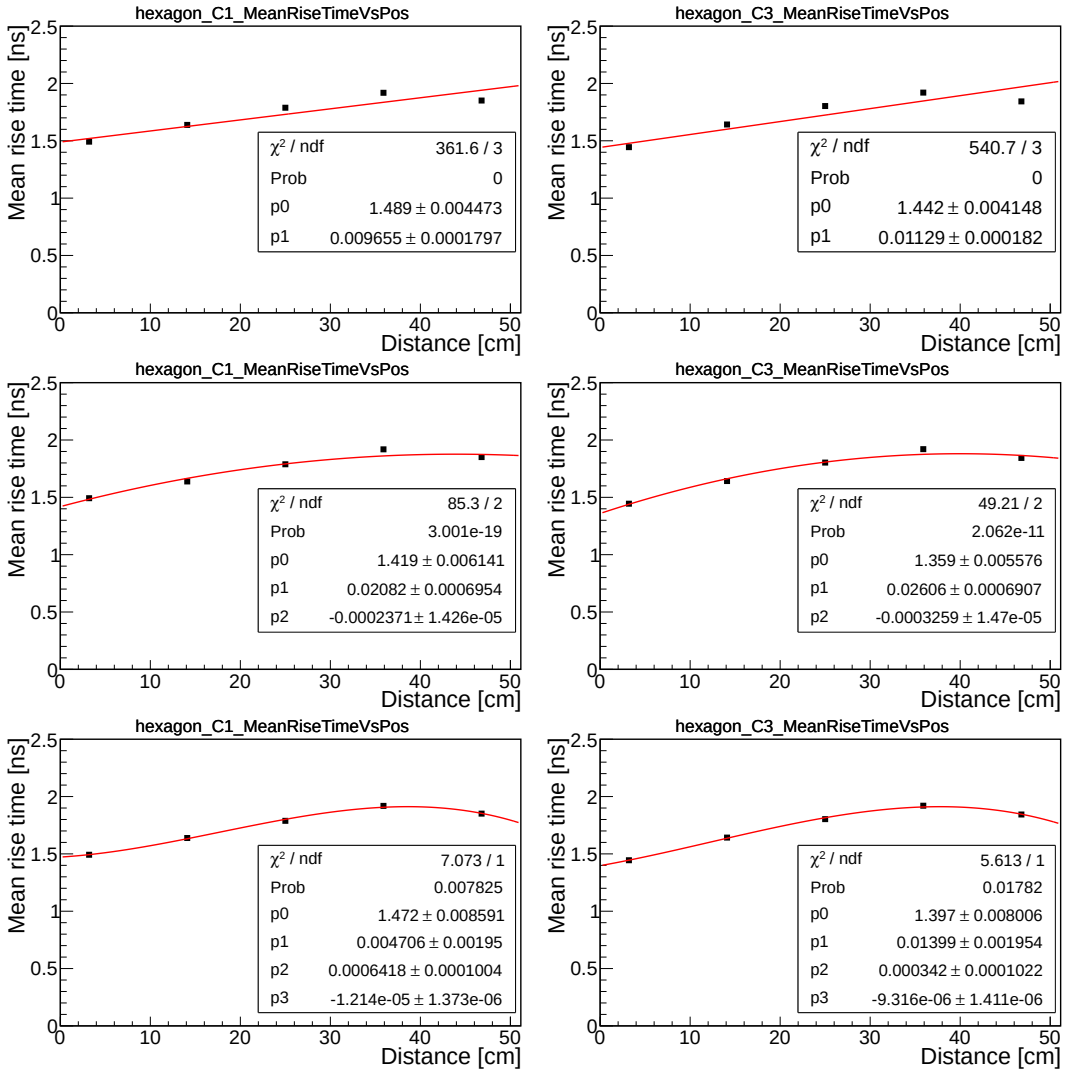

Figure 3.11: Plots of mean rise time versus distance for hexagon shape of scintillator for photomultiplier PM1 (C1) and F2 (C3) with 3 different functions fitted to data points: linear (top pair), quadratic polynomial (central pair) and cubic polynomial (bottom pair).

For each scintillator shape the parameters (p0) of third order polynomial extrapolation line is shown in Tab. 3.1. Third order polynomial was chosen as the best fit as one can see in Fig. 3.11. The values of parameters and errors were rounded to two decimal places.

Shape	Photomultiplier	Parameter p0 [ns]	Uncertainty [ns]
hexagon	PM1	1.47	0.01
	F2	1.40	0.01
big rod	PM1	1.46	0.01
	F2	1.37	0.01
small rod	PM1	1.42	0.01
	F2	1.32	0.01
bar	PM1	1.44	0.01
	F2	1.38	0.01
triangle	PM1	1.44	0.01
	F2	1.37	0.01

Table 3.1: Extrapolation fit parameters of polynomial of degree 3 for different shapes of scintillator.

The last point seen on plots for each photomultiplier behaves strangely (its value is smaller than the value of point before) and this is the reason to study how the mean value of rise time changes when the signal area is greater than the half of the area value on histograms of area etimation . For each position and photomultiplier cuts were selected in the arithmetic mean of area and changed symmetrically as one can see in Tab. 3.2. For example, for each deposition of energy inside the scintillator, signals from photomultipliers had to have area larger than their respective cut values.

Position	Photomultiplier	Value of cut [pC]	Photomultiplier	Value of cut [pC]
3.2 cm	PM1	61	F2	18
14.1 cm	PM1	37	F2	20
25 cm	PM1	28	F2	28
35.9 cm	PM1	20	F2	37
46.8 cm	PM1	18	F2	61

Table 3.2: Value of cuts done on area histograms for hexagon shape of scintillator.

Histograms of signals area for hexagon scintillator shape with cuts are shown in Fig. 3.12. Histograms of area under signals for hexagon scintillator shape before

cuts are shown in Section 3.5. One can see small change in histograms of rise time in Fig. 3.13 and mean rise times verusus distance from photomultipliers after cuts in Fig. 3.14.
All histograms and tables for the rest of scintillators shapes one can find in Appendix B.

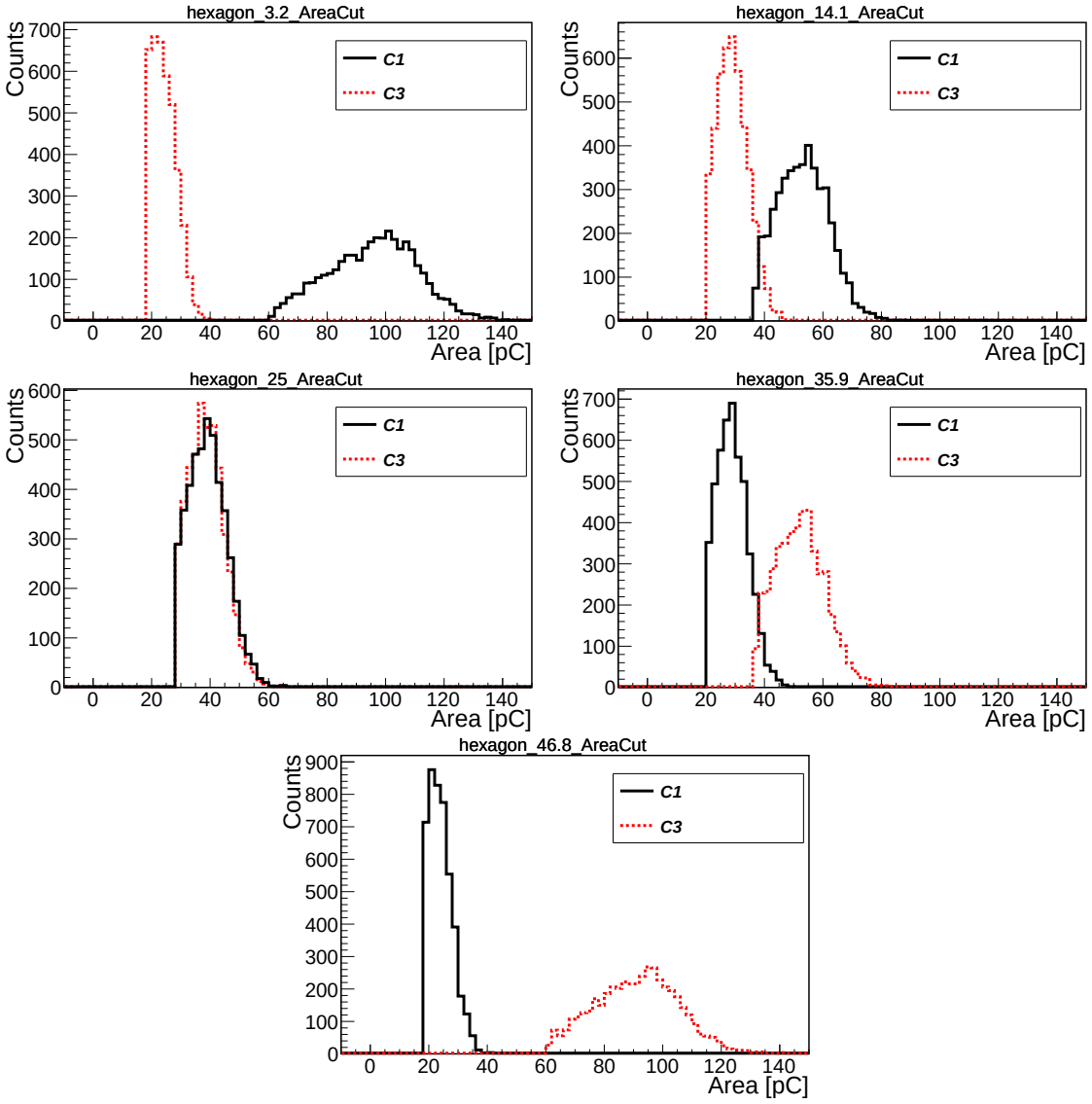

Figure 3.12: Histograms of area after cuts for hexagon scintillator shape for photomultiplier PM1 (C1) and F2 (C3) for all five positions.

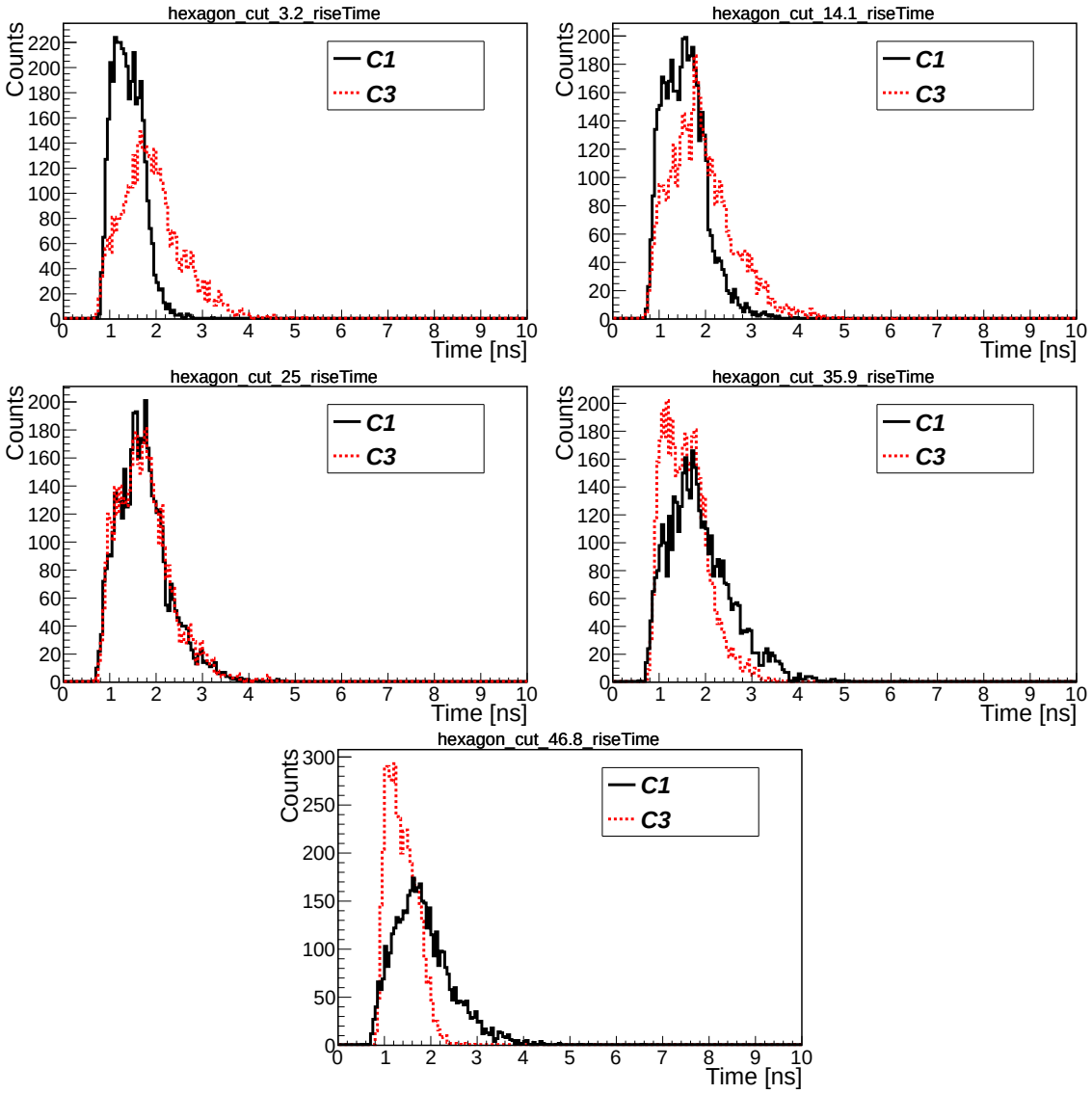

Figure 3.13: Histograms of rise time after cuts for hexagon shape of scintillator for all five positions.

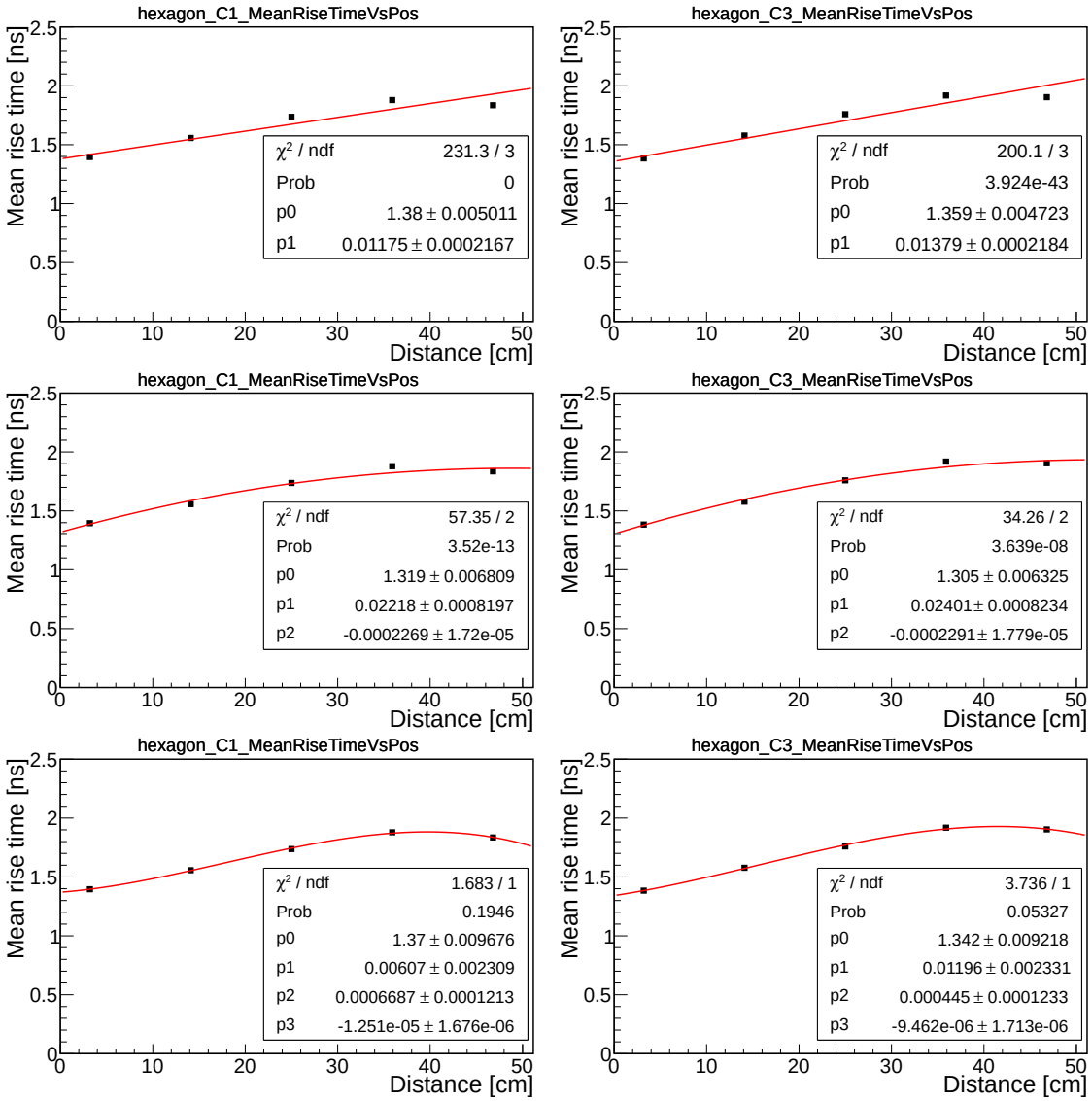

Figure 3.14: Plots of mean rise time versus distance after cuts for hexagon scintillator shape for photomultiplier PM1 (C1) and F2 (C3) with 3 different functions fitted to data points: linear (top pair), quadratic polynomial (central pair) and cubic polynomial (bottom pair).

Shape	Photomultiplier	Parameter p0 [ns]	Uncertainty [ns]
hexagon	PM1	1.37	0.01
	F2	1.34	0.01
big rod	PM1	1.34	0.01
	F2	1.34	0.01
small rod	PM1	1.32	0.01
	F2	1.32	0.01
bar	PM1	1.35	0.01
	F2	1.33	0.01
triangle	PM1	1.35	0.01
	F2	1.34	0.01

Table 3.3: Extrapolation fit parameters after cuts for different shapes of scintillator.

Shape	Photomultiplier	Parameter p0 before cut [ns]	Parameter p0 after cut [ns]	Uncertainty [ns]
hexagon	PM1	1.47	1.37	0.01
	F2	1.40	1.34	0.01
big rod	PM1	1.46	1.34	0.01
	F2	1.37	1.34	0.01
small rod	PM1	1.42	1.32	0.01
	F2	1.32	1.32	0.01
bar	PM1	1.44	1.35	0.01
	F2	1.38	1.33	0.01
triangle	PM1	1.44	1.35	0.01
	F2	1.37	1.34	0.01

Table 3.4: Comparison of extrapolation fit parameters before and after cuts for different shapes of scintillator.

As one can see histograms of rise time for hexagon scintillator after cuts change a little its shape and also one can noticed that the number of counts is smaller than before. The same behavior is observed for all shapes of scintillator. The value of χ^2/ndf, where ndf denotes the number of degrees of freedom, is closer to 1 after cuts in plots of mean rise time versus distance from given photomultiplier with cubic fit. One can see in Tab. 3.4 that extrapolation fit parameters (p0) of cubic polynomial is smaller after cut than before it. The finding is that after cuts fit better decribes points from analysis. On the other hand making the cut do not improve a lot the value of rise time of signals reaching the photmultpilier. Rise time should depend

on point of interaction of gamma quanta with scitntillators material and not on the shape of scintillator. Only this light signals have impact on rise time which directly hit the photomultiplier window (without any internal reflections).
Rise time of EJ-230 is equal to 0.5 ns and of R5320 Hamamatsu photomultiplier is equal to 0.7 ns. The results obtained by the analysis shown in Tab. 3.4 can be a result of the light propagation and its different path inside scintillator and also rise time imposed by used photomultipliers.

3.4 Fall times

For each scintillator shape analysis of signals fall time was done. Single signal with 10% and 90% fraction marked on the falling slope is shown in Fig. 3.15.

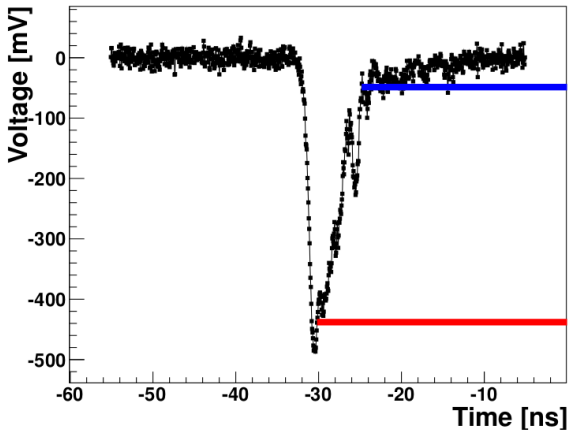

Figure 3.15: Signal with marked 10% (blue line) and 90% (red line) fraction.

For further calculations each signal is moved to zero with the offset value. All calculations are similar to those of rise time estimation. The minimum of signal (amplitude) is found once again.
Time at fraction is obtained from the same equations as it was for rise time estimation. One can calculate the fall time from the equation:

$$fall\ time = t_{10\%} - t_{90\%} \tag{3.5}$$

where $t_{10\%}$ is time at fraction 10% and $t_{90\%}$ is time at fraction 90%.
Results of fall times for hexagon scintillator shape and for each position are presented below in Fig. 3.17. Histograms and plots for the rest of scintillator shapes are presented in Appendix C.
The shapes of histograms of fall time may be caused by big value of this time. During the time equal to about 5 ns for hexagon scintillator shape the photomultiplier

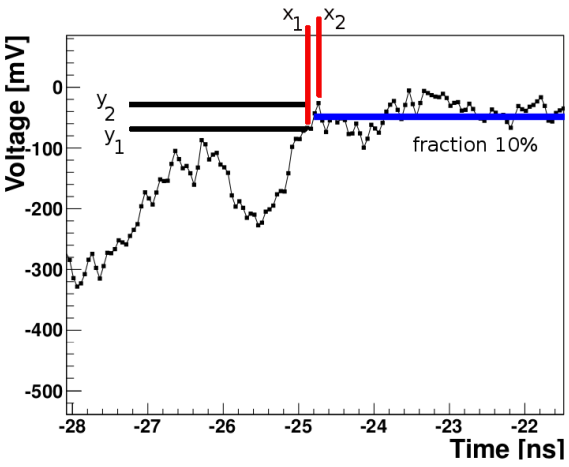

Figure 3.16: Part of signal with marked x_1,x_2, y_1 and y_2. y_1 is an amplitude below fraction, y_2 is an amplitude above fraction when x_1 and x_2 is a time corresponding to amplitude below and above fraction.

can be reached by more then one light signals and when photomultiplier record one light signal second reaching PMT can gives some contribution to this signal.

Shape	Photomultiplier	Parameter p0 [ns]	Uncertainty [ns]
hexagon	PM1	4.39	0.02
	F2	4.99	0.02
big rod	PM1	4.74	0.02
	F2	5.48	0.02
small rod	PM1	4.41	0.02
	F2	5.17	0.02
bar	PM1	4.38	0.02
	F2	5.07	0.02
triangle	PM1	4.25	0.02
	F2	4.95	0.02

Table 3.5: Extrapolation fit parameters for fall time for different shapes of scintillator.

Mean fall time versus distance from given photomultiplier with extrapolation to zero for hexagon shape of scintillator is shown in Fig. 3.18. For each plot 3 different kinds of fit were done - linear fit, quadratic polynomial and polynomial of third order as it was for rise time estimation. For each scintillator shape the fit parameters (p0) of extrapolation line for cubic polynomial rounded to two decimal places is shown is Tab. 3.5. Plots for the other scintillator shapes are presented in Appendix C.

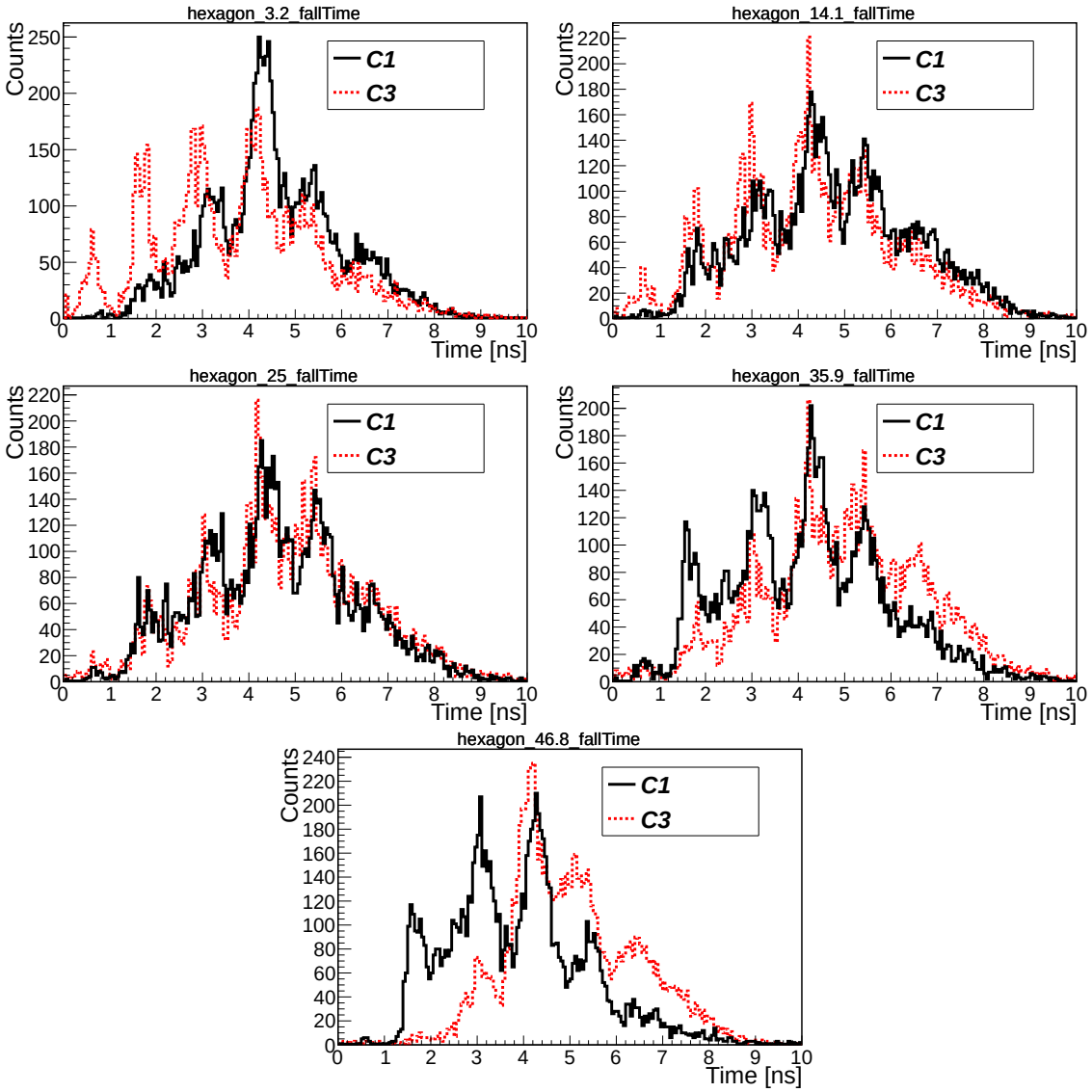

Figure 3.17: Histograms of fall time for hexagon shape scintillator for position 3.2 cm, 14.1 cm, 25 cm, 35.9 cm and 46.8 cm.

The first point for each photomultiplier behaves strangely (similar behavior as in histograms for mean rise time versus position) and this is once again the reason to study how the histograms of fall time and fall time mean value change when the area under signal is greater than the half of the area value. For each position and photomultiplier cuts were the same as in section 3.3. Histograms of area under signals after cuts for hexagon scintillator shape are shown in section 3.3 in Fig. 3.12 and for the other scintillator shapes in Appendix B.

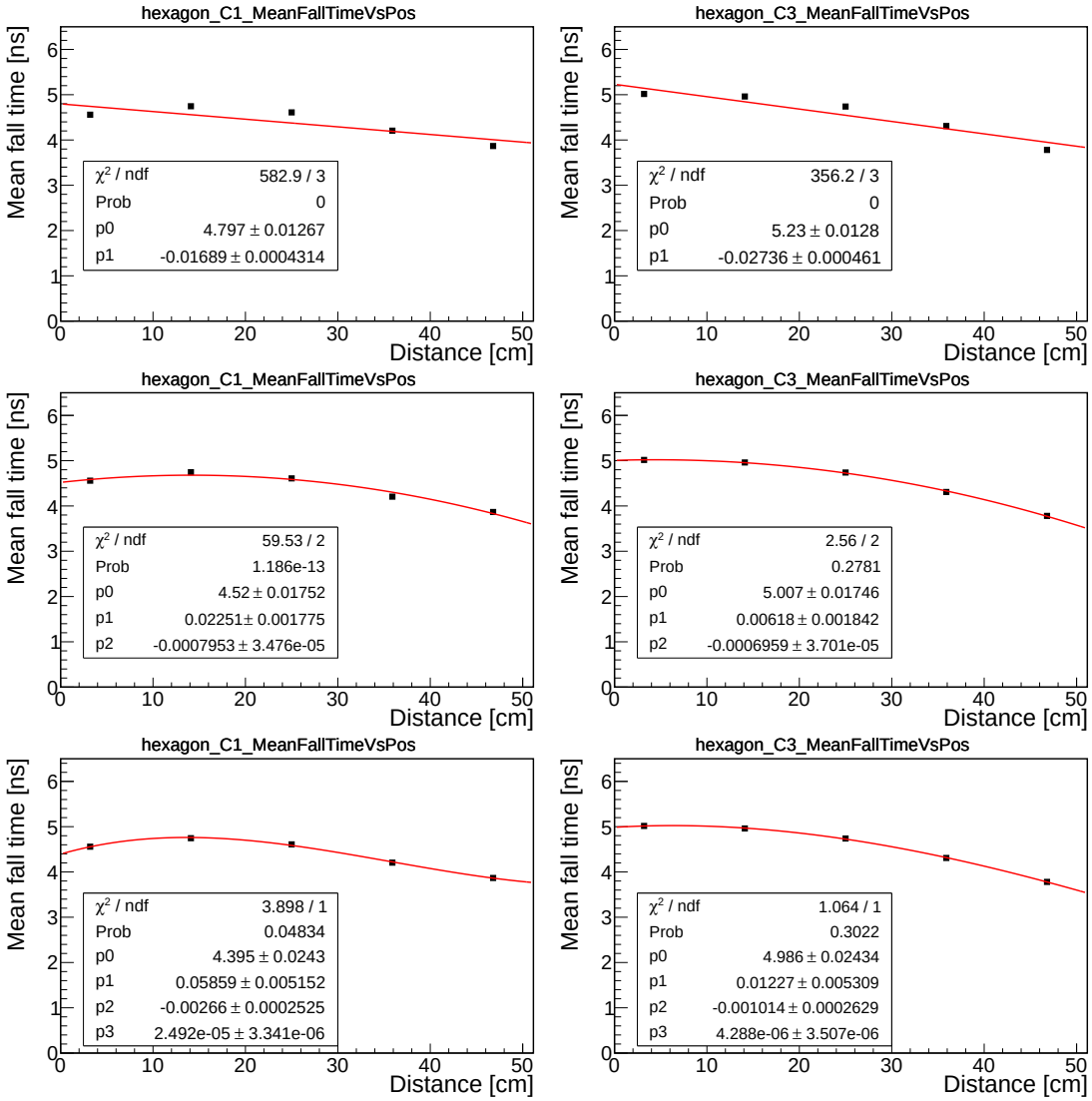

Figure 3.18: Plots of mean fall time versus distance for hexagon shape of scintillator for photomultiplier PM1 (C1) and F2 (C3) with 3 different functions fitted to data points: linear (top pair), quadratic polynomial (central pair) and cubic polynomial (bottom pair).

Histograms of fall time after cuts for hexagon shape of scintillator seen in Fig. 3.19 are narrower in comparison to Fig. 3.17 and changed their shape. The same behavior is observed for the rest of scintillator shapes and was observed for the rise time. Plots of mean fall time versus distance after cuts for hexagon shape is shown in Fig. 3.20. Histograms of fall time and plots of mean fall time versus distance from given photomultiplier with extrapolation lines one can find in Appendix C.

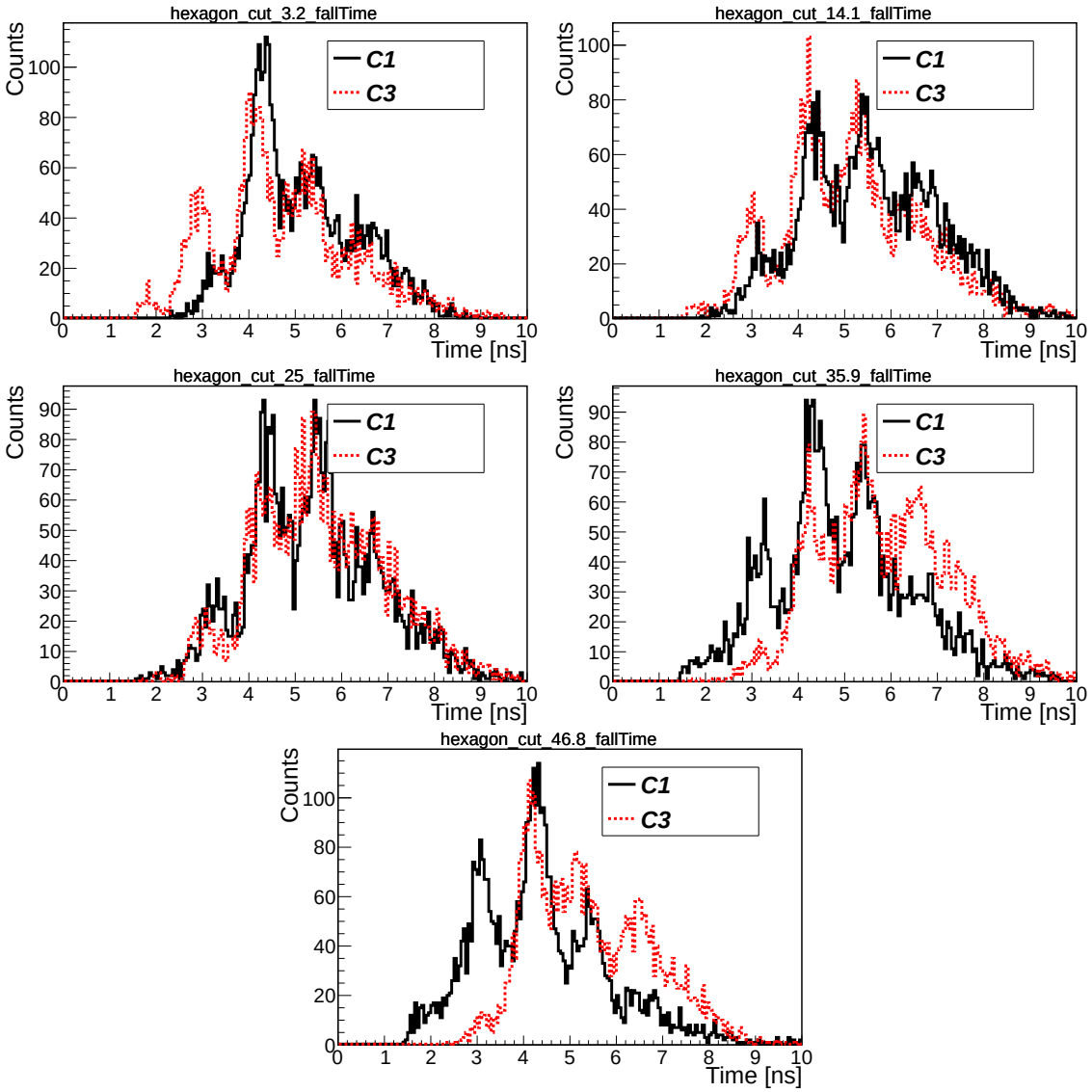

Figure 3.19: Histograms of fall time after cuts for hexagon shape scintillator for position 3.2 cm, 14.1 cm, 25 cm, 35.9 cm and 46.8 cm.

Dependence between mean fall time and distance to photomultiplier is not linear in contrast to the predictions (the same behaviour was observed in analysis of mean rise time versus distance to given photomultiplier) as one can see on plots for hexagon shape of scintillator in Fig. 3.20. For cubic polynomial fit for different shapes of scintillator the value of χ^2/ndf is nearest to 1 after cut than for the rest of fitted polynomials.

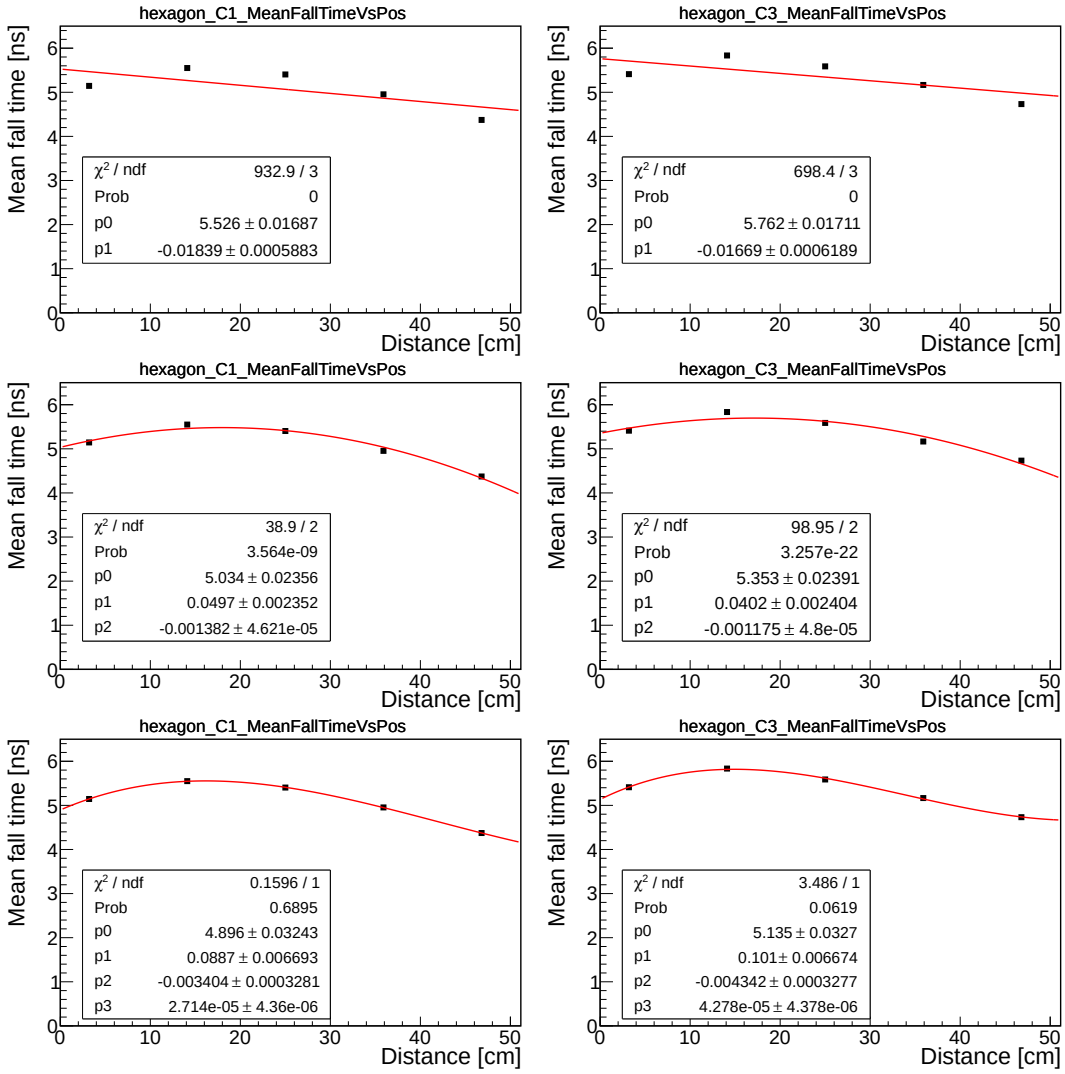

Figure 3.20: Plots of mean fall time versus distance after cuts for hexagon shape of scintillator for photomultiplier PM1 (C1) and F2 (C3) with 3 different functions fitted to data points: linear (top pair), quadratic polynomial (central pair) and cubic polynomial (bottom pair).

For each scintillator shape the fit parameters (p0) of cubic polynomial extrapolation line after cuts is shown in Tab. 3.6. Cubic polynomial fit was chosen as the best one. The value of parameters and errors were rounded to two decimal places.
In Tab. 3.7 one can see the comparison between cubic polynomal fit parameter p0 before and after cuts. After cuts the fit parameter p0 is bigger than before and their difference is also bigger. This is contrary to the behavior of p0 for rise time estimation. The decay time of EJ-230 scintillator is equal to 1.5 ns, so the mean value of fall time equal to about from 5 ns to 6 ns for all scintillators can strongly

depend on geometry of scintillator and internal refraction of light signals.

Shape	Photomultiplier	Parameter p0 [ns]	Uncertainty [ns]
hexagon	PM1	4.90	0.03
	F2	5.14	0.03
big rod	PM1	5.23	0.04
	F2	5.67	0.03
small rod	PM1	4.92	0.04
	F2	5.21	0.03
bar	PM1	4.93	0.03
	F2	5.24	0.03
triangle	PM1	4.65	0.03
	F2	5.04	0.03

Table 3.6: Extrapolation fit parameters for fall time after cuts for different shapes of scintillator.

Shape	Photomultiplier	Parameter p0 before cut [ns]	Uncertainty [ns]	Parameter p0 after cut [ns]	Uncertainty [ns]
hexagon	PM1	4.39	0.02	4.90	0.03
	F2	4.99	0.02	5.14	0.03
big rod	PM1	4.74	0.02	5.23	0.04
	F2	5.48	0.02	5.67	0.03
small rod	PM1	4.41	0.02	4.92	0.04
	F2	5.17	0.02	5.21	0.03
bar	PM1	4.38	0.02	4.93	0.03
	F2	5.07	0.02	5.24	0.03
triangle	PM1	4.25	0.02	4.65	0.03
	F2	4.95	0.02	5.04	0.03

Table 3.7: Comparison of extrapolation fit parameters before and after cuts for different shapes of scintillator.

3.5 Areas

Area analysis was done for each scintillator shape and each position. Area under each signal is proportional to light reaching to photomultiplier. Each signal was moved to zero with offser value and then the value of area was calculated. Results for position

3.2 cm, 14.1 cm, 25 cm. 35.9 cm and 46.8 cm without any cuts for hexagon shape of scintillator are presented in figures in this section. Results for the rest of scintillator shapes are presented in Appendix D.

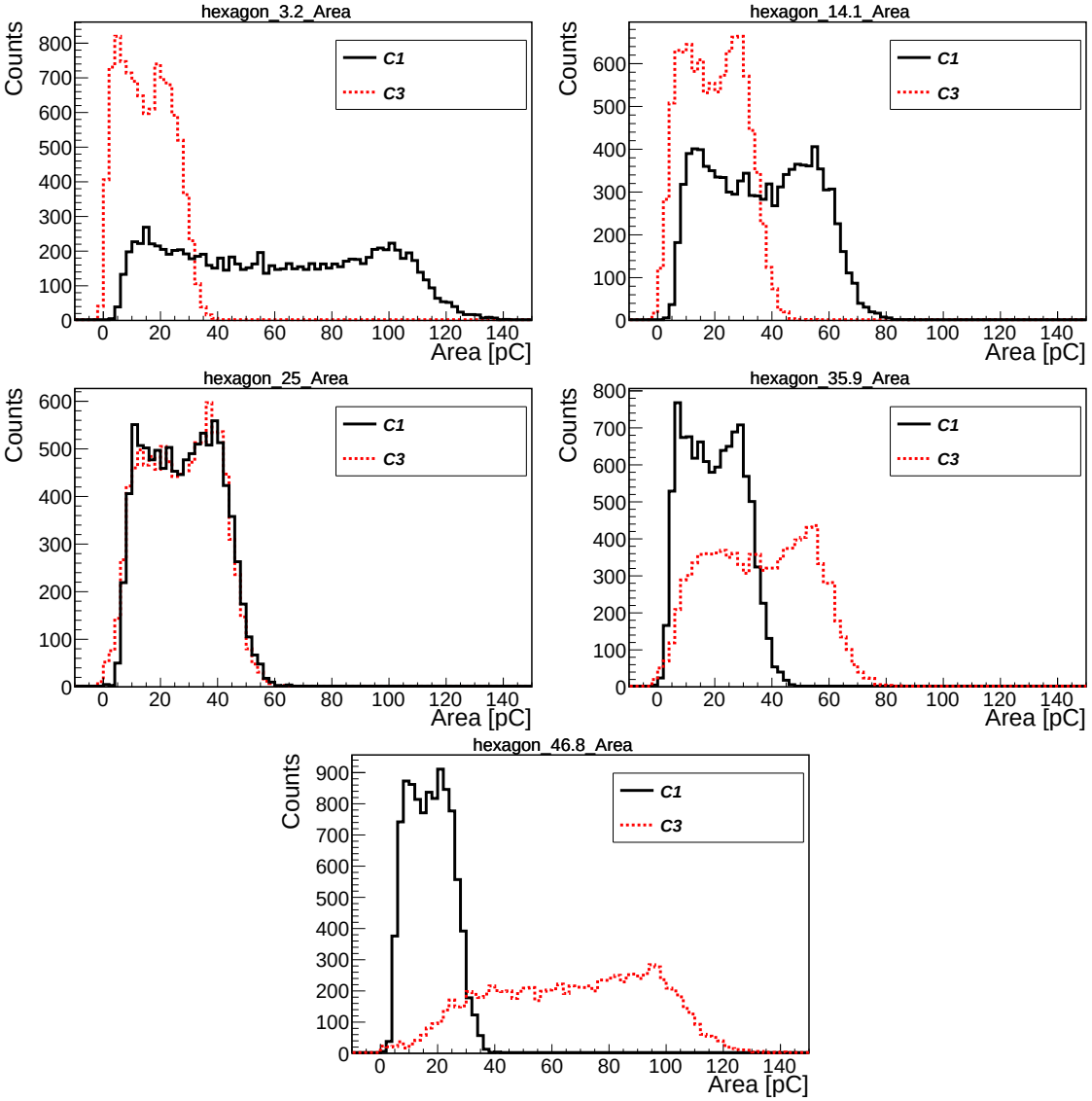

Figure 3.21: Histograms of area under signals for hexagon shape of scintillator for all five positions.

In the middle position area under signals for both photomultipliers look similarly. It means that the amplifications of photomultipliers were well chosen and were similar to each other. For small rod shape of scintillator a peak near zero value of area for position equal to 25 cm can be caused by some external light which probably got into the experimental setup.
For each scintillator shape value of area on the half on Compton edge was estimated

for middle position and is presented in Tab. 3.8. The middle point on the Compton energy corresponds to the maximum energy deposition of gamma quanta. In table is also presented relative light output for scintillator shapes, where hexagon shape of scintillator was chosen as reference detector.

Shape	Area value [pC]	Relative light output	cross section area [mm^2]
hexagon	44	100%	210.44
big rod	37	84%	201.06
small rod	32	73%	78.54
bar	41	93%	196
triangle	36	82%	125.14

Table 3.8: Comparison between area for different scintillator shapes in position equal to 25 cm.

The biggest value of area was observed for hexagon shape. When the scintillator cross section has smaller number of angles then the area is also smaller and this can be caused by internal reflection of light inside scintillator. The smaller area was obtained for small rod shape of scintillator. The conclusion is that the scintillator shape and its cross section area can impact on area under observed signals.

3.6 Amplitudes

Signals amplitude analysis was done for each scintillator shape and each position. Results for position 3.2 cm, 14.1 cm, 25 cm, 35.9 cm and 46.8 cm for hexagon shape of scintillator are presented in figures in this section. Results for the rest scintillator shape one can find in Appendix E.
Each signal was moved to zero with the offset value. Amplitude was calculated by finding the minimum point of signal. To plot histograms abosolute value of amplitude from each signal was taken.
The biggest amplitude values are observed in position nearest to appropriate photomultiplier, for PM1 the bigest amplitude values is for position 3.2 cm while for F2 in position 46.8 cm.
Similar analysis was done for the amplitude as it was for area etimation. For each scintillator shape the amplitude value on the half on the edge for position equal to 25 cm was estimated and is presented in Tab. 3.9.
As one can see estimated amplitude of signal also changed with the scintillator shape. The biggest is for scintillator shape with the bigger number of angles. It was predicted after analysis of area because area of signal is related with its shape and amplitude.

Shape	Amplitude [mV]	Relative proportion
hexagon	459	100%
big rod	390	85%
small rod	379	83%
bar	456	99%
triangle	430	94%

Table 3.9: Comparison between amplitude value for different scintillator shapes in position equal to 25 cm.

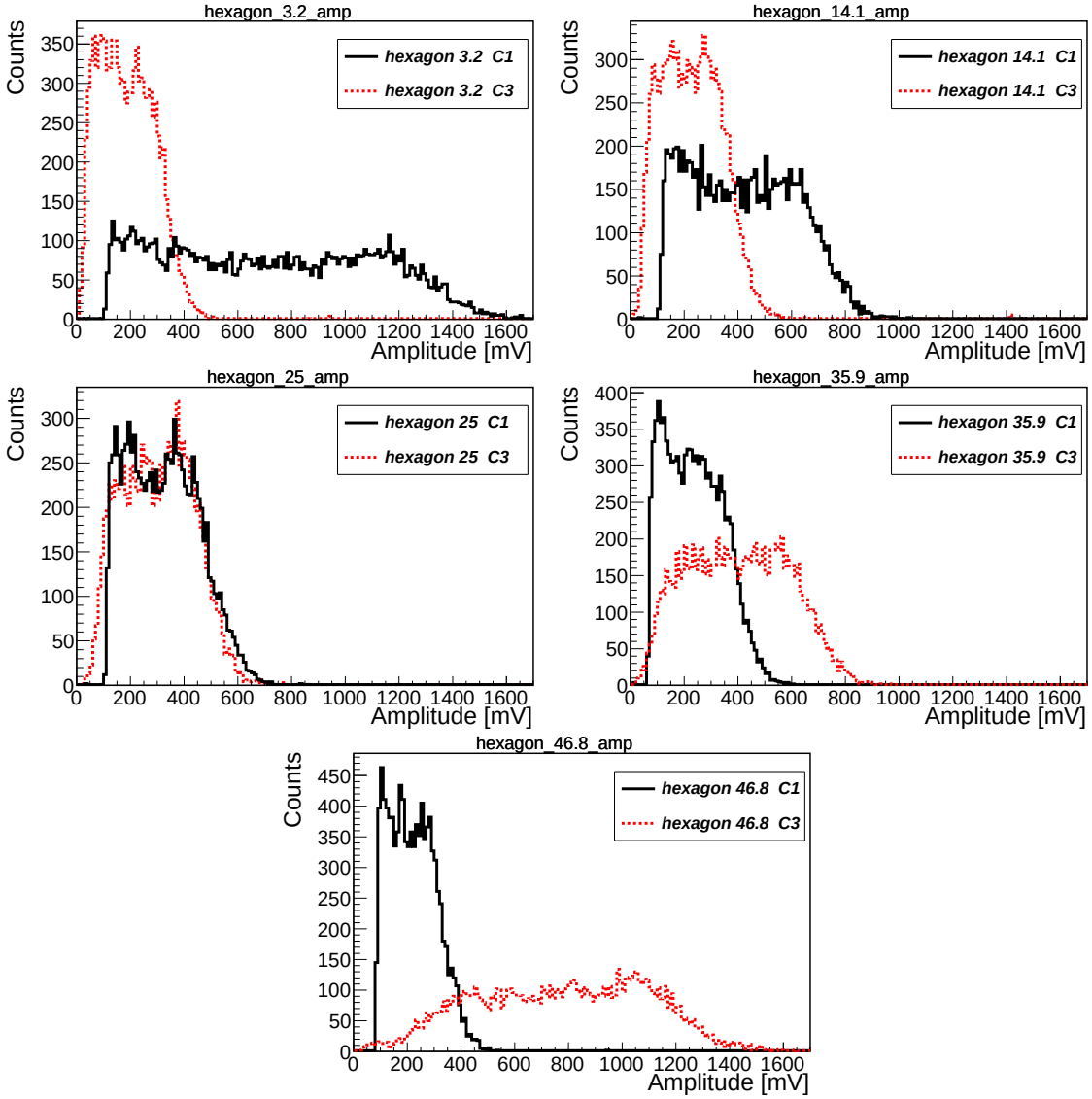

Figure 3.22: Histograms of signals amplitude for hexagon shape of scintillator for position 3.2 cm, 14.1 cm, 25 cm, 35.9cm and 46.8 cm.

4 Summary and conclusions

The aim of this thesis was to check how signals properties depend on the scintillator shape. For this purpose rise and fall time, area under signals and amplitude analysis were performed.

γ quanta originating from ^{68}Ge radioactive source placed in lead collimator hit the scintillator situated between two Hamamatsu photomultipliers. Signals were recorded by LeCroy Oscilloscope. For each measurement about 10 000 events were collected. Five positions along each strip were irradiated: the edges, the center and quarters.

The results for rise time implies that it depends on point of interaction of gamma quanta with scintillators material and not on the shape of scintillator. For each photomultiplier and irradiation position cuts on area were performed taking into account only signals with area larger than half of the maximum area. Making a cut does not change signals rise time.

Area under signal depend stongly on irradiation position and is the bigest for position nearest to given photomultiplier. Value of area on the half on Compton edge was estimated in the middle position for all scintillators shapes. This estimation has highlighted the relation between value of area and shape and cross sestion of scintillator. The biggest value was obtained for hexagon shape and the smallest for small rod shape of scintillator.

In case of amplitude, the same results was observed as for area analysis. Amplitude reached the biggest value in position nearest to given photomultiplier. Amplitude of signal also changed with the scintillator shape and was the biggest for shape with the biggest number of sides.

Appendix A - experimental details about different shapes measurements

Voltage on PM1 was equal to 2290 and on F2 was equal to 2000V. Voltage on reference detector was always equal to 1800V. PM1 was connected to channel 1 of the oscilloscope while F2 and reference detecor were connected respectively to channel 3 and channel 4 of the oscilloscope. Power suply of photomultipliers was guaranteed by CAEN SY4527 high voltage system. Trigger was always qualified negative after qualifier C1 has gone below -60mV before 60ns.

Scionix EJ-230 Plastic Hexagon Shape Scintillator (500mm x 9mm sides)
Scionix EJ-230 Plastic Bar Shape Scintillator (500mm x 14mm x 14mm)
Scionix EJ-230 Plastic Equilateral Triangle Shape Scintillator (500mm x 17mm)
All of this shapes had the same oscilloscope settings during measurements of each positions.

C1 DC50Ω	C3 DC50Ω	Timebase settings	Trigger C4
250mV/div 945mV offset	100mV/div 378.0mV offset	30.1ns 5.00ns/div 20GS/s	normal -5.6mV

Table A.1: Oscilloscope settings for position 3.2cm.

C1 DC50Ω	C3 DC50Ω	Timebase settings	Trigger C4
250mV/div 945mV offset	150mV/div 584.0mV offset	30.1ns 5.00ns/div 20GS/s	normal -5.6mV

Table A.2: Oscilloscope settings for position 14.1cm.

C1 DC50Ω	C3 DC50Ω	Timebase settings	Trigger C4
250mV/div 945mV offset	250mV/div 945mV offset	30.1ns 5.00ns/div 20GS/s	normal -5.6mV

Table A.3: Oscilloscope settings for position 25cm.

C1 DC50Ω	C3 DC50Ω	Timebase settings	Trigger C4
150mV/div 584.0mV offset	250mV/div 945mV offset	30.1ns 5.00ns/div 20GS/s	normal -5.6mV

Table A.4: Oscilloscope settings for position 35.9cm.

C1 DC50Ω	C3 DC50Ω	Timebase settings	Trigger C4
100mV/div 378.0mV offset	250mV/div 945mV offset	30.1ns 5.00ns/div 20GS/s	normal -5.6mV

Table A.5: Oscilloscope settings for position 46.8cm.

Scionix EJ-230 Plastic Rod Shape Scintillator (500mm x 16mm dia)
Scionix EJ-230 Plastic Rod Shape Scintillator (500mm x 10mm dia)

C1 DC50Ω	C3 DC50Ω	Timebase settings	Trigger C4
250mV/div 945mV offset	50mV/div 189.0mV offset	30.1ns 5.00ns/div 20GS/s	normal -5.6mV

Table A.6: Oscilloscope settings for position 3.2cm.

C1 DC50Ω	C3 DC50Ω	Timebase settings	Trigger C4
250mV/div 945mV offset	100mV/div 378.0mV offset	30.1ns 5.00ns/div 20GS/s	normal -5.6mV

Table A.7: Oscilloscope settings for position 14.1cm.

C1 DC50Ω	C3 DC50Ω	Timebase settings	Trigger C4
250mV/div 945mV offset	250mV/div 945mV offset	30.1ns 5.00ns/div 20GS/s	normal -5.6mV

Table A.8: Oscilloscope settings for position 25cm.

C1 DC50Ω	C3 DC50Ω	Timebase settings	Trigger C4
100mV/div 378.0mV offset	250mV/div 945mV offset	30.1ns 5.00ns/div 20GS/s	normal -5.6mV

Table A.9: Oscilloscope settings for position 35.9cm.

C1 DC50Ω	C3 DC50Ω	Timebase settings	Trigger C4
50mV/div 189.0mV offset	250mV/div 945mV offset	30.1ns 5.00ns/div 20GS/s	normal -5.6mV

Table A.10: Oscilloscope settings for position 46.8cm.

Appendix B - rise time spectra

Rise time spectra for different scintillator shapes

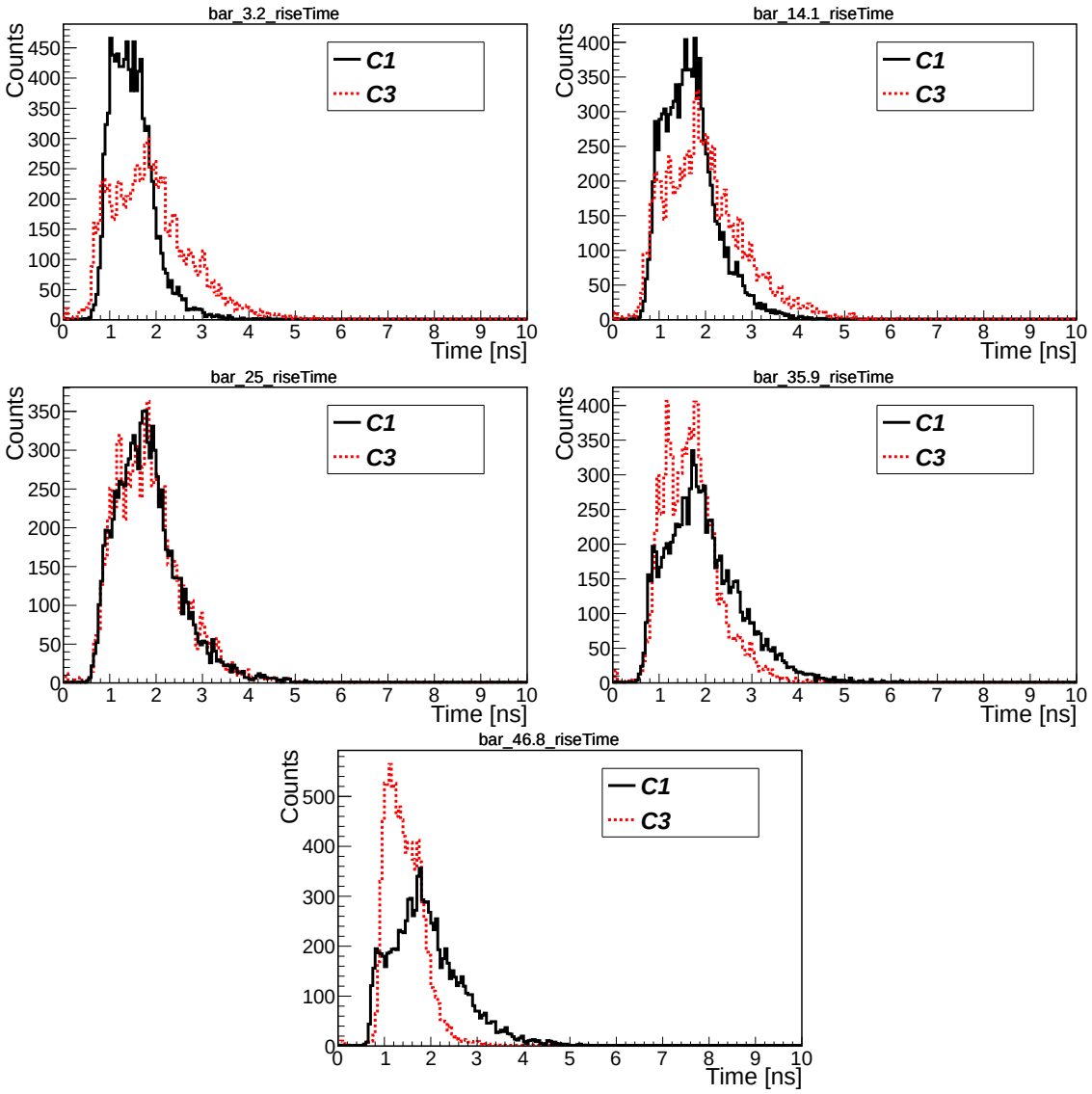

Figure B.1: Histograms of rise time for bar shape of scintillator for position 3.2 cm, 14.1 cm, 25 cm, 35.9 cm and 46.8 cm.

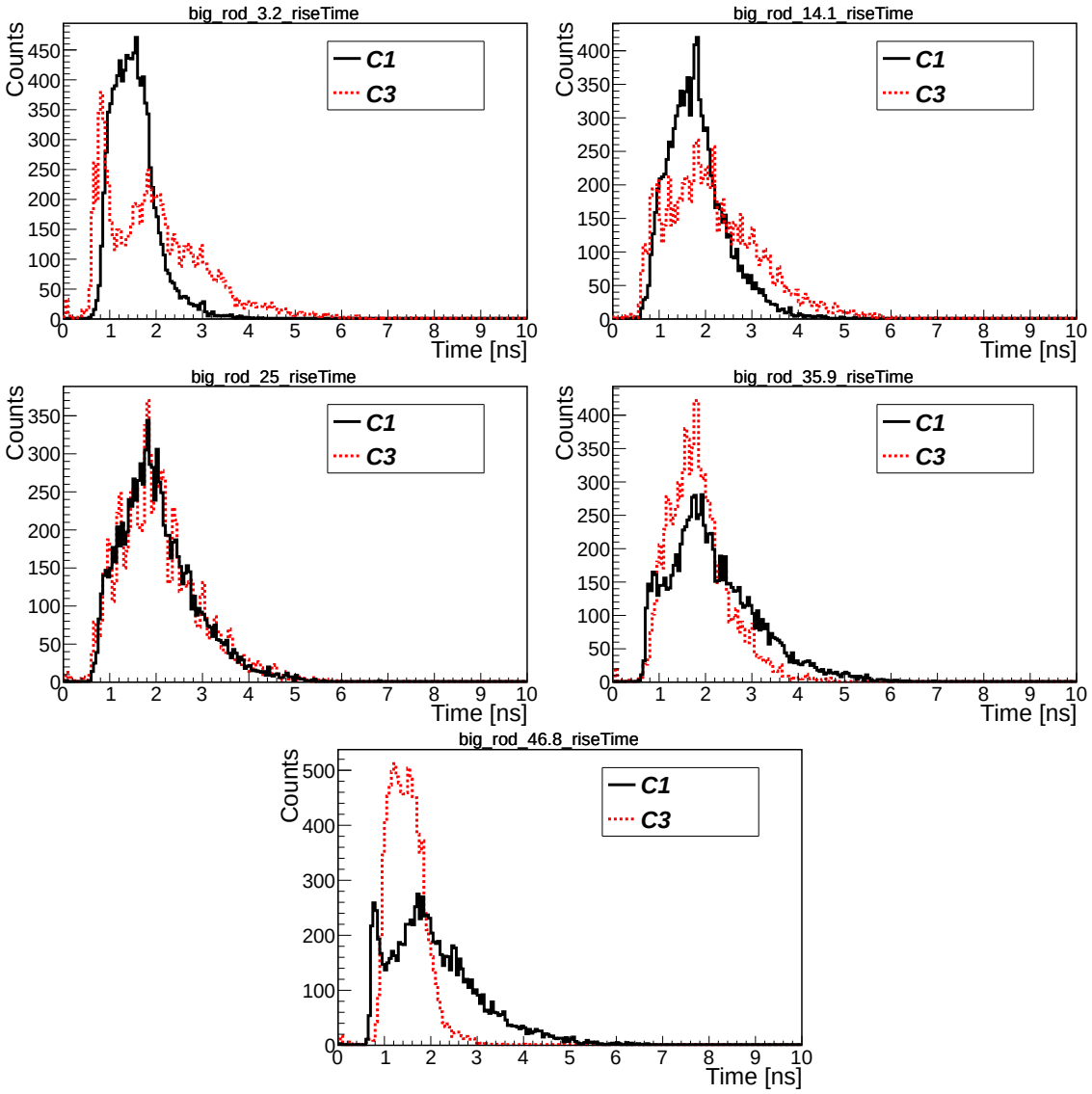

Figure B.2: Histograms of rise time for big rod shape of scintillator for position 3.2 cm, 14.1 cm, 25 cm, 35.9 cm and 46.8 cm.

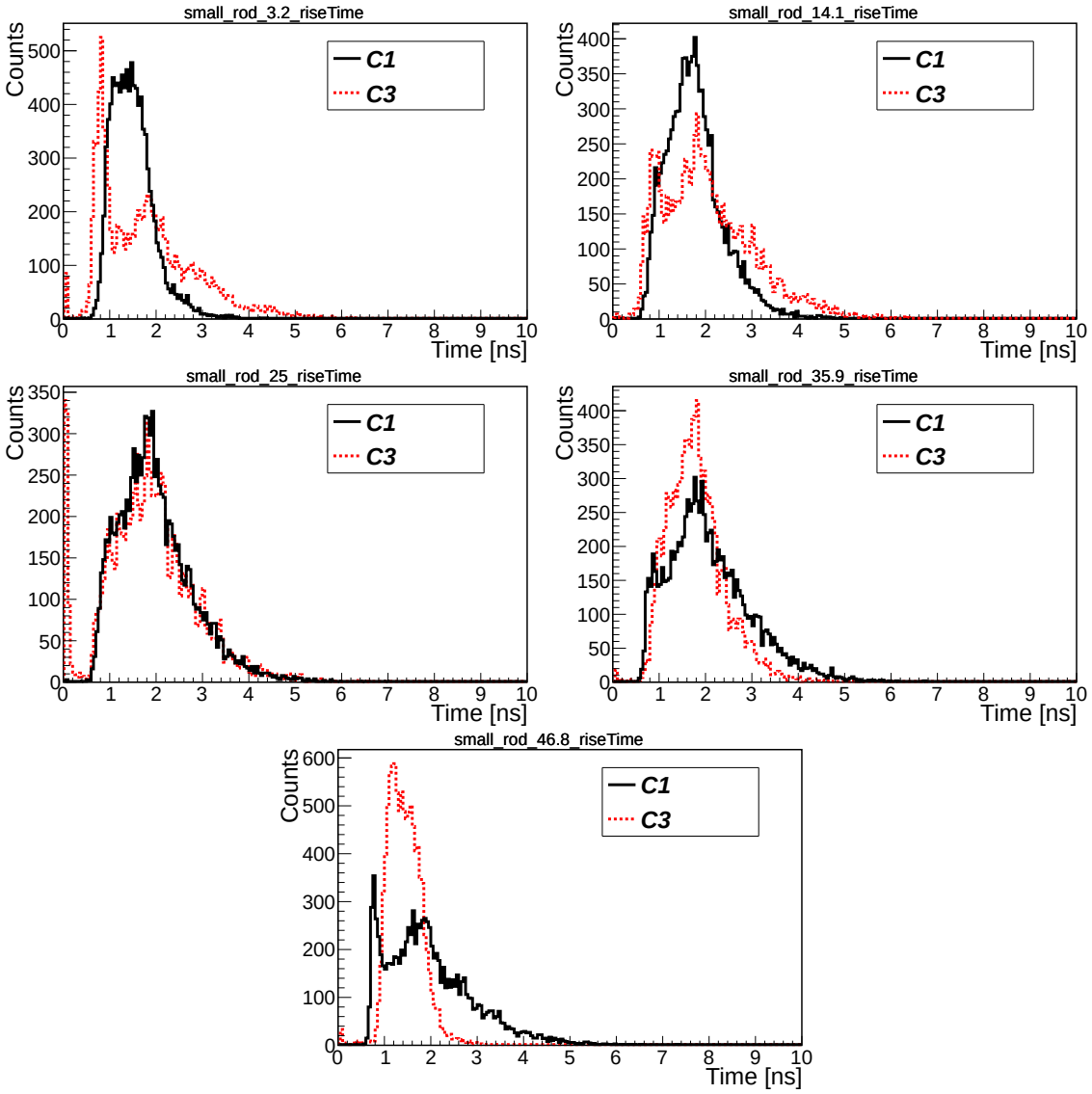

Figure B.3: Histograms of rise time for small rod shape of scintillator for position 3.2 cm, 14.1 cm, 25 cm, 35.9 cm and 46.8 cm.

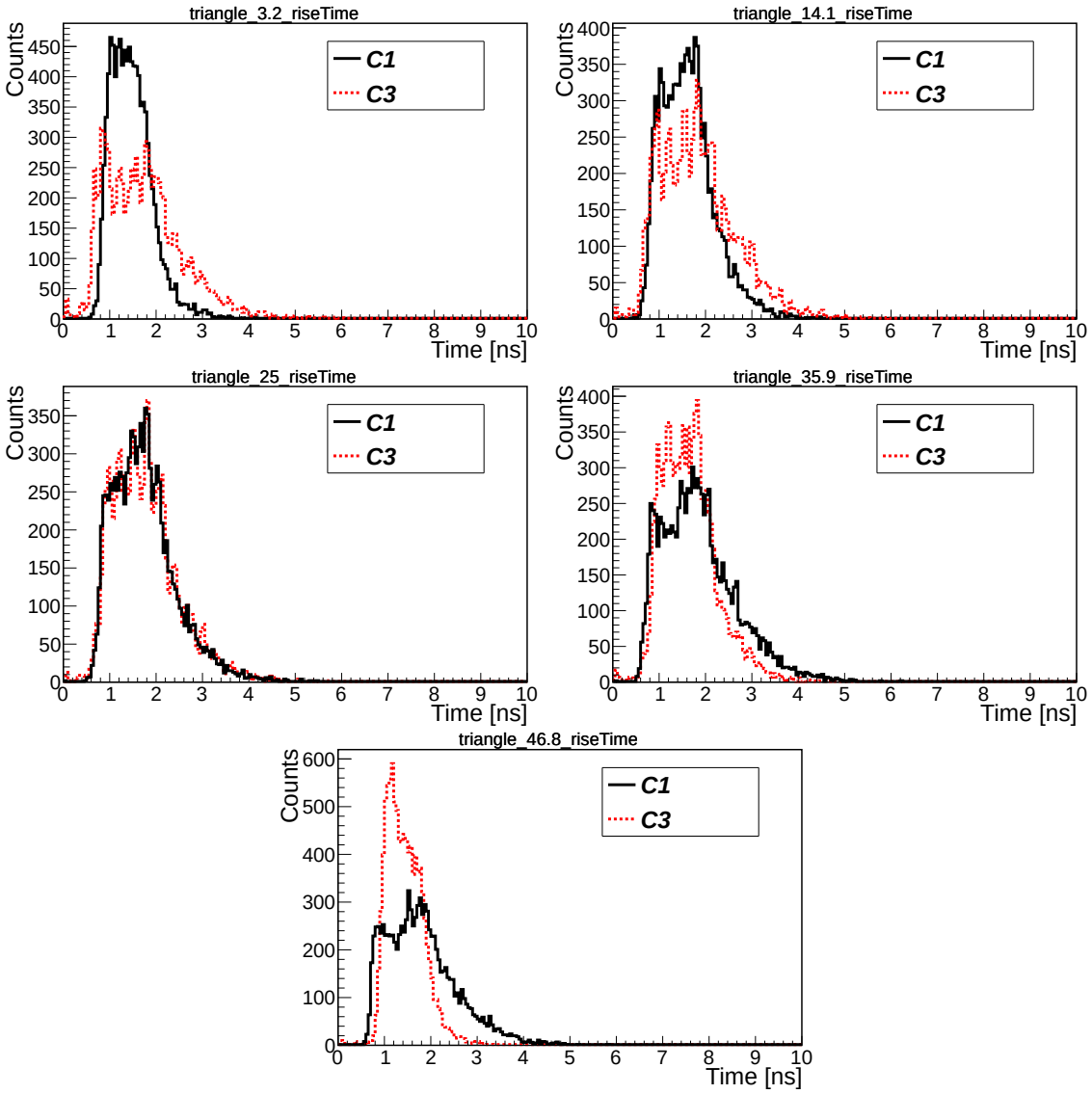

Figure B.4: Histograms of rise time for triangle shape of scintillator for position 3.2 cm, 14.1 cm, 25 cm, 35.9 cm and 46.8 cm.

Estimation of mean rise times versus distance from given photomultiplier

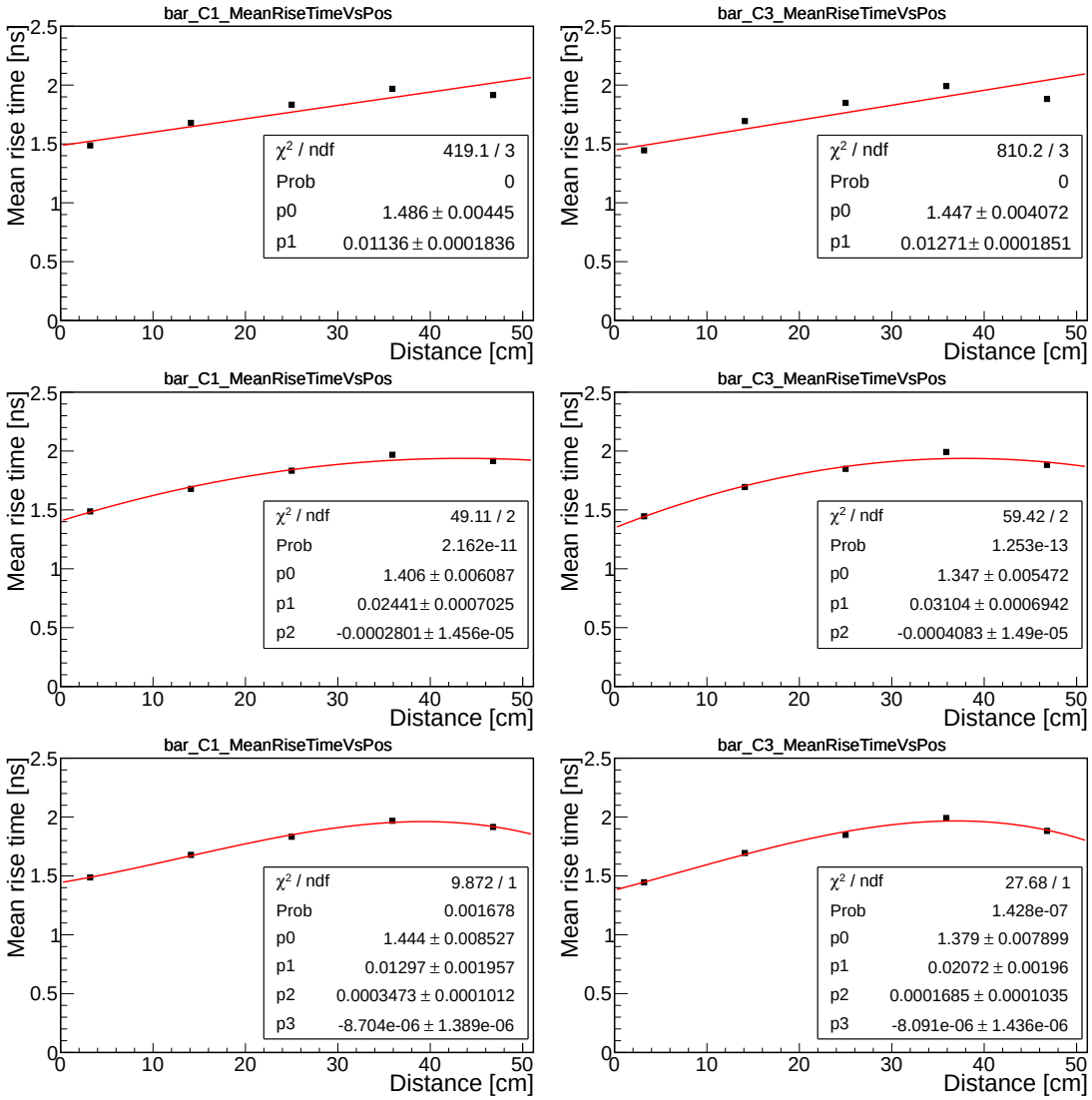

Figure B.5: Plots of mean rise time versus distance for bar shape of scintillator for photomultiplier PM1 (C1) and F2 (C3) with 3 different functions fitted to data points: - linear (top pair), quadratic polynomial (central pair) and cubic polynomial (bottom pair).

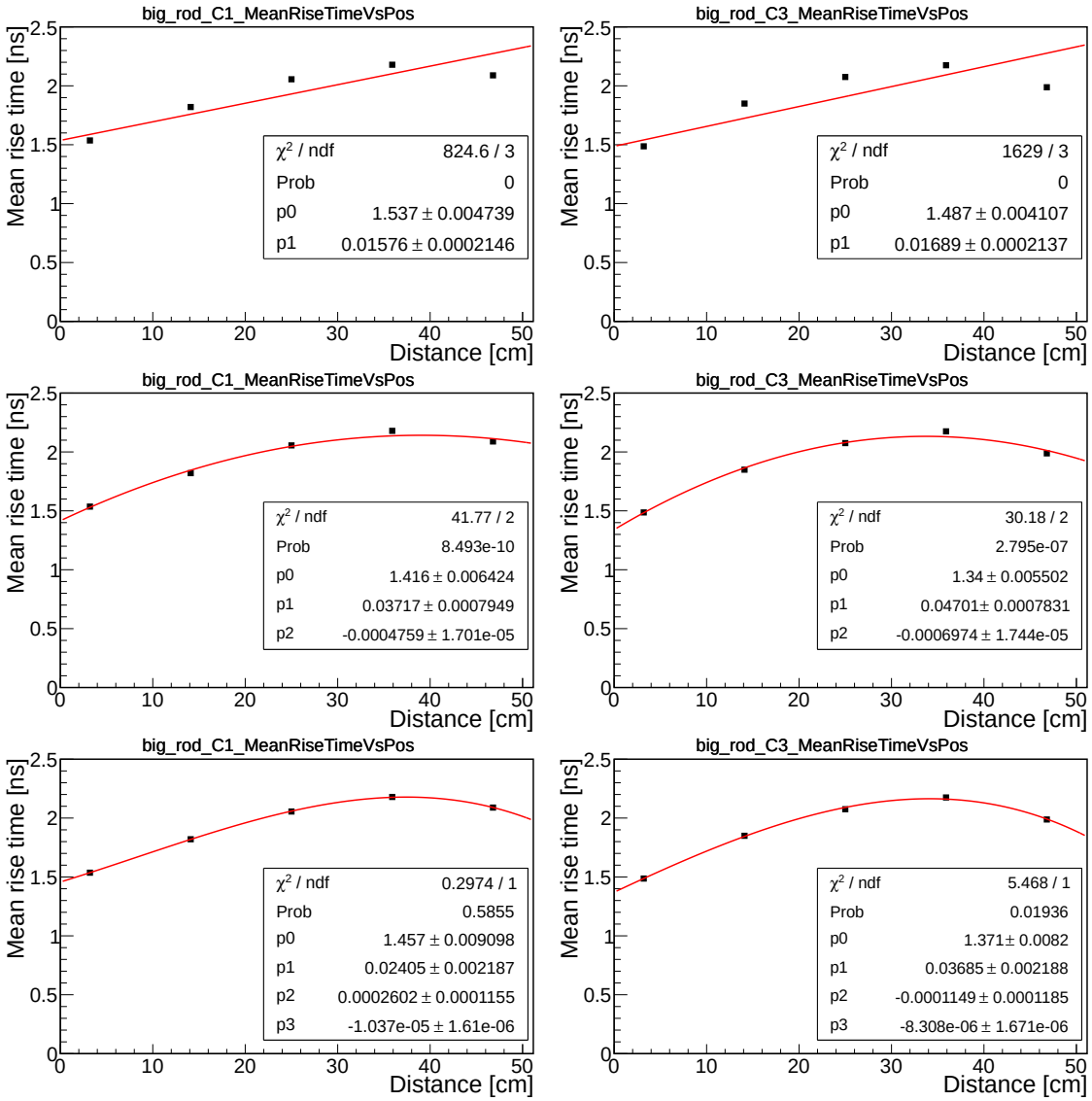

Figure B.6: Plots of mean rise time versus distance for big rod shape of scintillator for photomultiplier PM1 (C1) and F2 (C3) with 3 different functions fitted to data points: - linear (top pair), quadratic polynomial (central pair) and cubic polynomial (bottom pair).

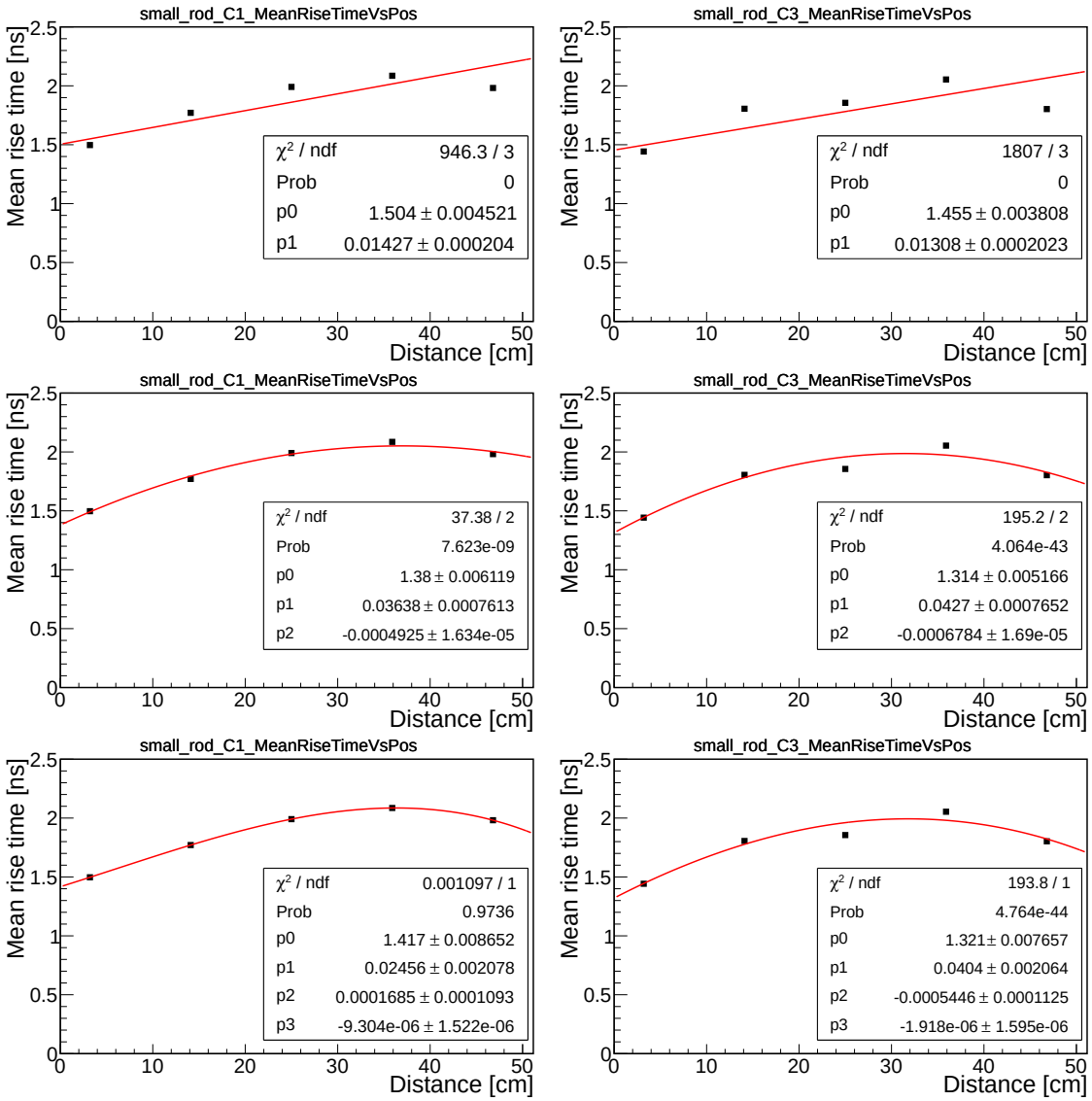

Figure B.7: Plots of mean rise time versus distance for small rod shape of scintillator for photomultiplier PM1 (C1) and F2 (C3) with 3 different functions fitted to data points: - linear (top pair), quadratic polynomial (central pair) and cubic polynomial (bottom pair).

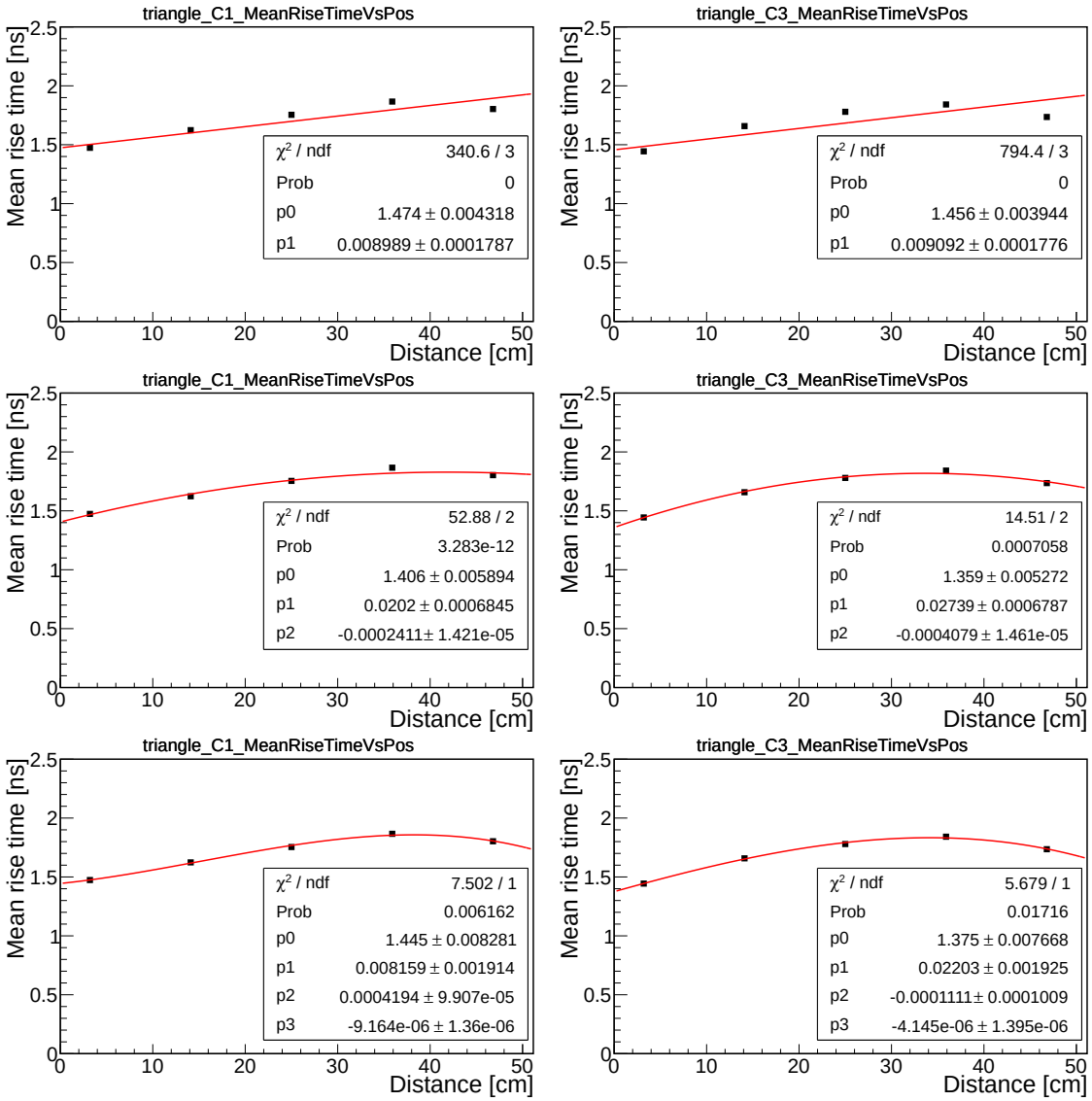

Figure B.8: Plots of mean rise time versus distance for triangle shape of scintillator for photomultiplier PM1 (C1) and F2 (C3) with 3 different functions fitted to data points: linear (top pair), quadratic polynomial (central pair) and cubic polynomial (bottom pair).

Estimation of rise times after cuts

Position	Photomultiplier	Value of cut [pC]	Photomultiplier	Value of cut [pC]
3.2 cm	PM1	62	F2	15
14.1 cm	PM1	37	F2	19
25 cm	PM1	26	F2	26
35.9 cm	PM1	19	F2	37
46.8 cm	PM1	15	F2	62

Table B.11: Value of cuts done of area histograms for bar shape of scintillator.

Position	Photomultiplier	Value of cut [pC]	Photomultiplier	Value of cut [pC]
3.2 cm	PM1	68	F2	13
14.1 cm	PM1	38	F2	18
25 cm	PM1	24	F2	24
35.9 cm	PM1	18	F2	38
46.8 cm	PM1	13	F2	68

Table B.12: Value of cuts done of area histograms for big rod shape of scintillator.

Position	Photomultiplier	Value of cut [pC]	Photomultiplier	Value of cut [pC]
3.2 cm	PM1	67	F2	10
14.1 cm	PM1	34	F2	16
25 cm	PM1	21	F2	21
35.9 cm	PM1	16	F2	34
46.8 cm	PM1	10	F2	67

Table B.13: Value of cuts done of area histograms for small rod shape of scintillator.

Position	Photomultiplier	Value of cut [pC]	Photomultiplier	Value of cut [pC]
3.2 cm	PM1	62	F2	13
14.1 cm	PM1	31	F2	15
25 cm	PM1	22	F2	22
35.9 cm	PM1	15	F2	31
46.8 cm	PM1	13	F2	62

Table B.14: Value of cuts done of area histograms for triangle shape of scintillator.

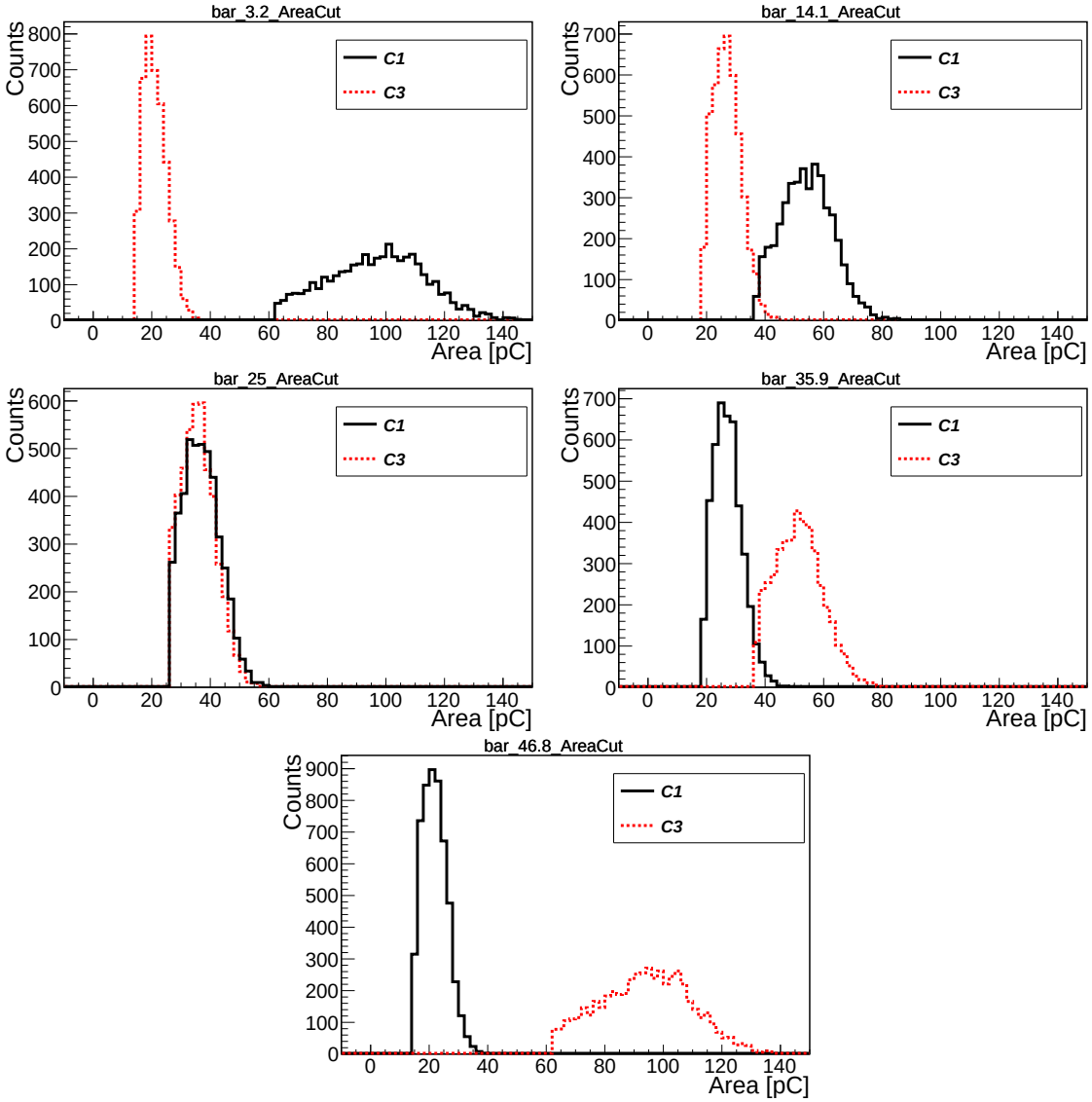

Figure B.9: Histograms of area after cuts for bar scintillator shape for photomultiplier PM1 (C1) and F2 (C3) for all five positions.

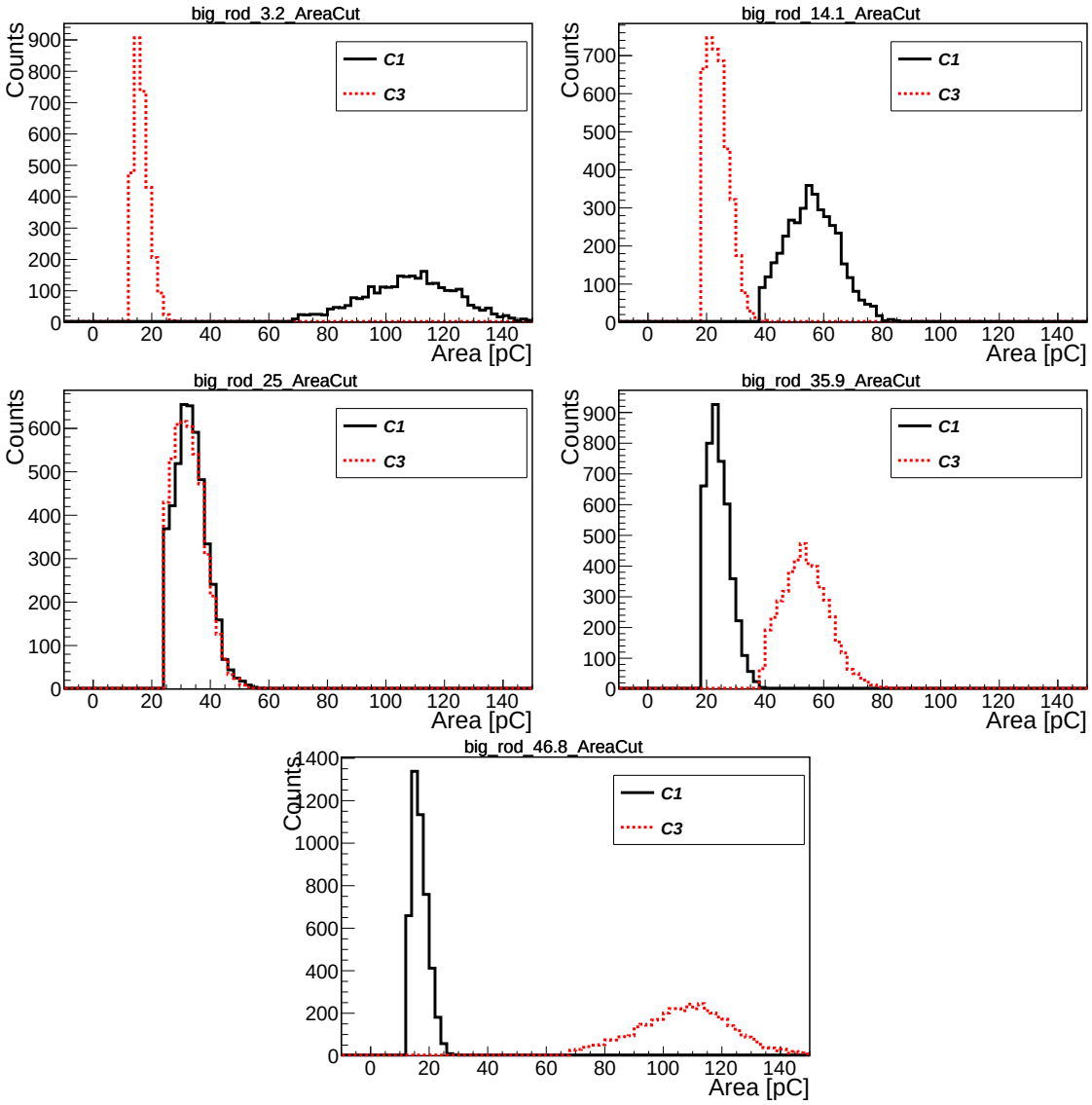

Figure B.10: Histograms of area after cuts for big rod scintillator shape for photomultiplier PM1 (C1) and F2 (C3) for positions 3.2 cm (left top corner), 25 cm (right top corner) and 46.8 cm (bottom).

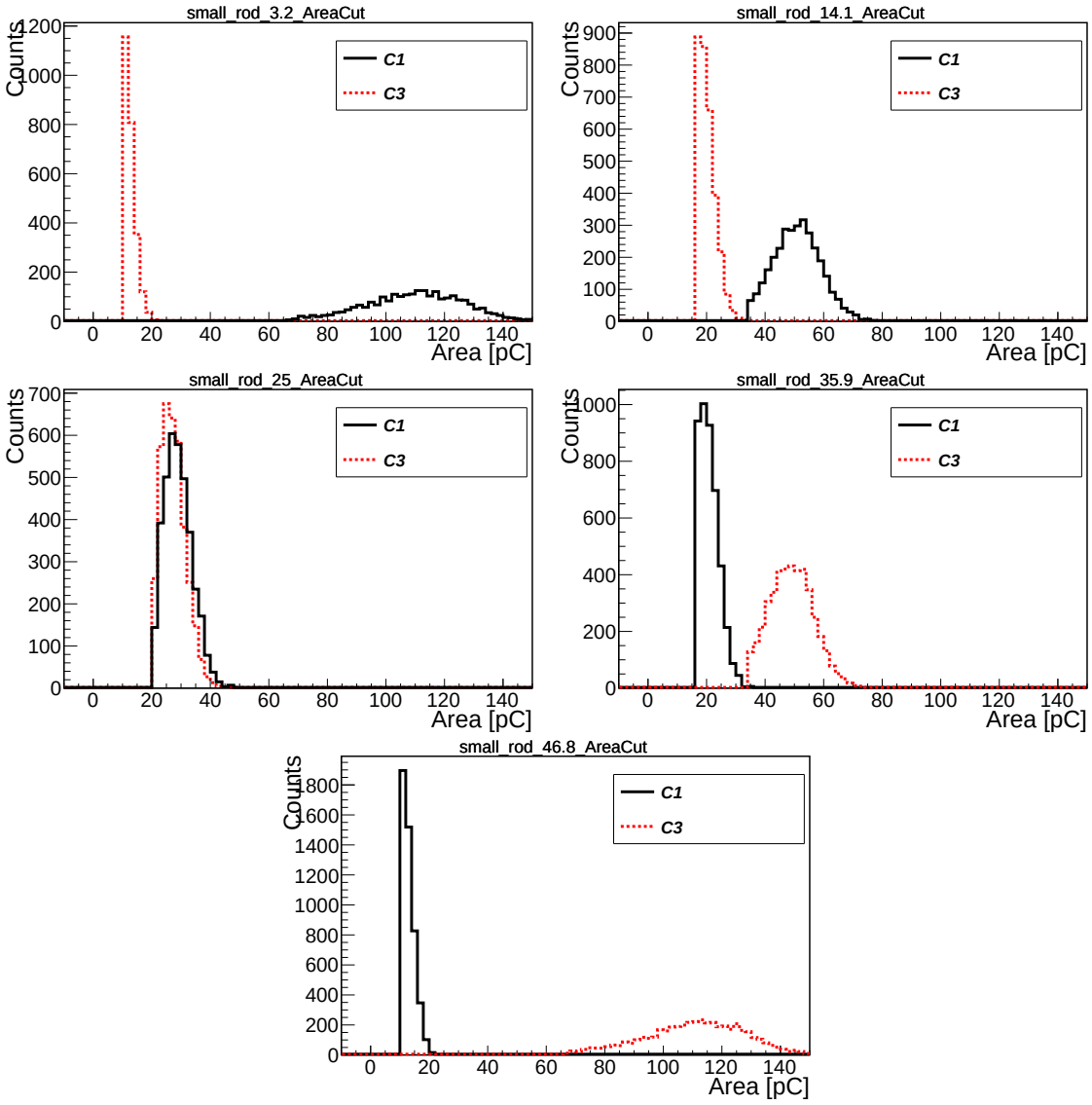

Figure B.11: Histograms of area after cuts for small rod scintillator shape for photomultiplier PM1 (C1) and F2 (C3) for all five positions.

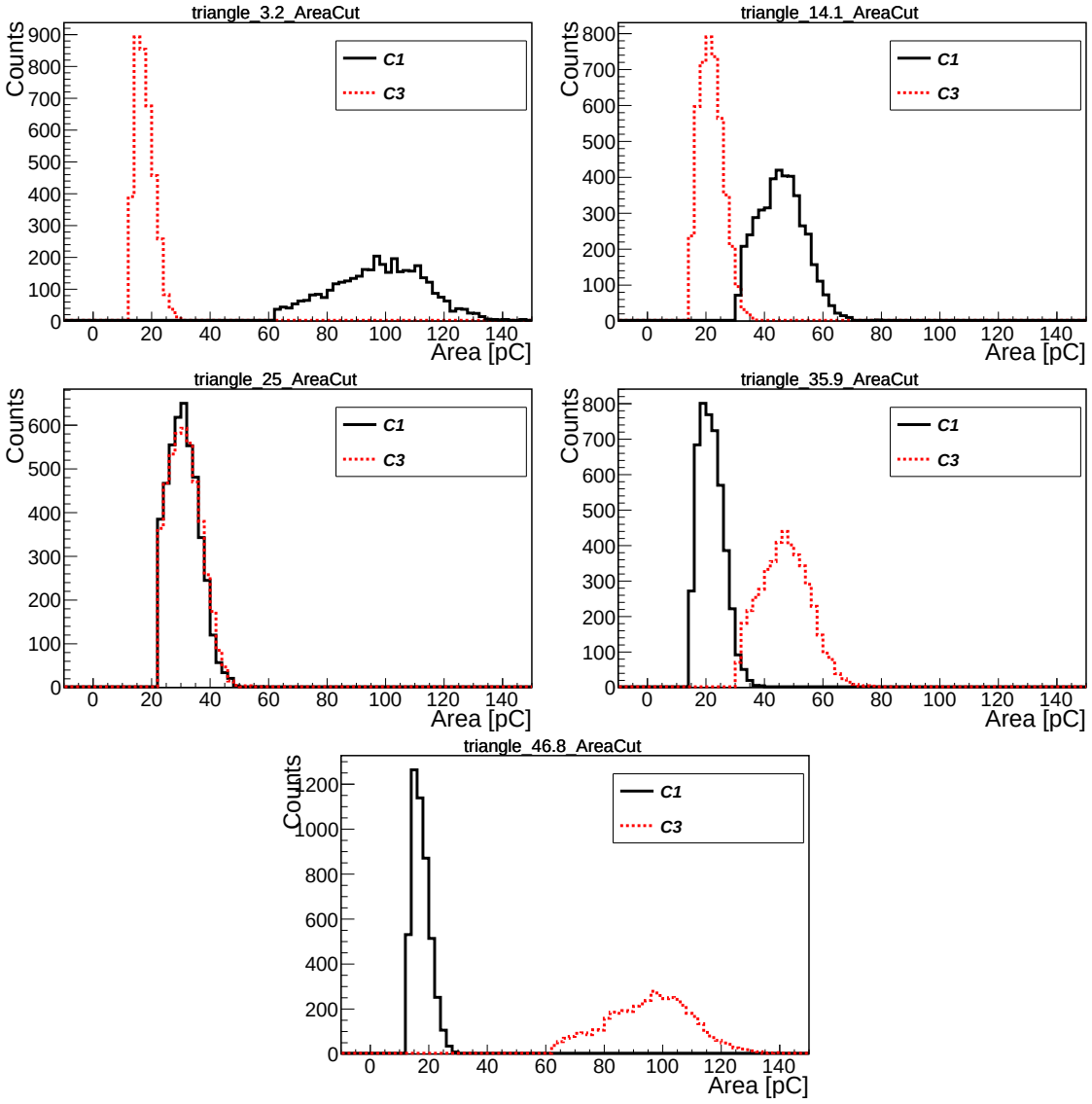

Figure B.12: Histograms of area after cuts for triangle scintillator shape for photomultiplier PM1 (C1) and F2 (C3) for all five positions.

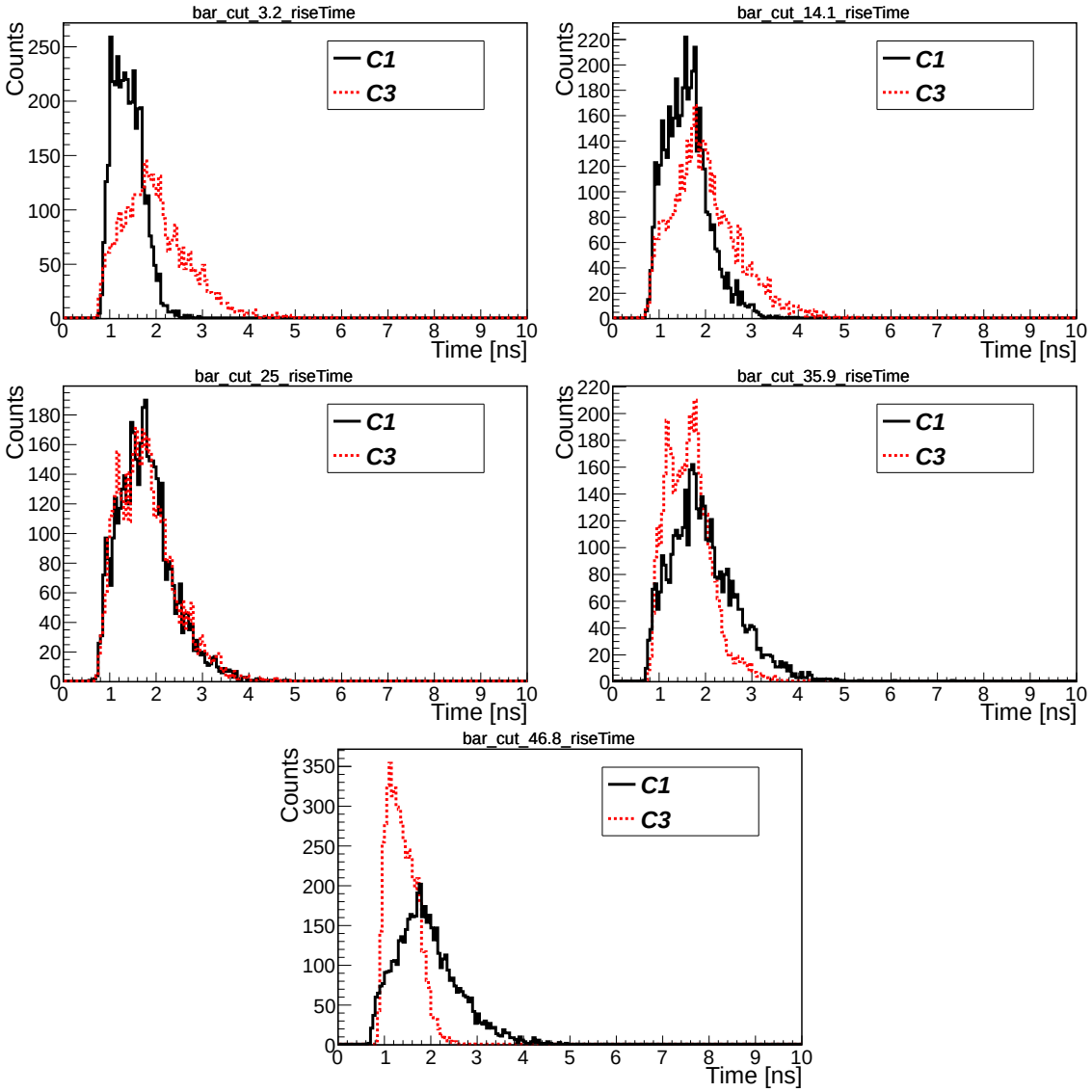

Figure B.13: Histograms of rise time after cuts for bar shape scintillator for all five positions.

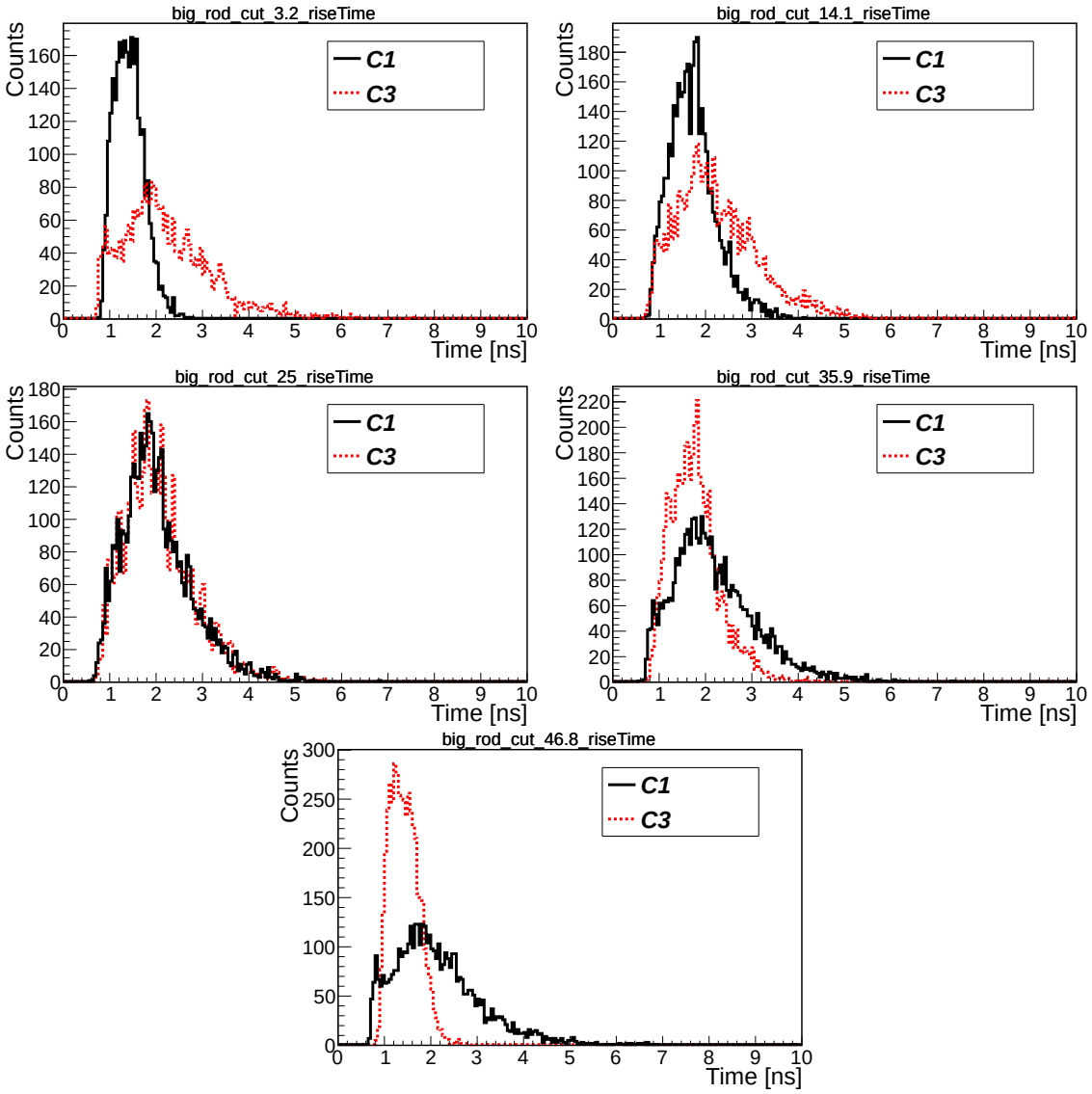

Figure B.14: Histograms of rise time after cuts for big rod shape scintillator for all five positions.

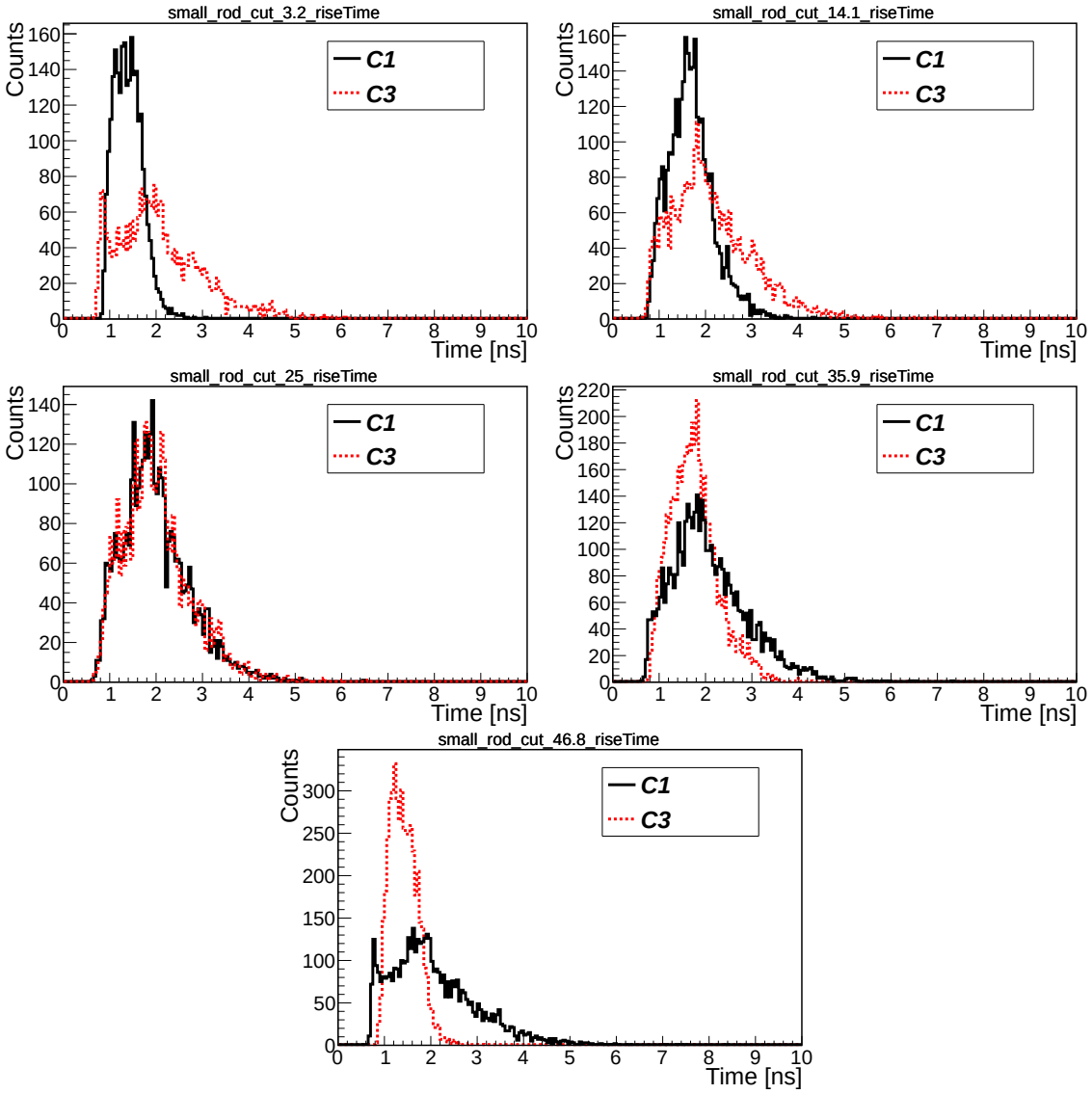

Figure B.15: Histograms of rise time after cuts for small rod shape scintillator for all five positions.

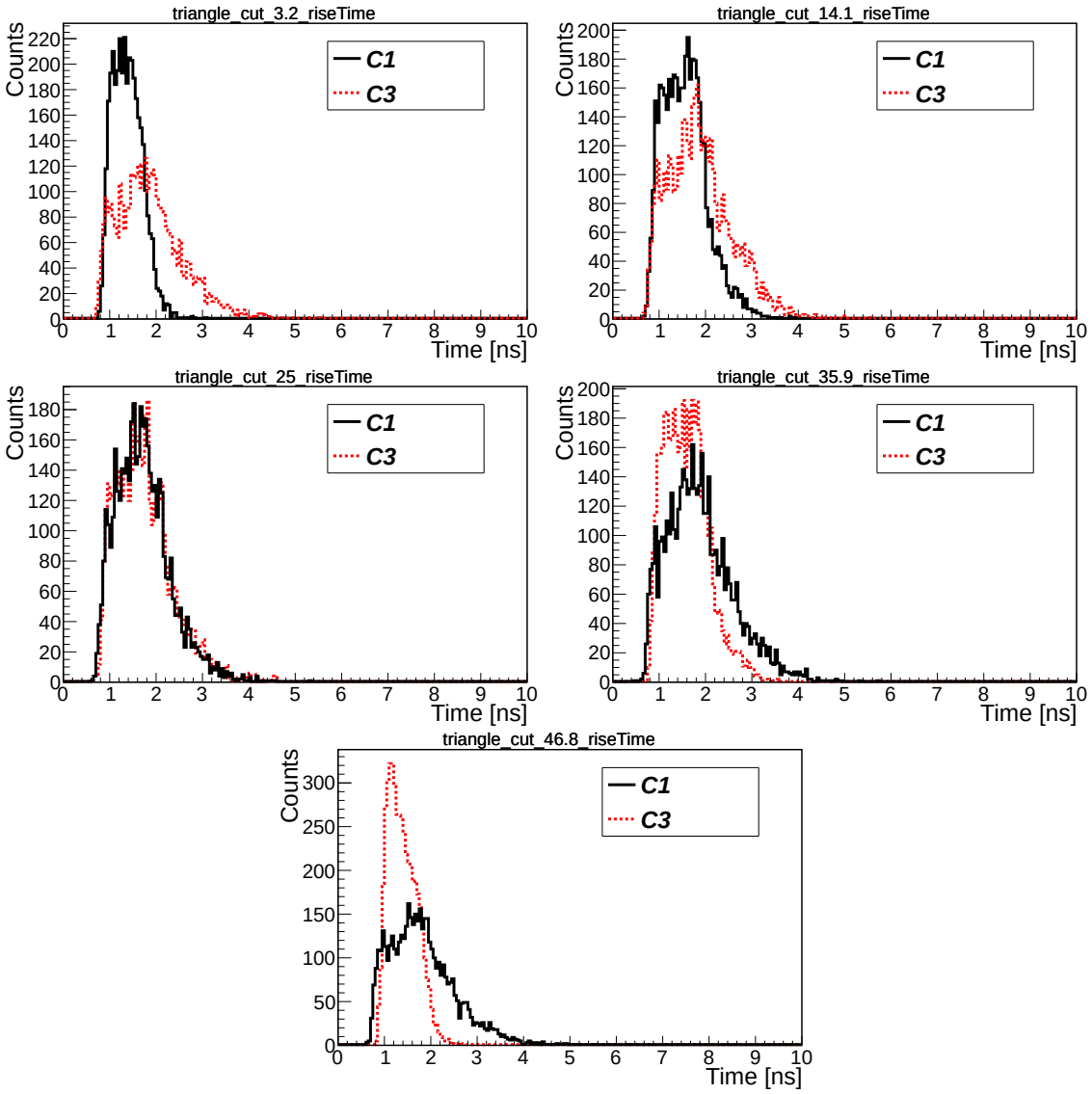

Figure B.16: Histograms of rise time after cuts for triangle shape scintillator for all five positions.

Estimation of mean rise times versus distance from given photomultiplier after cuts

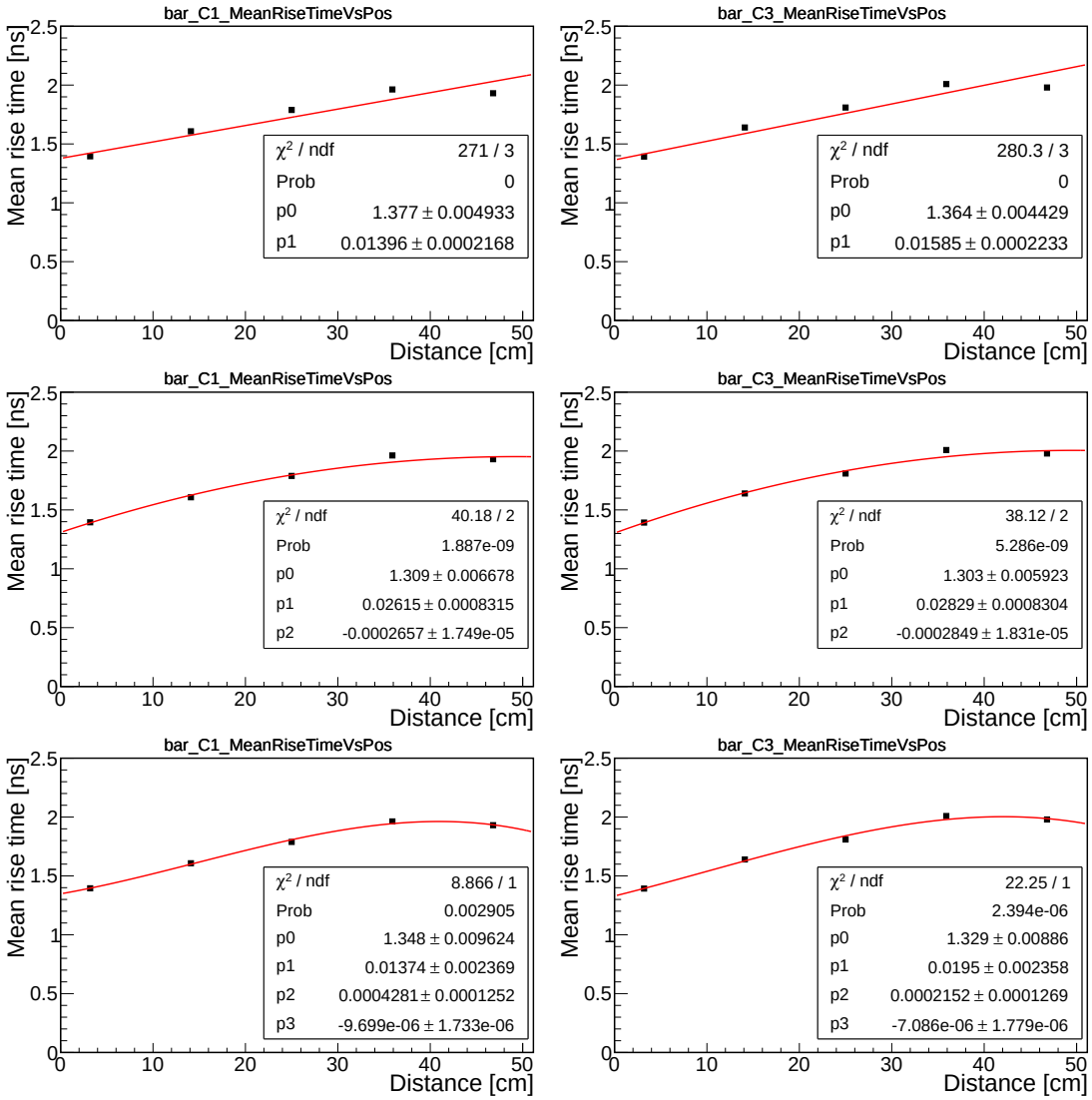

Figure B.17: Plots of mean rise time versus distance after cuts for bar scintillator shape for photomultiplier PM1 (C1) and F2 (C3) with 3 different functions fitted to data points: linear (top pair), quadratic polynomial (central pair) and cubic polynomial (bottom pair).

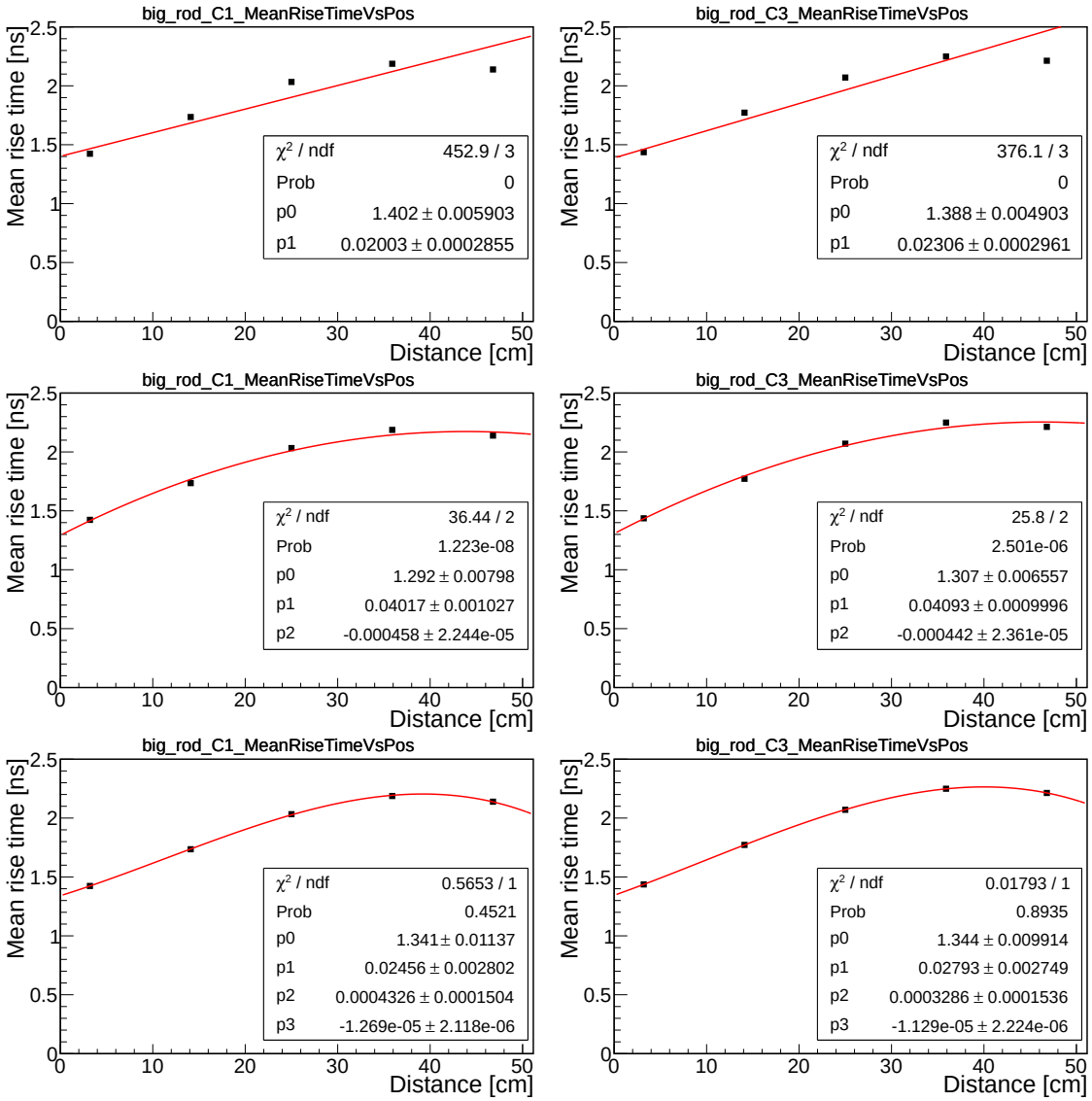

Figure B.18: Plots of mean rise time versus distance after cuts for big rod scintillator shape for photomultiplier PM1 (C1) and F2 (C3) with 3 different functions fitted to data points: linear (top pair), quadratic polynomial (central pair) and cubic polynomial (bottom pair).

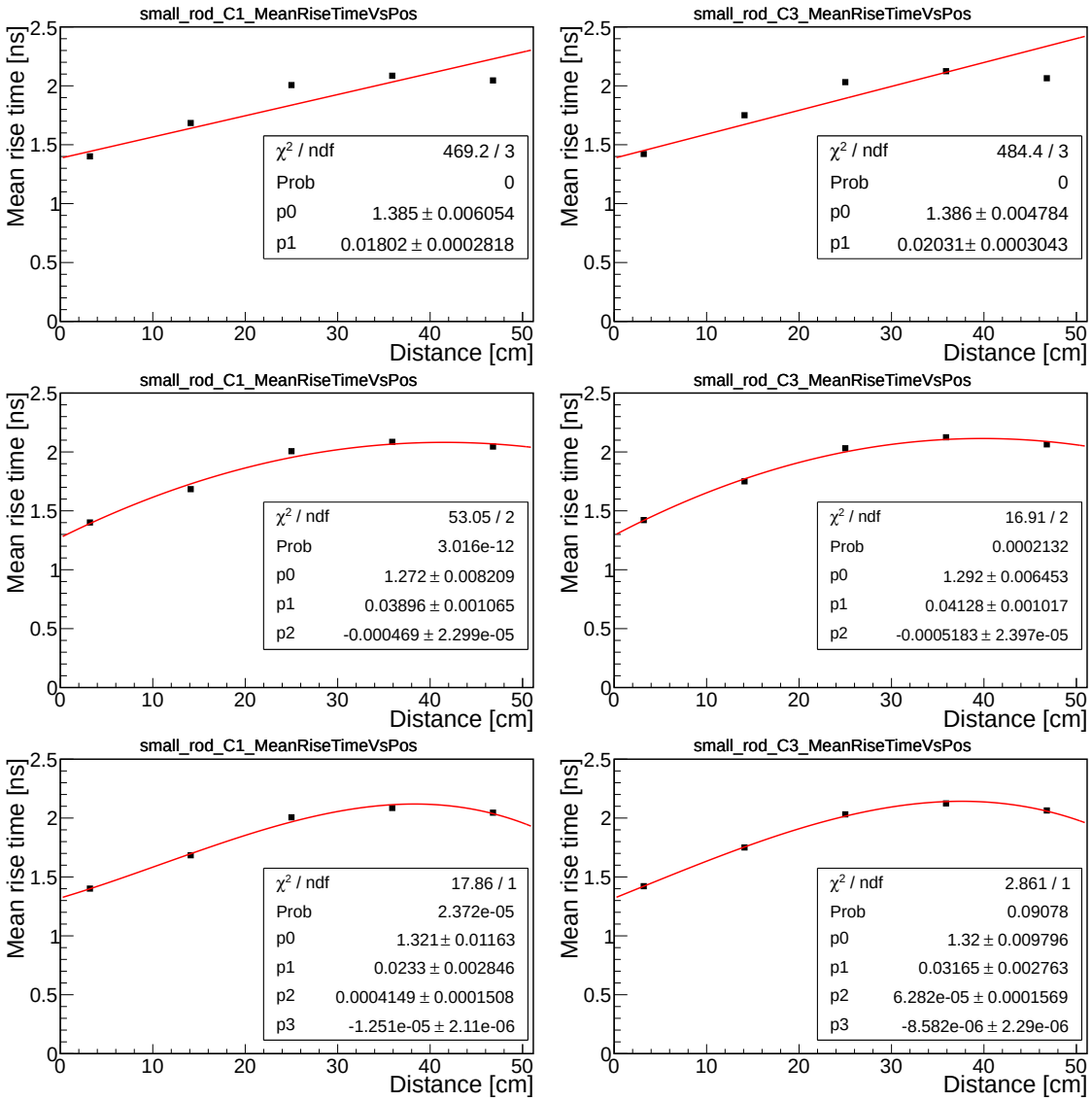

Figure B.19: Plots of mean rise time versus distance after cuts for small rod scintillator shape for photomultiplier PM1 (C1) and F2 (C3) with 3 different functions fitted to data points: linear (top pair), quadratic polynomial (central pair) and cubic polynomial (bottom pair).

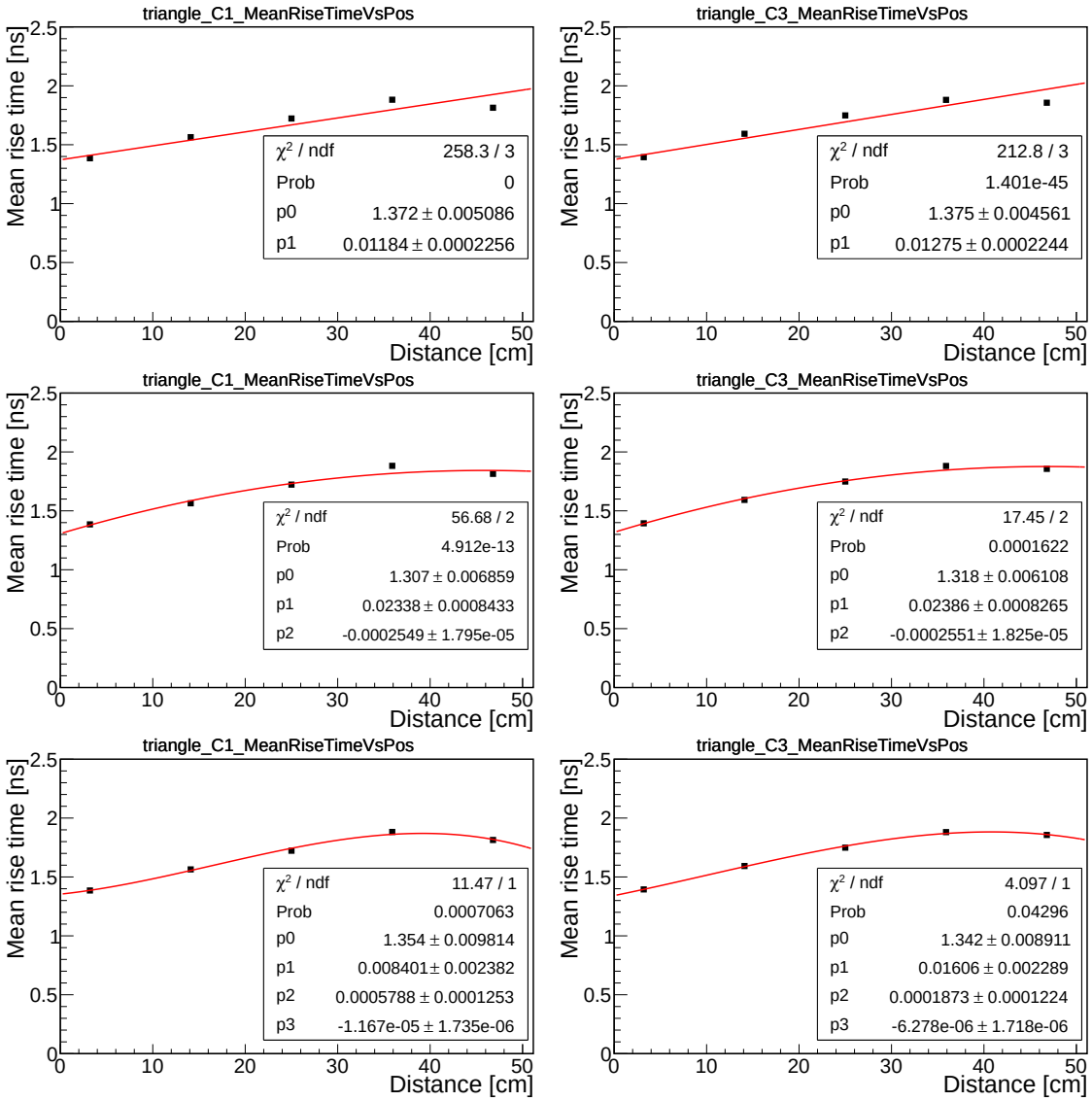

Figure B.20: Plots of mean rise time versus distance after cuts for triangle scintillator shape for photomultiplier PM1 (C1) and F2 (C3) with 3 different functions fitted to data points: linear (top pair), quadratic polynomial (central pair) and cubic polynomial (bottom pair).

Appendix C - fall time spectra

Fall time spectra for different scintillator shapes

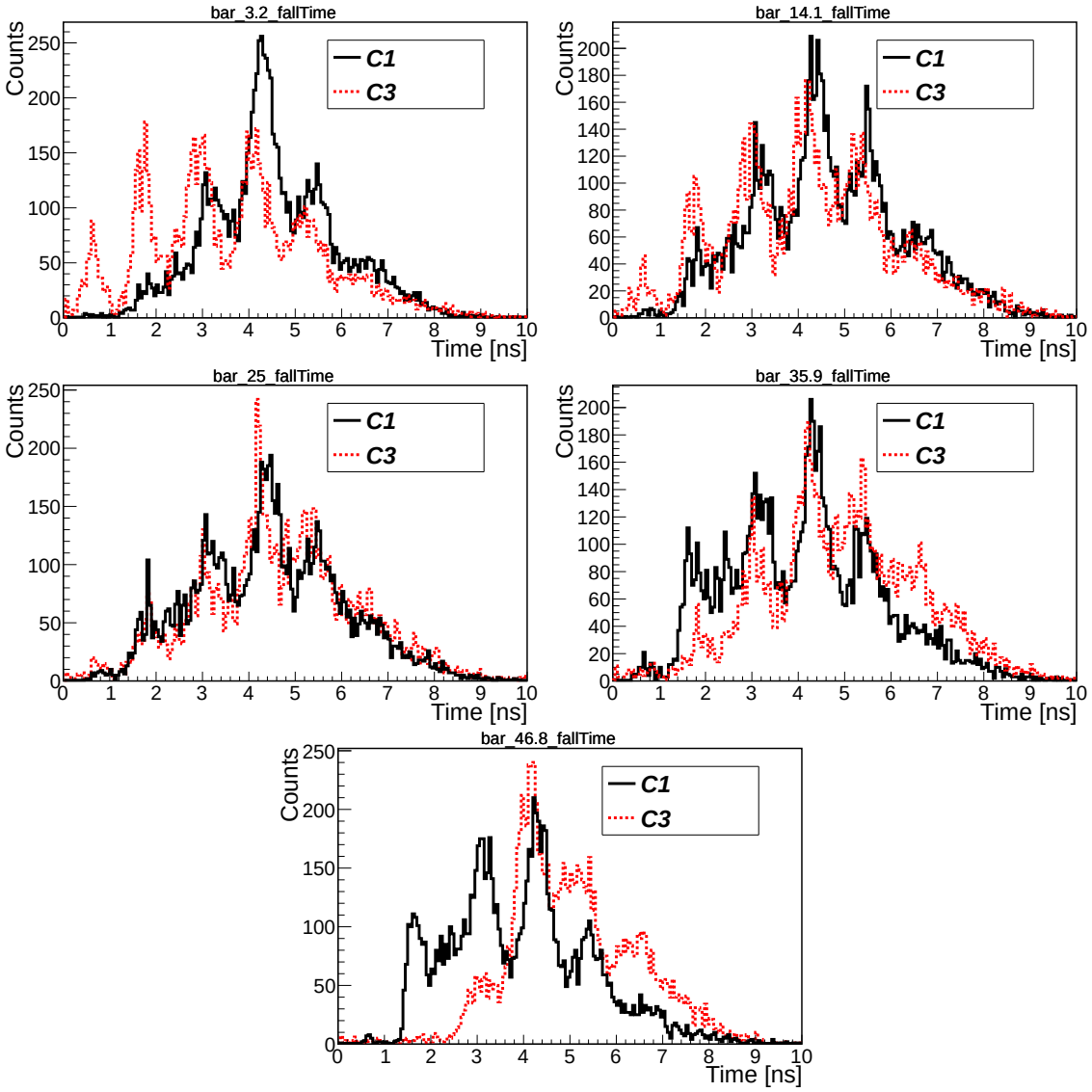

Figure C.1: Histograms of fall time for bar shape scintillator for position 3.2 cm, 14.1 cm, 25 cm, 35.9 cm and 46.8 cm.

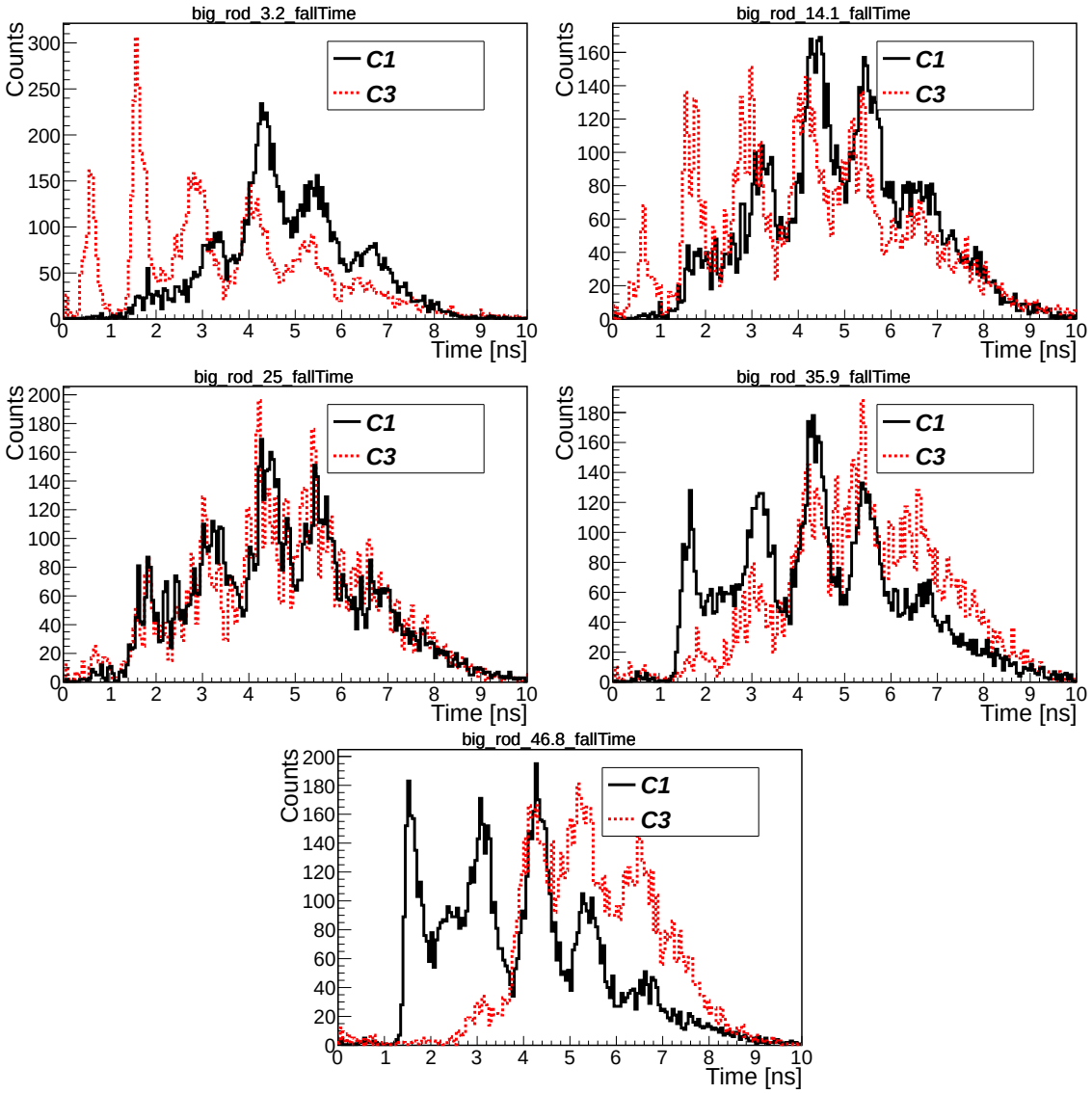

Figure C.2: Histograms of fall time for big rod shape scintillator for position 3.2 cm, 14.1 cm, 25 cm, 35.9 cm and 46.8 cm.

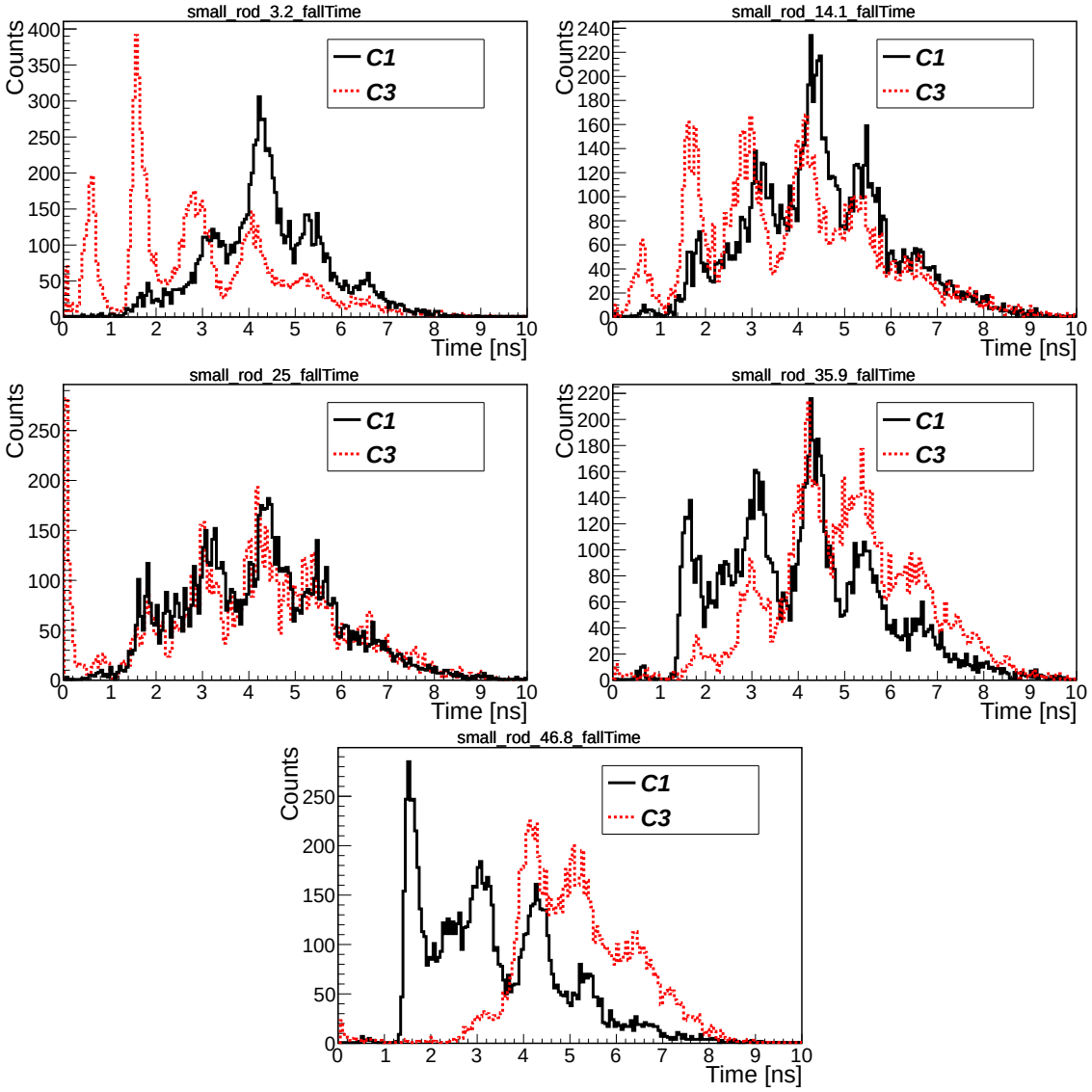

Figure C.3: Histograms of fall time for small rod shape scintillator for position 3.2 cm, 14.1 cm, 25 cm, 35.9 cm and 46.8 cm.

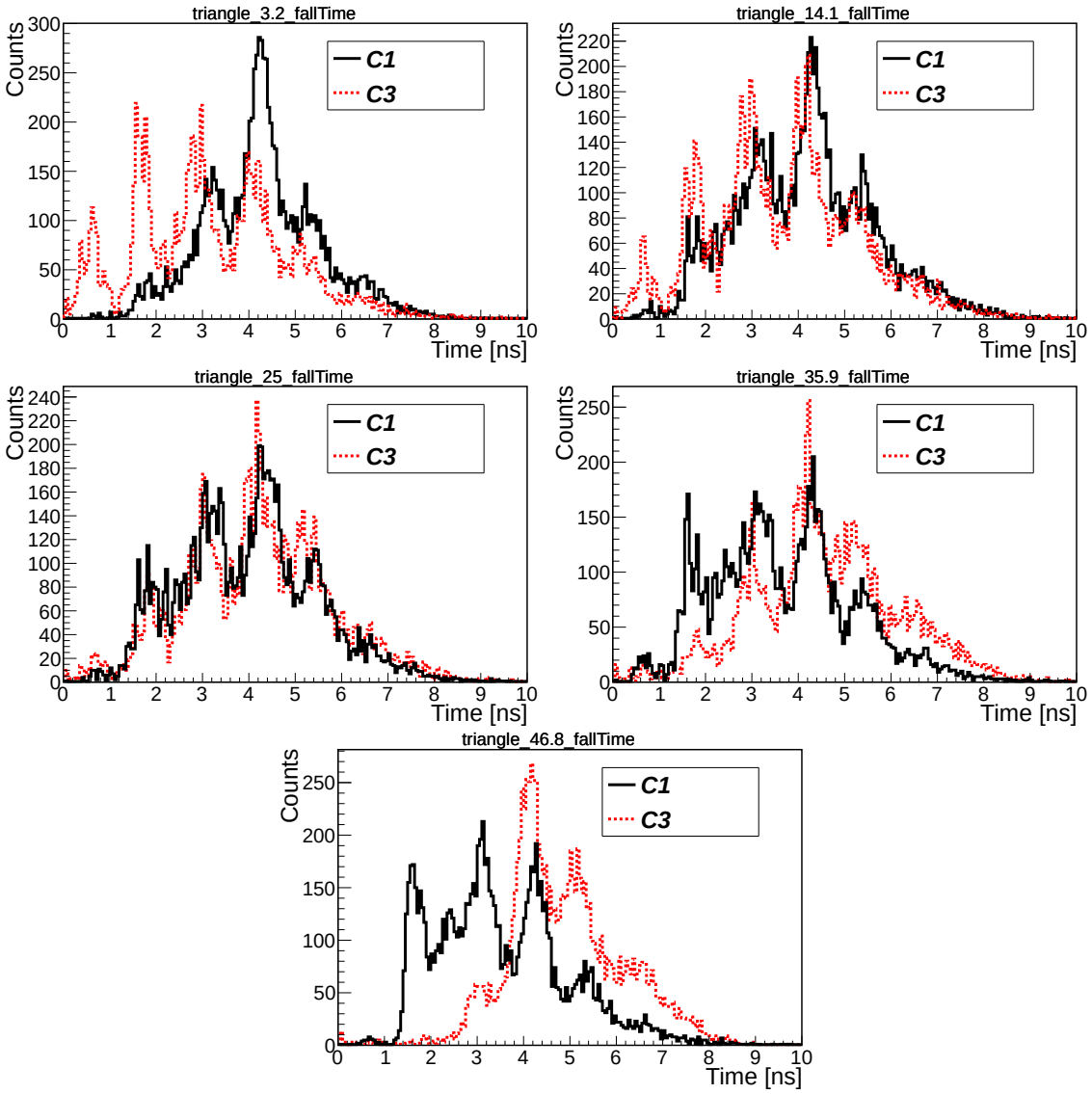

Figure C.4: Histograms of fall time for triangle shape scintillator for position 3.2 cm, 14.1 cm, 25 cm, 35.9 cm and 46.8 cm.

Estimation of mean fall times versus distance from given photomultiplier

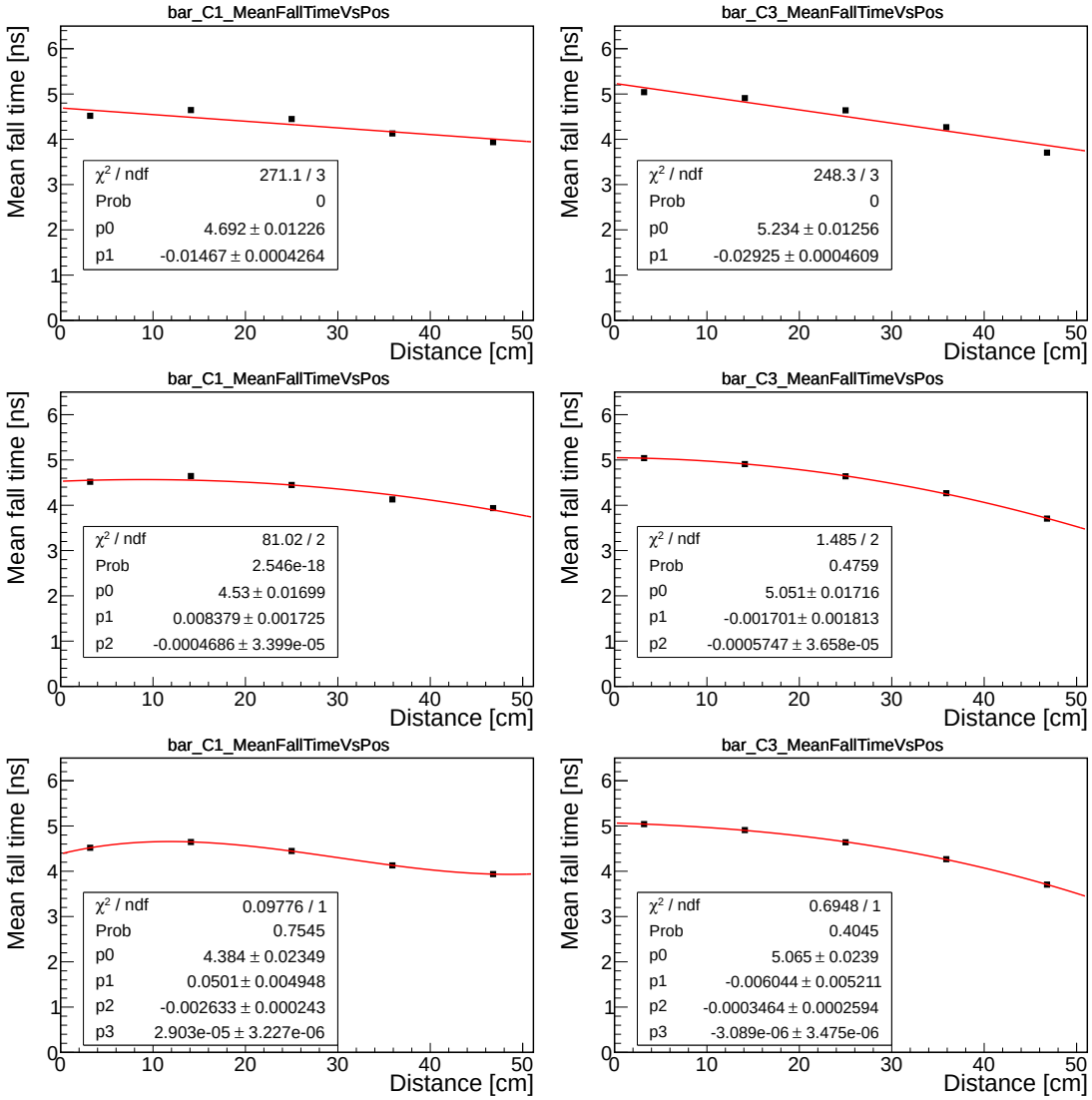

Figure C.5: Plots of mean fall time versus distance for bar shape of scintillator for photomultiplier PM1 (C1) and F2 (C3) with 3 different functions fitted to data points: linear (top pair), quadratic polynomial (central pair) and cubic polynomial (bottom pair).

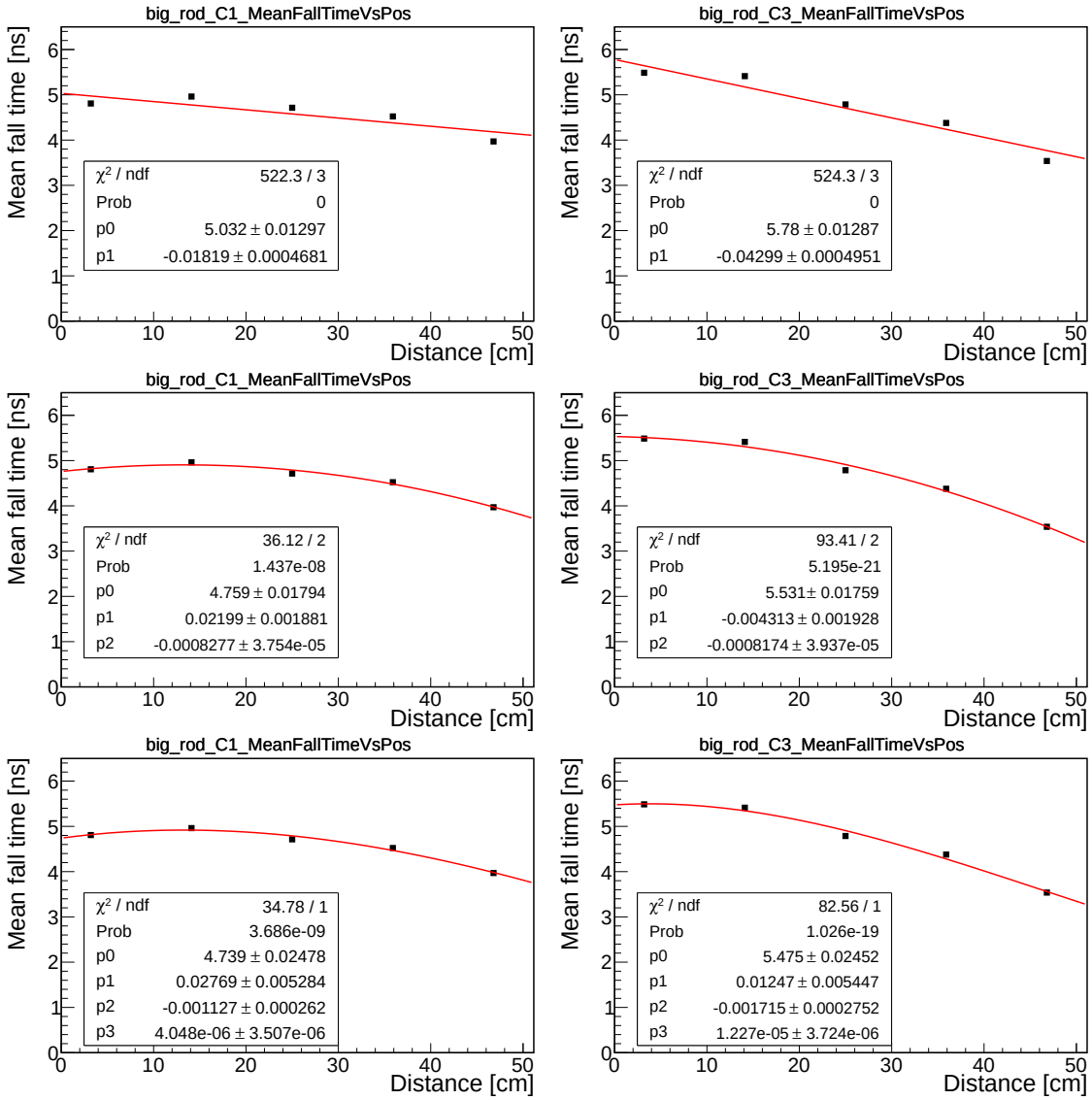

Figure C.6: Plots of mean fall time versus distance for big rod shape of scintillator for photomultiplier PM1 (C1) and F2 (C3) with 3 different functions fitted to data points: linear (top pair), quadratic polynomial (central pair) and cubic polynomial (bottom pair).

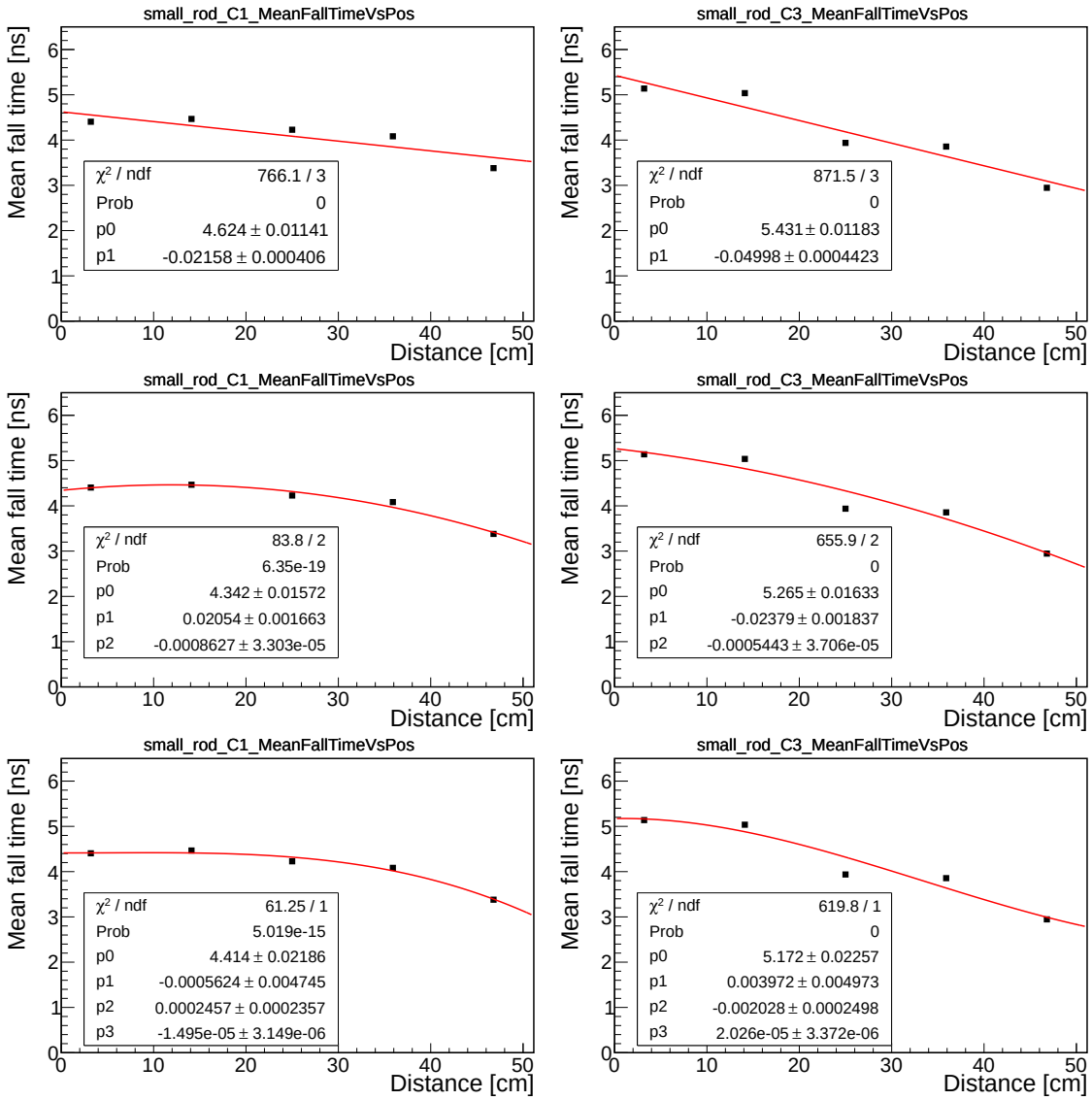

Figure C.7: Plots of mean fall time versus distance for small rod shape of scintillator for photomultiplier PM1 (C1) and F2 (C3) with 3 different functions fitted to data points: linear (top pair), quadratic polynomial (central pair) and cubic polynomial (bottom pair).

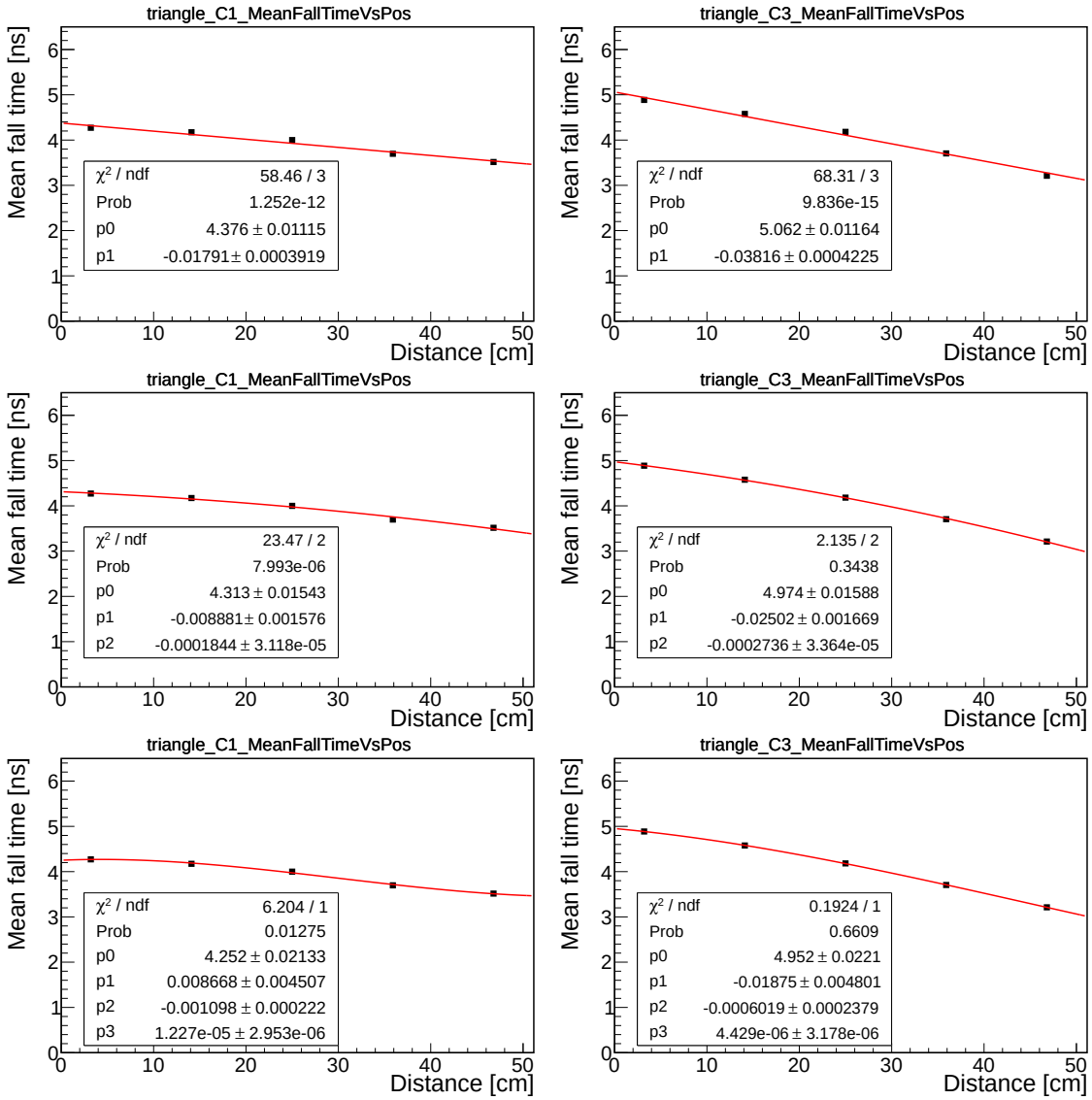

Figure C.8: Plots of mean fall time versus distance for triangle shape of scintillator for photomultiplier PM1 (C1) and F2 (C3) with 3 different functions fitted to data points: linear (top pair), quadratic polynomial (central pair) and cubic polynomial (bottom pair).

Estimation of fall times after cuts

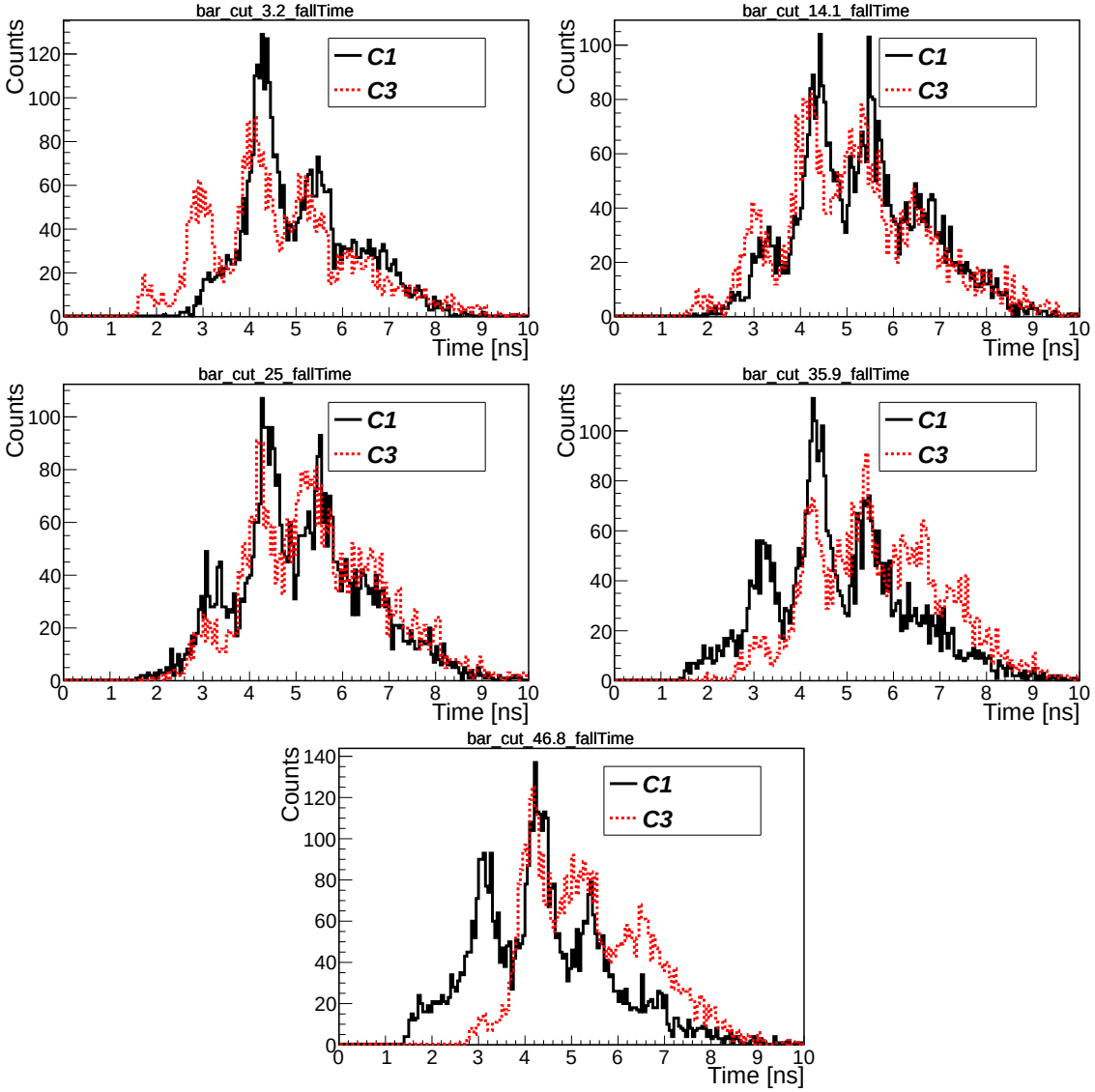

Figure C.9: Histograms of fall time after cuts for bar shape scintillator for position 3.2 cm, 14.1 cm, 25 cm, 35.9 cm and 46.8 cm.

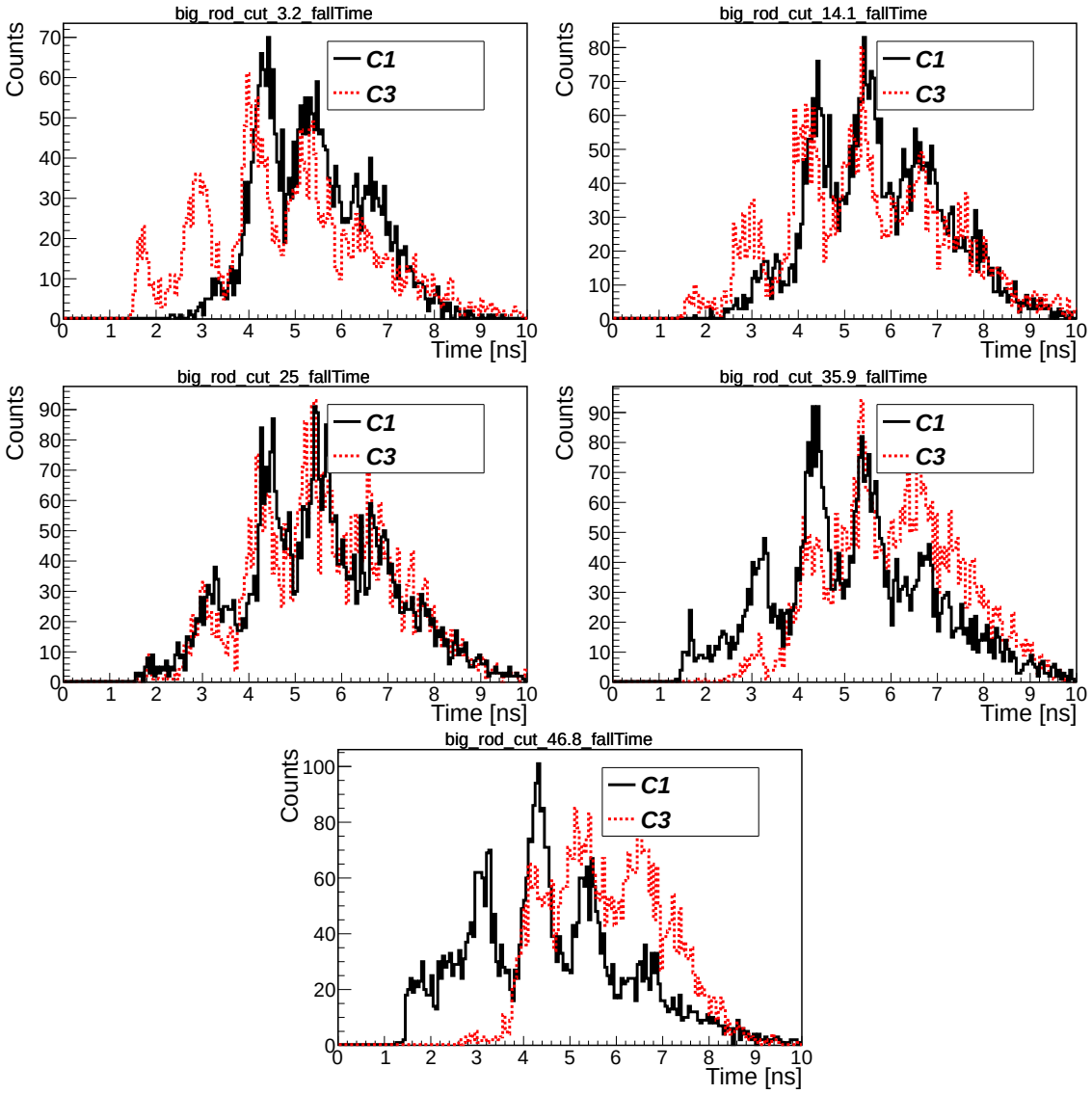

Figure C.10: Histograms of fall time after cuts for big rod shape scintillator for position 3.2 cm, 14.1 cm, 25 cm, 35.9 cm and 46.8 cm.

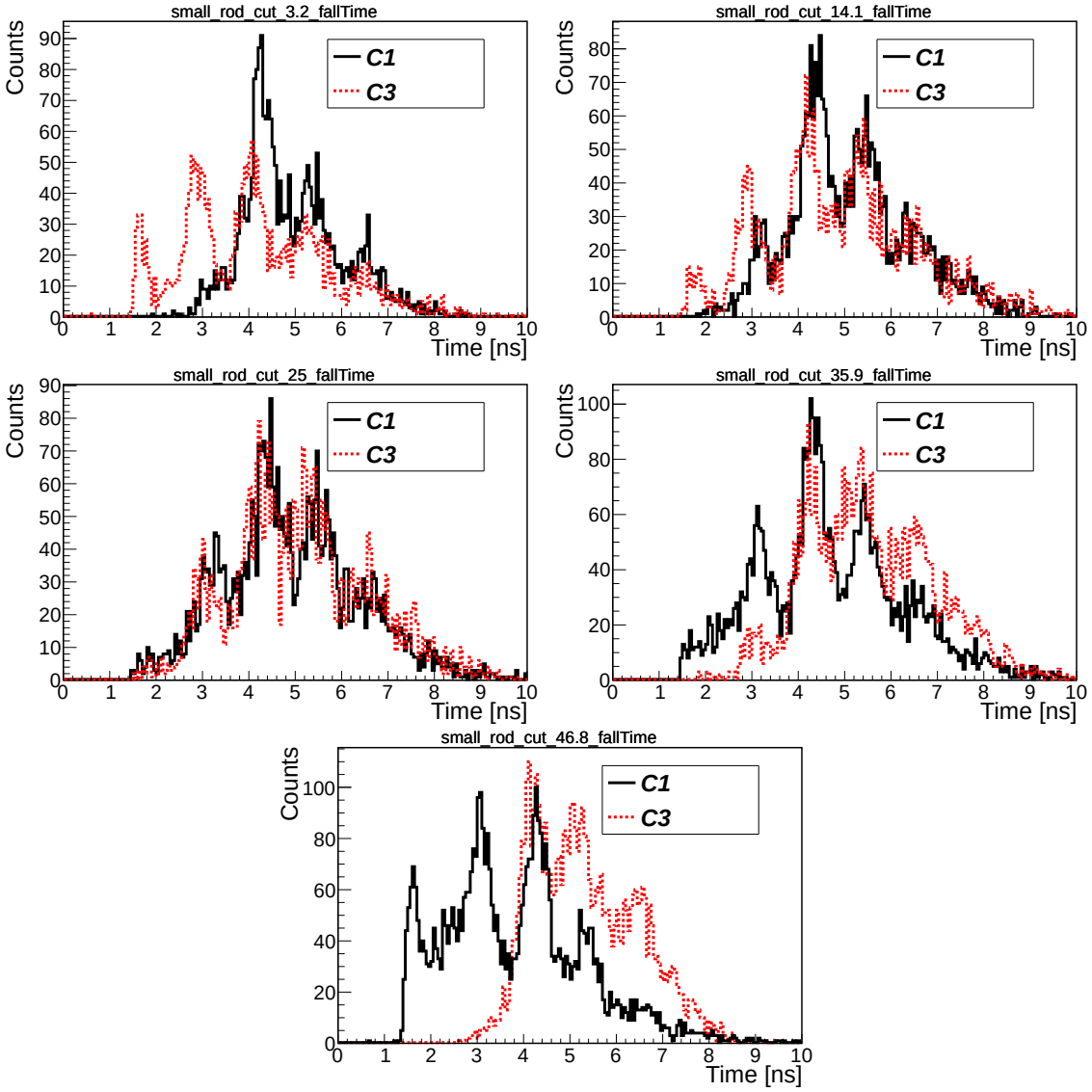

Figure C.11: Histograms of fall time after cuts for small rod shape scintillator for position 3.2 cm, 14.1 cm, 25 cm, 35.9 cm and 46.8 cm.

Estimation of mean fall times versus distance from given photomultiplier after cuts

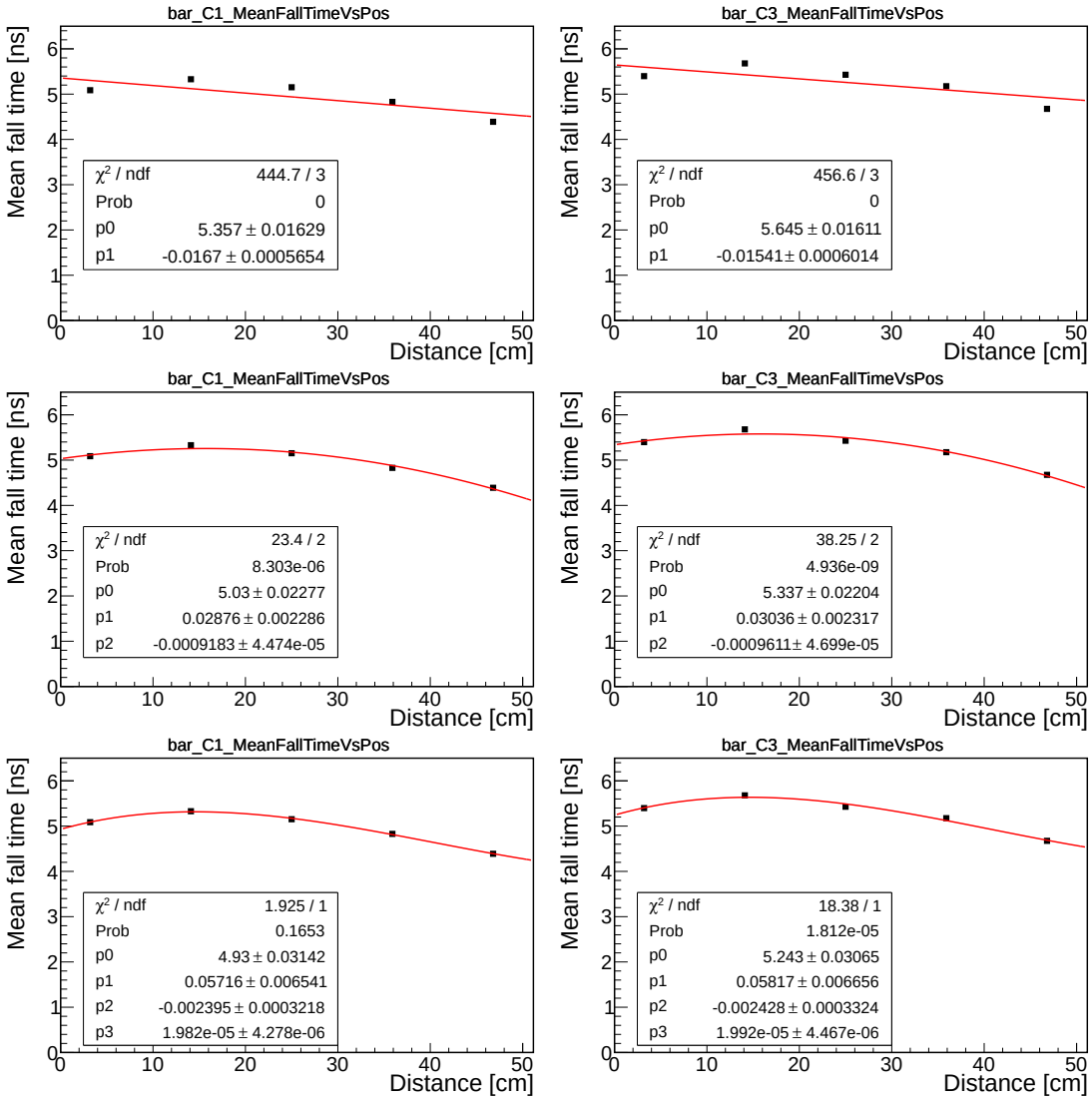

Figure C.12: Plots of mean fall time versus distance after cuts for bar shape of scintillator for photomultiplier PM1 (C1) and F2 (C3) with 3 different functions fitted to data points: linear (top pair), quadratic polynomial (central pair) and cubic polynomial (bottom pair).

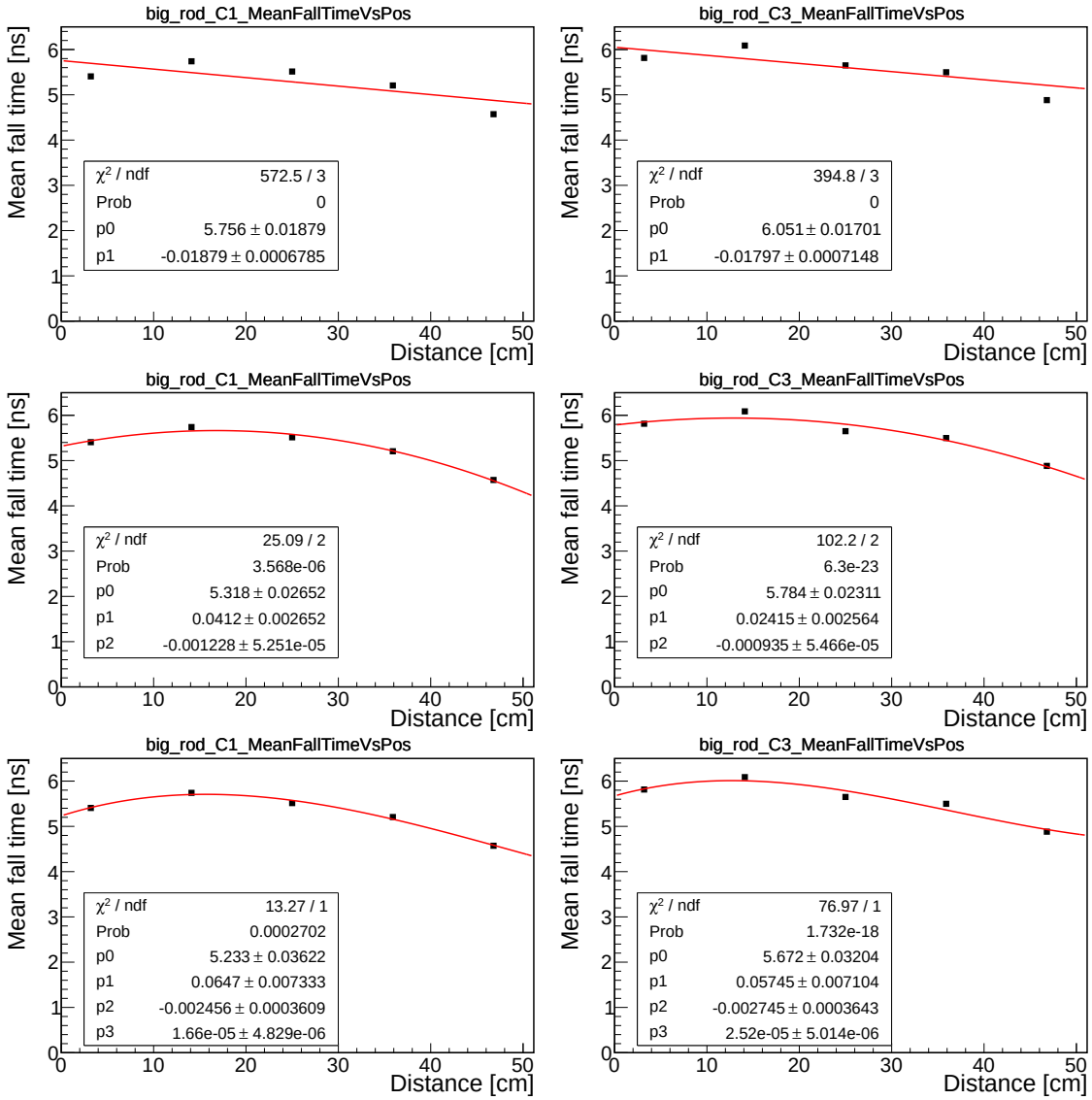

Figure C.13: Plots of mean fall time versus distance after cuts for big rod shape of scintillator for photomultiplier PM1 (C1) and F2 (C3) with 3 different functions fitted to data points: linear (top pair), quadratic polynomial (central pair) and cubic polynomial (bottom pair).

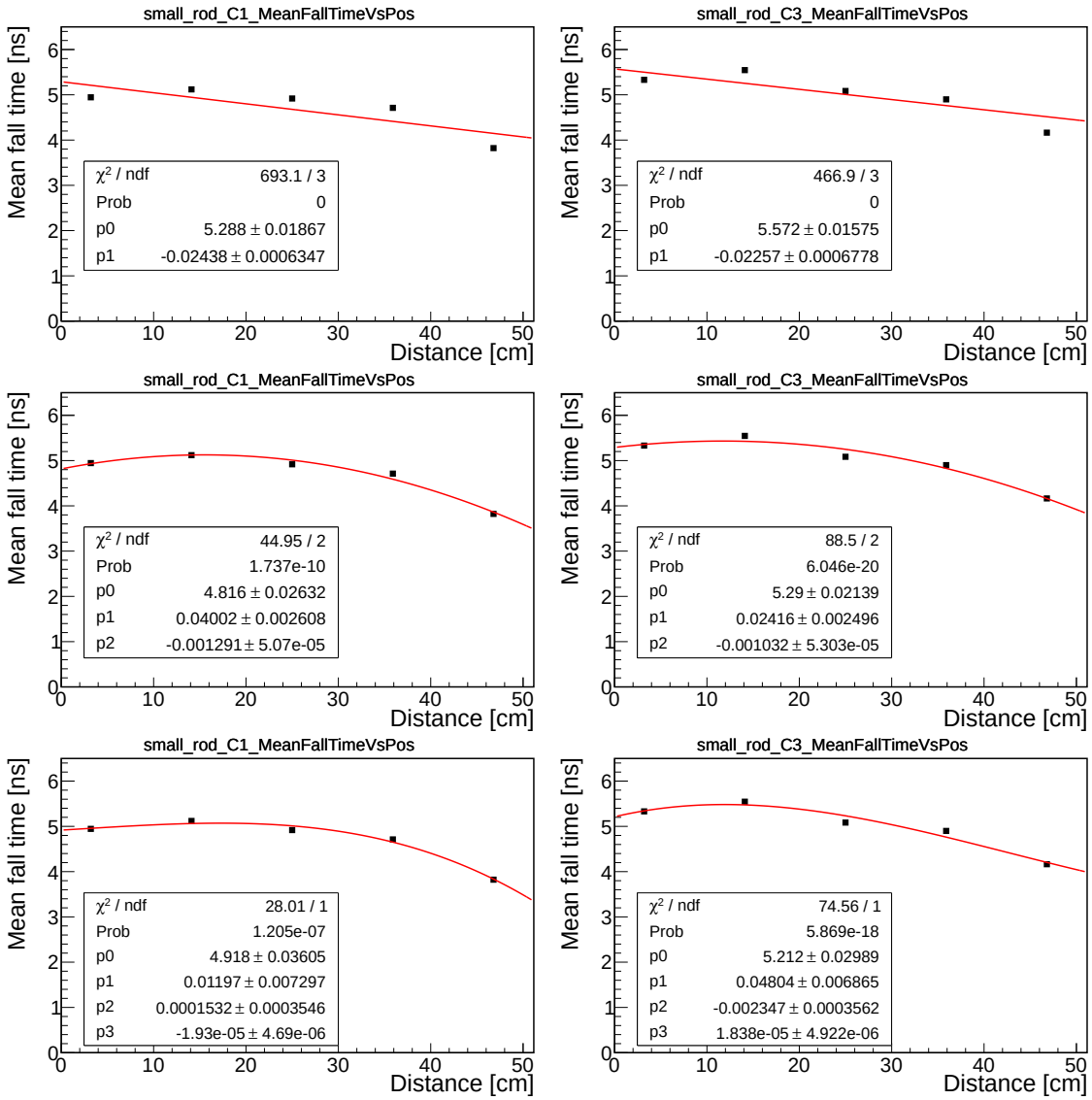

Figure C.14: Plots of mean fall time versus distance after cuts for small rod shape of scintillator for photomultiplier PM1 (C1) and F2 (C3) with 3 different functions fitted to data points: linear (top pair), quadratic polynomial (central pair) and cubic polynomial (bottom pair).

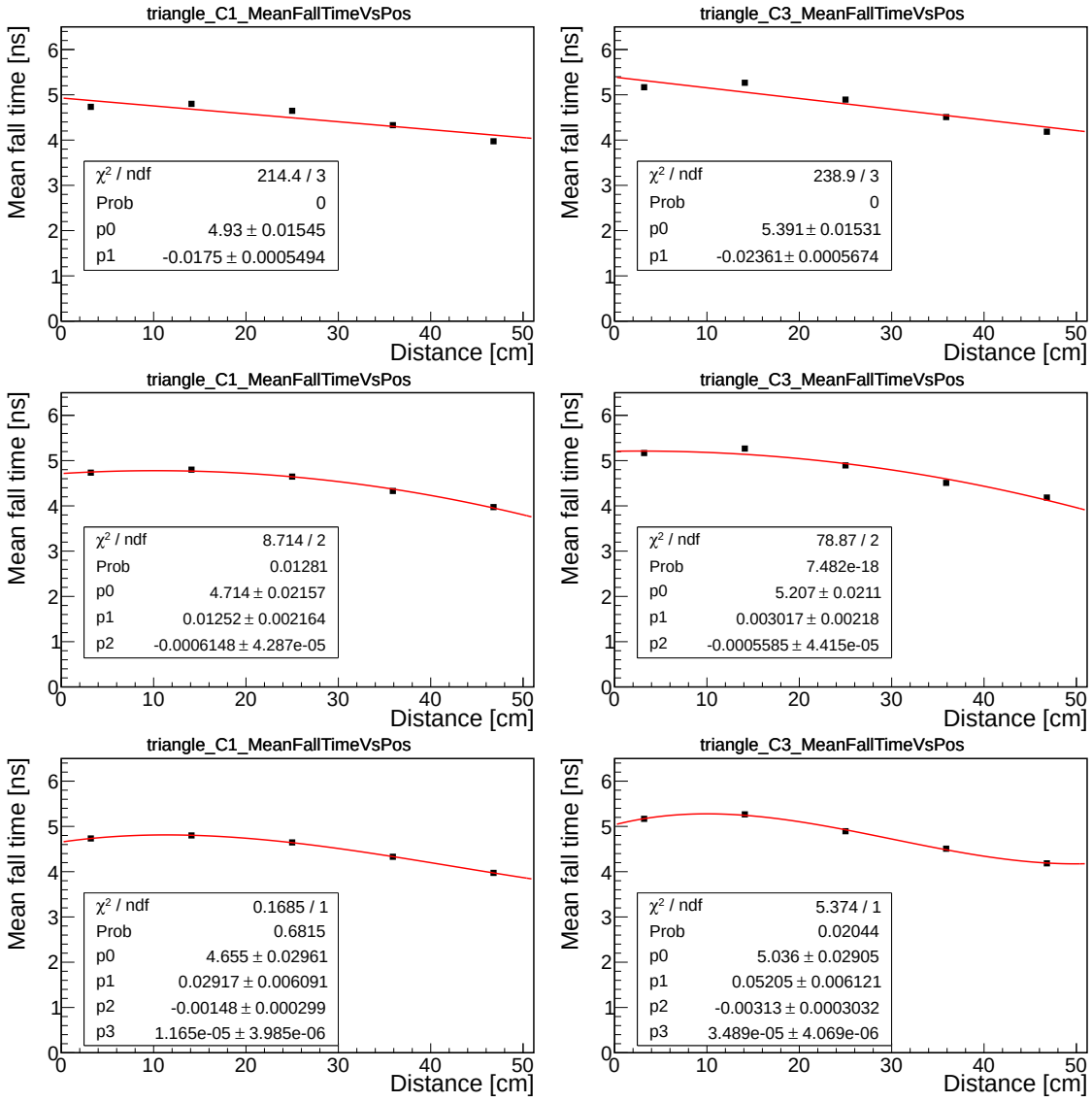

Figure C.15: Plots of mean fall time versus distance after cuts for triangle shape of scintillator for photomultiplier PM1 (C1) and F2 (C3) with 3 different functions fitted to data points: linear (top pair), quadratic polynomial (central pair) and cubic polynomial (bottom pair).

Appendix D - area spectra

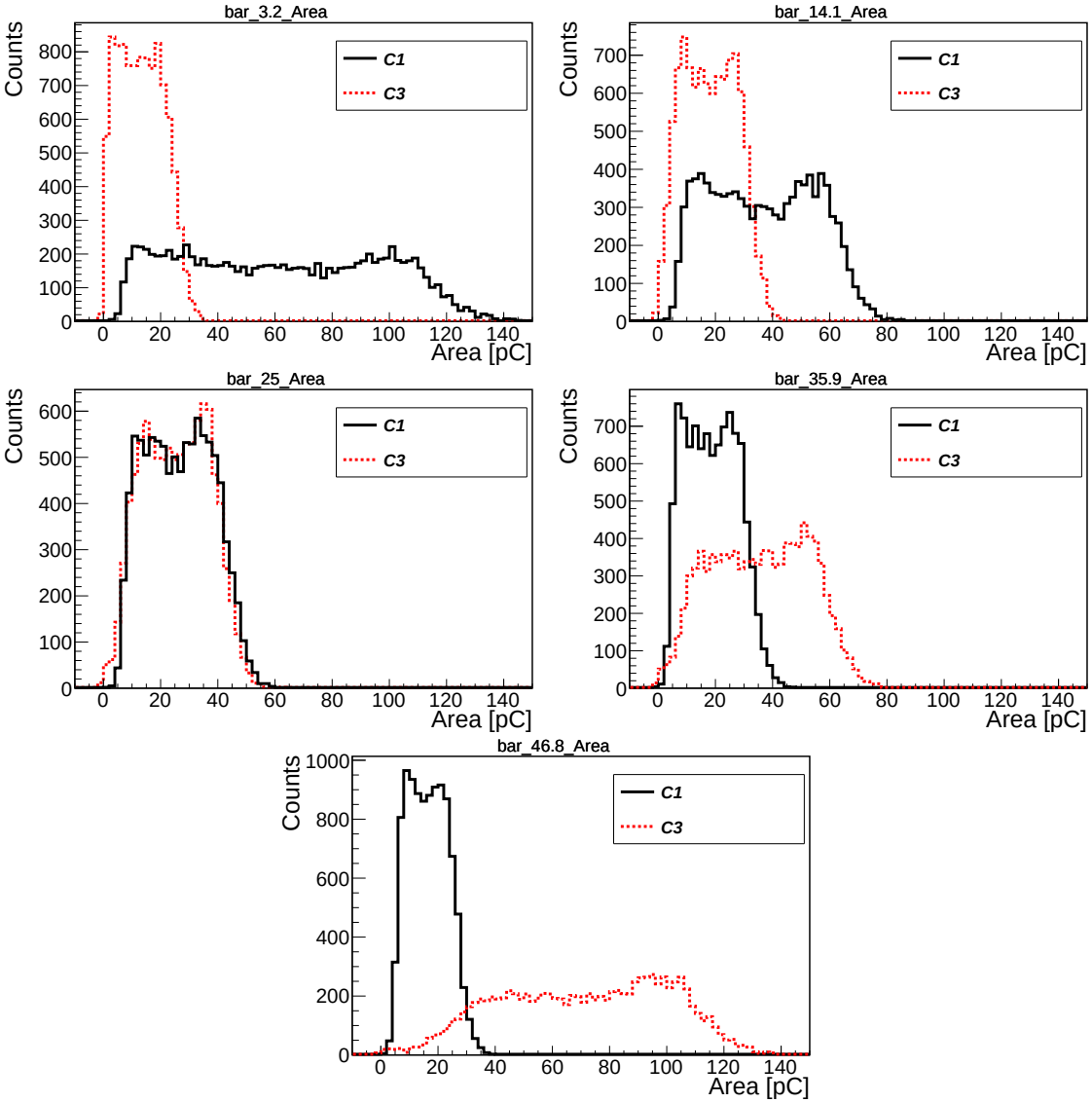

Figure D.1: Histograms of area under signals for bar shape of scintillator for all five positions.

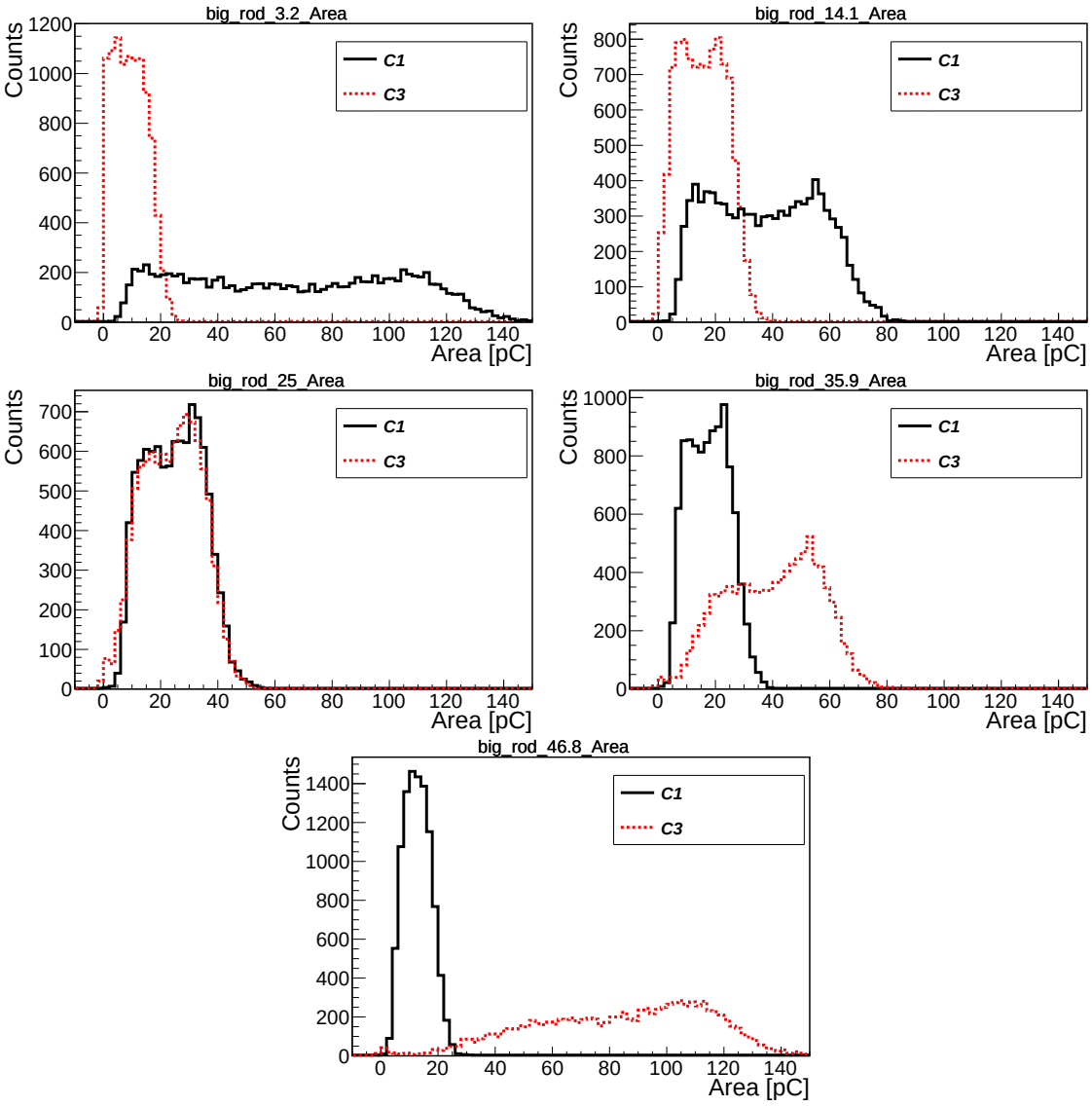

Figure D.2: Histograms of area under signals for big rod shape of scintillator for all five positions.

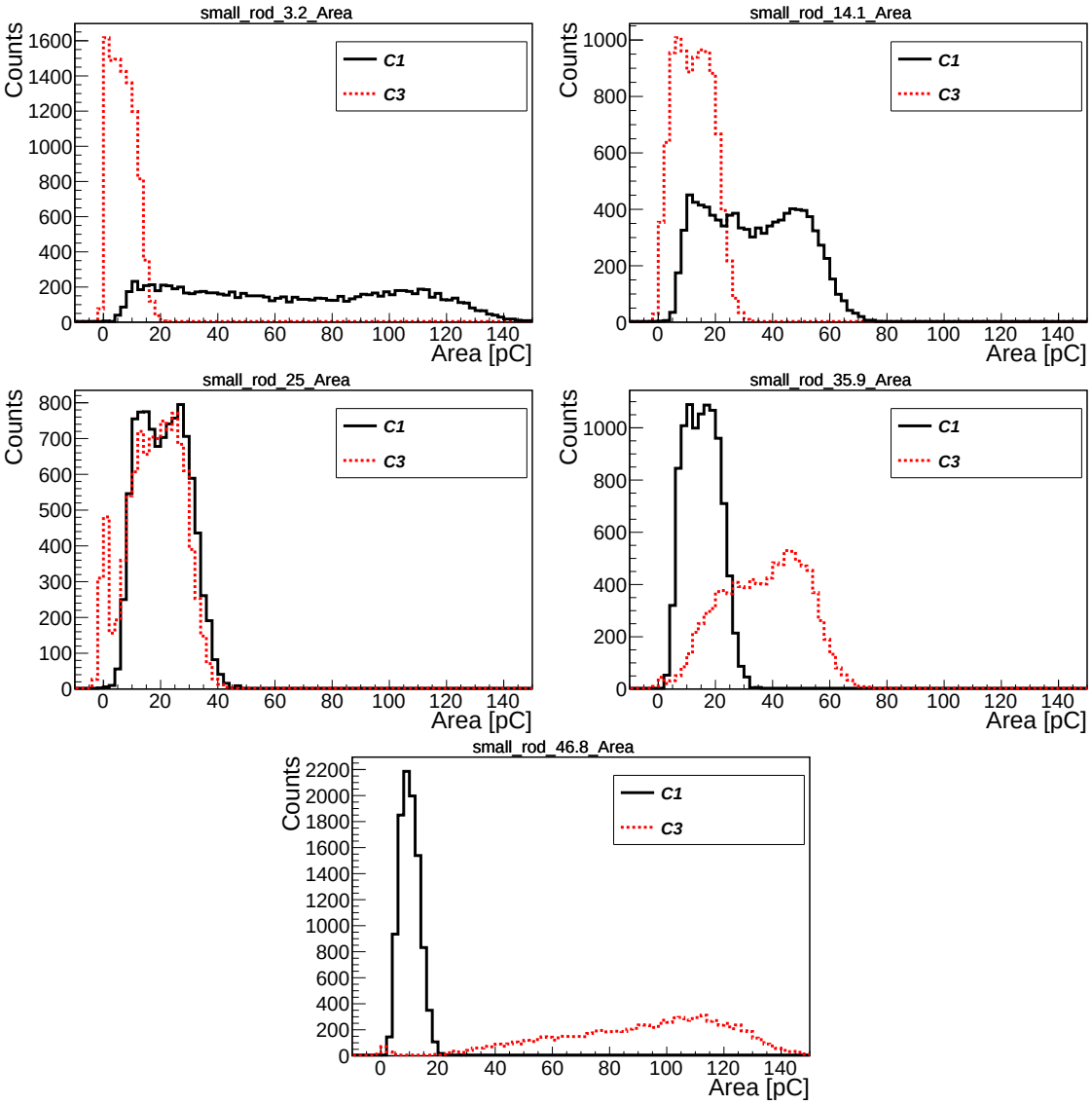

Figure D.3: Histograms of area under signals for small rod shape of scintillator for all five positions.

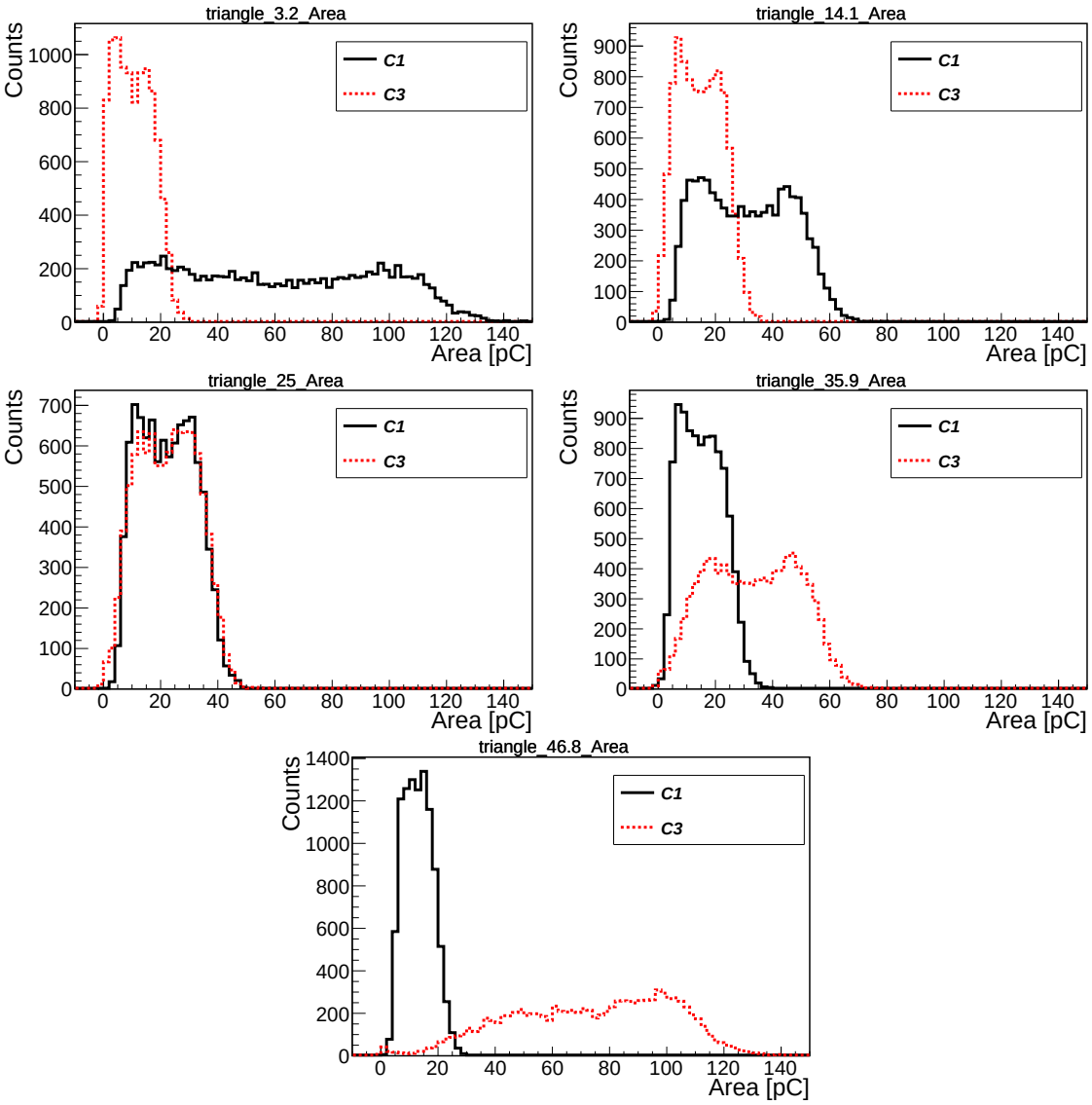

Figure D.4: Histograms of area under signals for triangle shape of scintillator for all five positions.

Appendix E - amplitude spectra

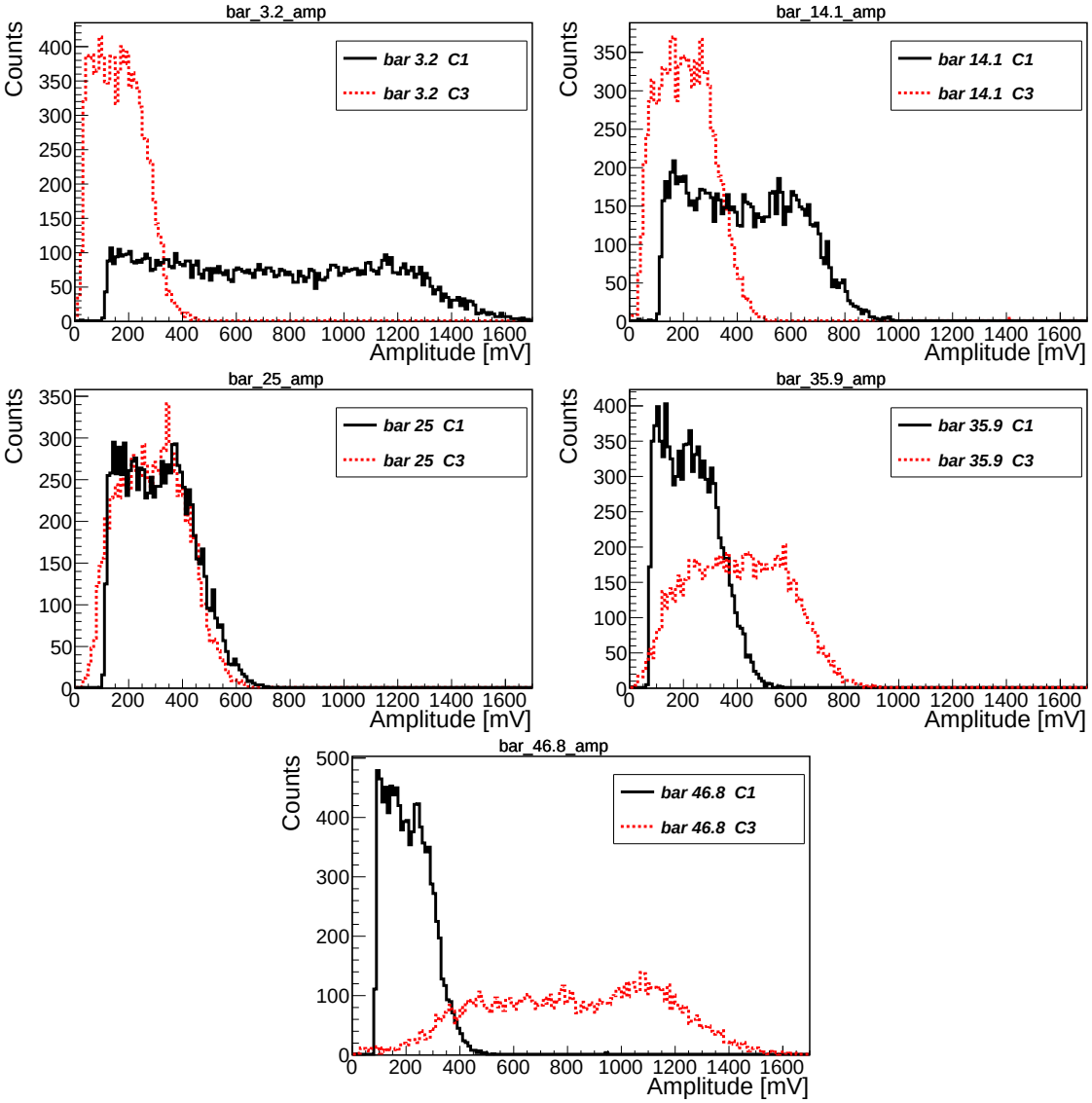

Figure E.1: Histograms of signals amplitude for bar shape of scintillator for position 3.2 cm, 14.1 cm, 25 cm, 35.9cm and 46.8 cm.

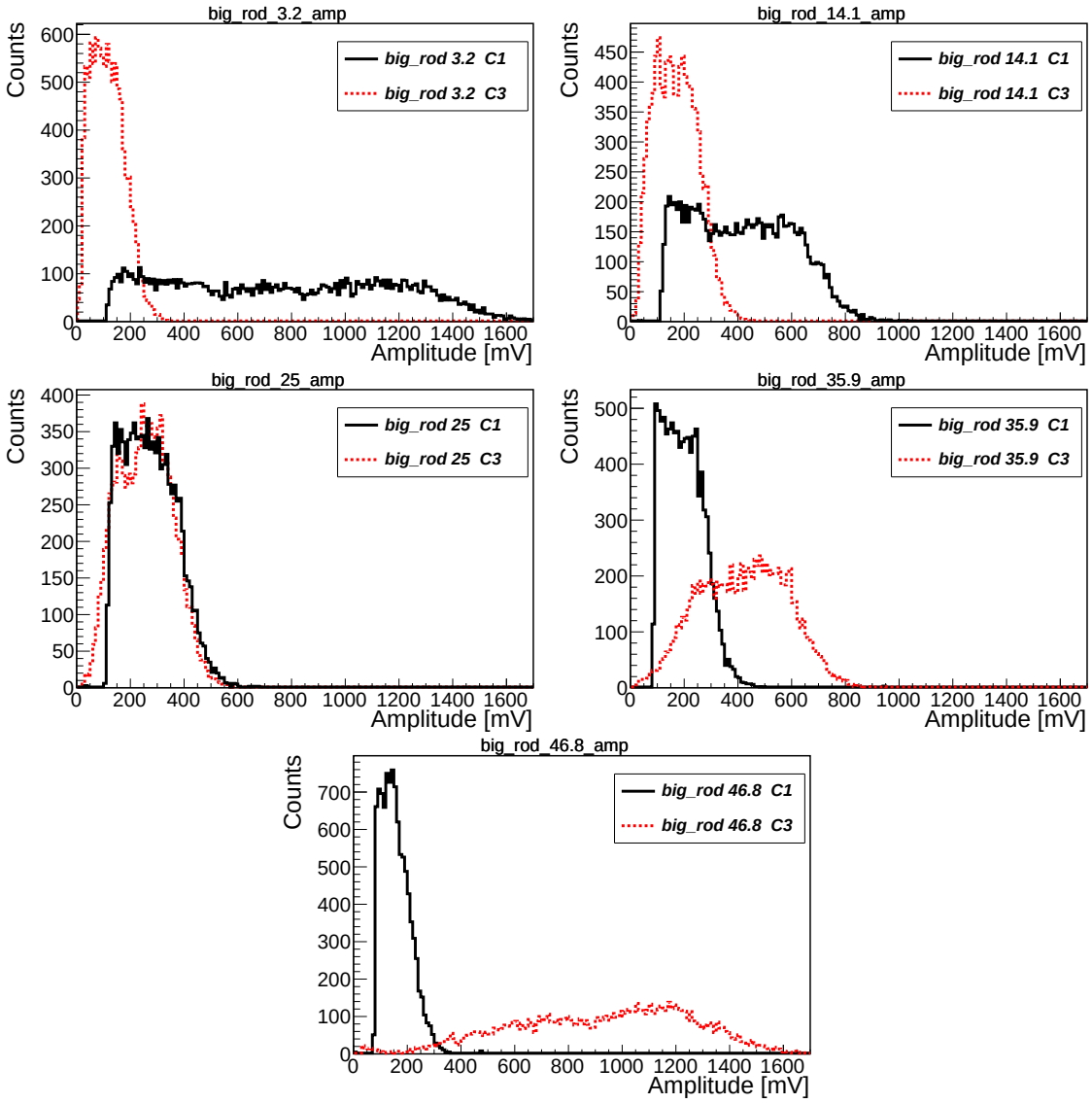

Figure E.2: Histograms of signals amplitude for big rod shape of scintillator for position 3.2 cm, 14.1 cm, 25 cm, 35.9cm and 46.8 cm.

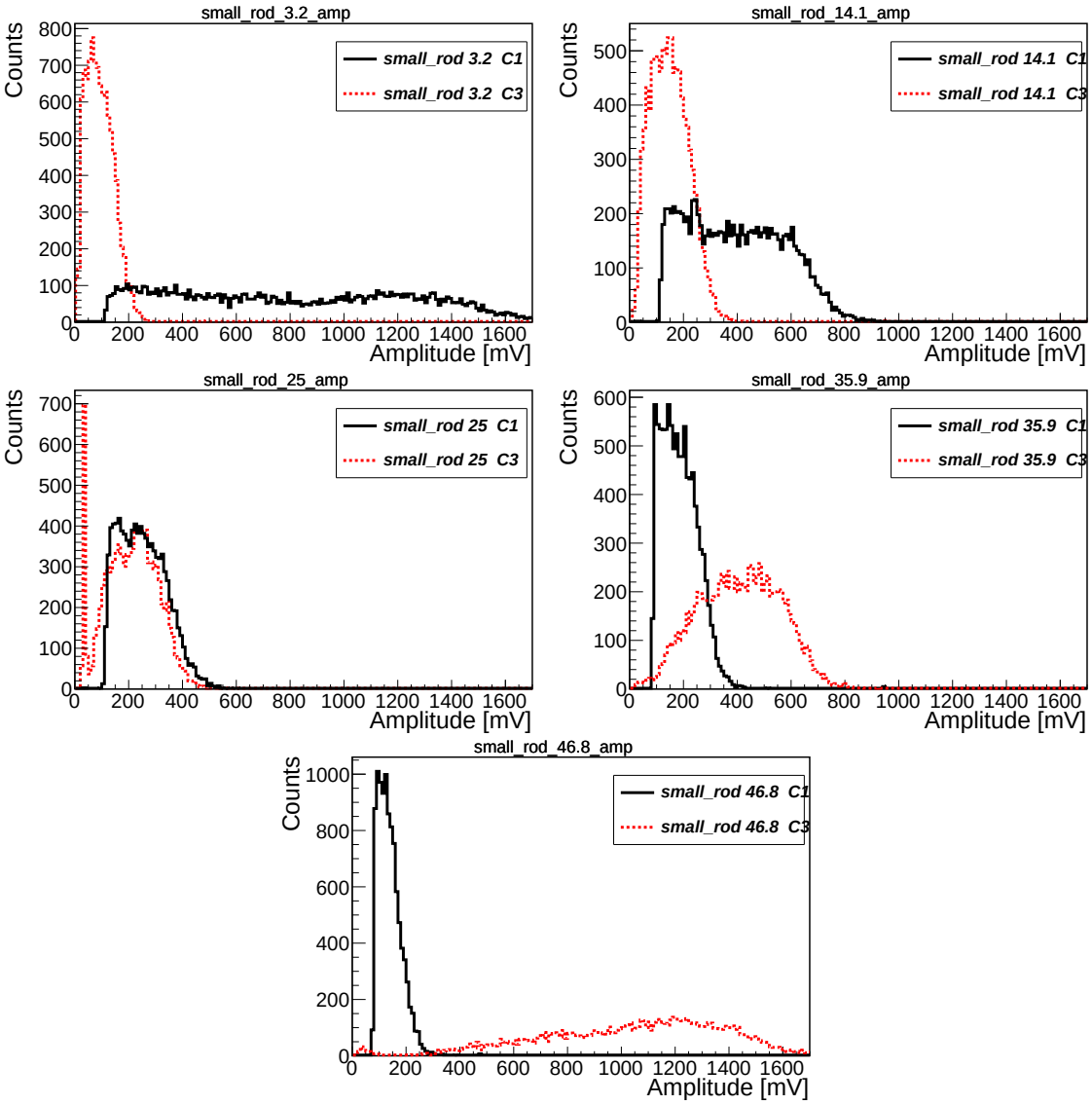

Figure E.3: Histograms of signals amplitude for small rod shape of scintillator for position 3.2 cm, 14.1 cm, 25 cm, 35.9cm and 46.8 cm.

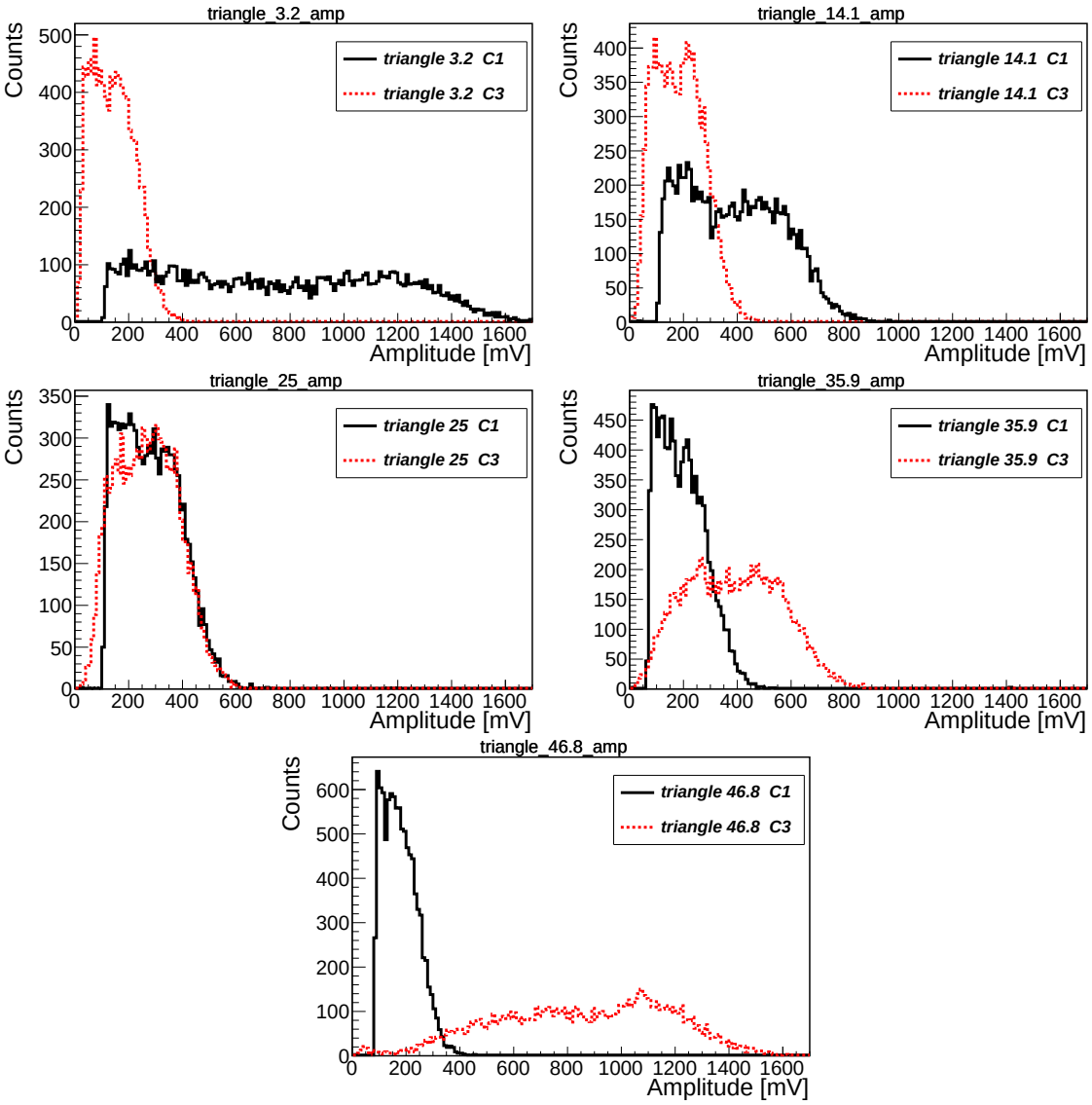

Figure E.4: Histograms of signals amplitude for triangle shape of scintillator for position 3.2 cm, 14.1 cm, 25 cm, 35.9cm and 46.8 cm.

References

[1] P. Moskal et al., *Test of a single module of the J-PET scanner based on plastic scintillators*, Nuclear Instruments and Methods A, vol. 764, pp. 317, 2014.

[2] L. Raczynski et al., *Novel method for hit-positon reconstruction using voltage signals in plastic scintillators and its application to the Positron Emission Tomography*, Nuclear Instruments and Methods A, vol. 764, pp. 186, 2014.

[3] P. Moskal et al., *A novel TOF-PET detector based on organic scintillators*, Radiotheraphy and Oncology, vol. 110, pp. S69, 2014.

[4] P. H. Elsinga, *Present and future of PET - radiopharmaceuticals*, Nuclear Medicine Review, vol. 15, pp. C13—C16, 2012.

[5] R. N. Bryan, *Introduction to the Science of Medical Imaging*, Cambridge University Press, Cambridge, 2010.

[6] M. S. Jacobson, R. A. Steichen, P. J. Peller, *PET-CT and PET-MRI in Oncology. A Practical Guide*, Springer, pp. 19-30, 2012.

[7] G. B. Saha, *Basics of PET Imaging. Physics, Chemistry, and Regulations*, Springer, 2010.

[8] M. N. Wernick, J. N. Aarsvold, *Emission Tomography. The Fundamentals of PET and SPECT*, Elsevier Academic Press, San Diego, 2004.

[9] W. Wadsak , M. Mitterhauser, *Basics and principles of radiopharmaceuticals for PET/CT*, European Journal of Radiology, vol. 73, pp. 461—469, 2010.

[10] E. Czaicka, *Liniowy model Poytonowego Tomografu Emisyjnego*, Diploma thesis, Jagiellonian University , Department of Physics, 2008.

[11] *Scintillation Detectors.Particle Detection via Luminescence*, http://www.kip.uni-heidelberg.de/∼coulon/ Lectures/Detectors/Free_PDFs/ Lecture4.pdf

[12] *How it works: Positron Emission*, http://courses.washington.edu/bioen508/Lecture5-B-PET.pdf

[13] M. Ciszewska, *Badanie rozdzielczości czasowej detektorów scyntylacyjnych pod kątem ich użycia w pozytonowej tomografii emisyjnej*, Diploma thesis, Jagiellonian University, Department of Physics, 2012.

[14] Sz. Niedźwiecki, *Studies of detection of Îş radiation with use of organic scintillator detectors in view of positron emission tomography*, Diploma thesis, Jagiellonian University, Department of Physics, 2011.

[15] A. T. Nassalski, *Wspólny detektor do tomografii pozytonowej i rentgenowskiej*, PhD thesis, The Andrzej Soltan Institute For Nuclear Studie, 2010.

[16] N. Hegemann, *Simulation studies and validation towards a TOF-PET detector*, Diploma thesis, University of Hamburg, Faculty of Experimental Physics, 2011.

[17] C. Grupen, B. Shwartz, *Particle Detectors*, Cambridge Monographs on Particle Physics, Nuclear Physics and Cosmology, Cambridge, 2008.

[18] M. E. Phelps, *PET: Physics, Instrumentation, and Scanners*, Springer, 2006.

[19] S. N. Ahmed, *Physics and Engineering of Radiation Detection*, Academic Press, Elsevier, 2007.

[20] C. Leroy, P. Rancoita, *Principles Of Radiation Interaction In Matter And Detection*, World Scientific, 2009.

[21] G. F. Knoll, *Radiation Detection*, John Wiley & Sons, 2000.

[22] *Scintillation Products Data Sheet, Saint-Gobain Ceramics & Plastics*, 2014.

[23] *P11. Strip-PET: Concept of TOF-PET scanner based on polymer scintillator strips*, Abstract, Poster session, http://www.ips.if.uj.edu.pl/files/bf4d900bed3f3a0e43b23be203f024a2/NuclMedRev15_2012_A61.pdf.

[24] *Polymer scintillator detectors for TOF-PET with large longitudinal field of view*, Abstract, Oral presentations, http://koza.if.uj.edu.pl/files/da5525964911934e69c174fbeb7cd14c/NuclMedRev15_2012_A25.pdf.

[25] *Plastic scintillators Data Sheet, Eljen Technology*, http://www.eljentechnology.com/index.php/products/ plastic-scintillators/68-ej-232, http://www.eljentechnology.com/index.php/products/plastic-scintillators/60-product-template, http://www.eljentechnology.com/index.php/products/plastic-scintillators/65-ej-228, 2014.

[26] *Hammamatsu Data Sheet*, http://www.hamamatsu.com/us/en/R5320.html, 2014.

[27] *Internal reports of J-PET collaboration.*

[28] *Internal images of J-PET collaboration.*

[29] *Sublima website*, http://dev-sublima.keepwebsimple.de/objectives/performance.html, 2014.

[30] P. Moskal et al.,*Strip-PET: a novel detector concept Âη for the TOF-PET scanner*, Nuclear Medicine Review, vol. 15, pp. C68âĂŞC69, 2012.

[31] M. Mitterhauser and W. Wadsak,*Imaging Biomarkers or Biomarker Imaging?*, Pharmaceuticals, vol. 7, pp. 765-778, 2014.